SPACE
TELESCOPE
SCIENCE
INSTITUTE

NASA CR-189365

IN-89-CR
NAS5-26555
IN-89
14038
104 P

Hubble Space Telescope

Faint Object Camera

Instrument Handbook

[Post-COSTAR]

(NASA-CR-189365) HUBBLE SPACE TELESCOPE FAINT OBJECT CAMERA INSTRUMENT HANDBOOK (POST-COSTAR), VERSION 5.0 (Space Telescope Science Inst.) 104 p

N94-36795

Unclas

G3/89 0014038

Version 5.0

May 1994

Revision History

Handbook Version 1.0	May 1985; edited by F. Paresce
Handbook Version 2.0	April 1990; edited by F. Paresce
Handbook Version 3.0	April 1992; edited by F. Paresce
Handbook Version 4.0	February 1993; edited by A. Nota, R. Jedrzejewski, W. Hack
Handbook Version 5.0	May 1994; edited by A. Nota, R. Jedrzejewski, W. Hack

The Space Telescope Science Institute is operated by the Association of Universities for Research in Astronomy, Inc., for the National Aeronautics and Space Administration.

REPORT DOCUMENTATION PAGE

Form Approved
OMB No. 0704-0188

1. AGENCY USE ONLY *(Leave blank)*

2. REPORT DATE
May 1994

3. REPORT TYPE AND DATES COVERED
Contractor Report

4. TITLE AND SUBTITLE
Hubble Space Telescope
Faint Object Camera Instrument Handbook (v. 5.0)
[Post-COSTAR]

5. FUNDING NUMBERS
633

6. AUTHOR(S)
Editors: A. Nota, R. Jedrzejewski, P. Greenfield and W. Hack

7. PERFORMING ORGANIZATION NAME(S) AND ADDRESS(ES)
Space Telescope Science Institute
3700 San Martin Drive
Baltimore, MD 21218

8. PERFORMING ORGANIZATION REPORT NUMBER

9. SPONSORING/MONITORING AGENCY NAME(S) AND ADDRESS(ES)
National Aeronautics and Space Administration
Washington, D.C. 20546–0001

10. SPONSORING/MONITORING AGENCY REPORT NUMBER
CR-189365

11. SUPPLEMENTARY NOTES
Technical Monitor: R. Dilling, Code 633

12a. DISTRIBUTION/AVAILABILITY STATEMENT
Unclassified–Unlimited
Subject Category 82
Report is available from the NASA Center for AeroSpace Information, 800 Elkridge Landing Road, Linthicum Heights, MD 21090; (301) 621-0390.

12b. DISTRIBUTION CODE

13. ABSTRACT *(Maximum 200 words)*

The Faint Object Camera (FOC) is a long-focal-ratio, photon-counting device capable of taking high-resolution two-dimensional images of the sky up to 14 by 14 arcseconds squared in size with pixel dimensions as small as 0.014 by 0.014 arcseconds squared in the 1150 to 6500 Å wavelength range. Its performance approaches that of an ideal imaging system at low light levels. The FOC is the only instrument on board the Hubble Space Telescope (HST) to fully use the spatial resolution capabilities of the Optical Telescope Assembly (OTA) and is one of the European Space Agency's contributions to the HST program.

14. SUBJECT TERMS
Hubble Space Telescope

15. NUMBER OF PAGES
96

16. PRICE CODE

17. SECURITY CLASSIFICATION OF REPORT	**18. SECURITY CLASSIFICATION OF THIS PAGE**	**19. SECURITY CLASSIFICATION OF ABSTRACT**	**20. LIMITATION OF ABSTRACT**
Unclassified	Unclassified	Unclassified	Unlimited

NSN 7540-01-280-5500

Standard Form 298 (Rev. 2-89)
Prescribed by ANSI Std. 239-18, 298-102

FAINT OBJECT CAMERA
INSTRUMENT HANDBOOK
[Post-COSTAR]

A. Nota
R. Jedrzejewski
P. Greenfield
W. Hack

Space Telescope Science Institute
3700 San Martin
Baltimore, MD 21218

Version 5.0

May 1994

CAUTION

The procedures for creating a Phase II proposal are being reviewed and revised as this is written. We strongly recommend that users check the Phase II documentation carefully. We also recommend checking on STEIS at that time for a revised version of this Instrument Handbook.

Major changes from the FOC Instrument Handbook,version (4.0)

1. **The F/48 Camera is not available in Cycle 5**, due to the high background count rate and high-voltage turn-on problems which have occurred in the past two years. The F/48 was last successfully switched on December 22, 1993, before the deployment of the COSTAR corrective optics. The camera remained on for the duration of the observation. While the acquisition image showed a background level which, although high, was consistent with the previous dark count images, a preliminary analysis of the following images showed immediately that the background increased dramatically with time, eventually reaching saturation levels approximately two hours after HV switch-on. Whether this characteristic of increasing background is a permanent condition of the F/48 is not clear. **As a consequence, the F/48 will not be made available to GOs during Cycle 5, pending further testing and analysis.** See section 6.4 for further details.
2. **The Point Spread Function** description has been updated to reflect the results from SMOV and early Cycle 4 calibrations. COSTAR has restored much of the OTA capability, in that the COSTAR-corrected PSF contains more than 75% of the light within a radius of 0.1 arcsecond at visible wavelengths while only losing less than 20% of the light to the two reflections at the two extra mirror surfaces. The net increase in sensitivity is a factor of approximately 3—4 at visible wavelengths. Section 6.1 contains all the new information.
3. **The Absolute Detector Quantum Efficiency** has been updated after execution of the related Cycle 4 Calibration program. A new OTA + COSTAR + FOC central absolute quantum efficiency curve is provided as a function of wavelength for the four FOC imaging and spectrographic configurations. The data represent the product of in-orbit measurements for the new F/96 relay+OTA absolute quantum efficiency, and ground-based reflectance calibrations of the COSTAR mirrors for the new F/48. The predicted loss of light from two reflections of MgF_2 coated aluminum COSTAR mirrors amounts to a 20% loss in the visible and a 35% loss in the ultraviolet. The loss due to the COSTAR mirrors is more than compensated by the improvement in image quality, since the encircled energy performance is improved from 18% within a 0.1" radius to $\simeq$80% within the same area, based on theoretical PSFs. For a detailed discussion, see Section 6.3. In addition, a format dependence sensitivity effect has been studied, and the results are provided in Section 6.3.1
4. **The Format-Dependent Sensitivity Effect** has been measured and has been found to be substantial (as much as a 45% change). Section 6.3.1 lists the relative sensitivities of the more common imaging formats.
5. **The Geometric Distortion** discussion has been updated (Section 6.11) and new values for the FOC plate scale are provided in Section 6.12).
6. **The prescription for Estimating Exposure Times** has been updated to take into account the new PSF and DQE parameters (see Section 7.0).

CONTENTS

LIST OF FIGURES

LIST OF TABLES

1.0 INTRODUCTION

The Faint Object Camera (FOC) is a long-focal-ratio, photon-counting device capable of taking high-resolution two-dimensional images of the sky up to 14 by 14 arcseconds squared in size with pixel dimensions as small as 0.014 by 0.014 arcseconds squared in the 1150 to 6500Å wavelength range. Its performance approaches that of an ideal imaging system at low light levels. The FOC is the only instrument on board the Hubble Space Telescope (HST) to fully use the spatial resolution capabilities of the Optical Telescope Assembly (OTA) and is one of the European Space Agency's contributions to the HST program.

The HST was placed in orbit on April 24, 1990. A few months later, it was realized that the 2.4m diameter primary mirror suffered serious optical degradation due to a manufacturing error at Perkin-Elmer. The primary mirror of the HST OTA was incorrectly figured with the wrong conic constant, which produced severe spherical aberration at the OTA image plane (Burrows *et al.* 1991, *Ap.J.Letters*, 369,L21.). This aberration, which caused the light from a star to be spread out into a circular Point Spread Function (PSF) of 2.5 arcseconds radius, could not be removed by changing the secondary mirror focus position or by moving the primary mirror actuators. In the fall of 1990, a Strategy Panel was convened to investigate possible methods for removing the spherical aberration, and made the following recommendations: 1) replace the Wide Field Planetary Camera (WF/PC) with the WFPC2 at the earliest possible opportunity, with the optics of the WFPC2 re-designed to counteract the OTA spherical aberration, and 2) replace the High-Speed Photometer with an instrument designed to deploy corrective optics in front of the remaining axial instruments (FOC, GHRS and FOS)— COSTAR. Both these recommendations were approved by NASA, and were implemented in the first Servicing Mission executed in December 1993.

COSTAR (Corrective Optics Space Telescope Axial Replacement) has restored the two prime scientific objectives of the FOC: deep imagery and photometry of very faint celestial objects and imagery of bright objects at the highest possible resolution available from HST. The FOC is now capable of detecting a star of U magnitude 27.5 in a 5 hour exposure with a S/N = 5 and of resolving bright sources in the near UV up to an effective angular resolution of $\simeq$0.04 arcseconds.

Other main scientific objectives of the FOC include, but are not restricted to, the study of the physics of planets, search for planets and proto-planetary condensations around nearby stars, search for massive black holes in globular clusters, study of the ionization structure of shock waves in the interstellar medium, high spatial resolution studies of very young stars and cataclysmic variables and their interaction with the surrounding interstellar medium, the study of stellar content of globular clusters, observation of optical emission associated with radio lobes and jets in galaxies, the observations of velocity dispersion and mass densities in the central regions of normal and compact elliptical galaxies, observation of extended structure around QSOs at high spatial resolution, and the study of gravitational lenses.

The basic aim of this handbook is to make relevant information about the performance of the FOC+COSTAR system available to a wide group of astronomers, primarily to aid in applying for HST time, and to aid those who have had FOC proposals accepted in planning and specifying their exposures. **At this point it needs to be emphasized that, due to the high background count rate and high-voltage turn-on problems which have occurred in the F/48 relay (see Section 6.4), the F/48 camera will not be made available in Cycle 5, pending further testing and data analysis.**

The information contained in this handbook has been obtained from the combination of the inflight characterization of the FOC, COSTAR ground and flight calibrations and represents our best present knowledge of the performance of the FOC+COSTAR system. **For Cycle 5, this handbook supersedes all the previous versions. However, if the reader is interested in preparing an Archival Proposal for observations taken during the previous cycles (before COSTAR was deployed), the Cycle 3 Handbook (Version 3) must be used as a reference instead.**

A brief overview of COSTAR and its effect on the OTA image quality is presented in Section 2. The FOC, as presently configured, is briefly described and some basic performance parameters summarized in Section 3. A more detailed, in-depth perspective on the FOC can be found in Section 4. In Sections 6 and 7, the readers will find the detailed FOC performance parameters and instructions on how to derive approximate FOC exposure times for the proposed targets and some useful examples. The last section deals with the expected data products and calibration plans. This plan should allow readers to choose the level of detail required to match their previous degree of understanding of the instrument with the degree of complexity of the proposed observing program.

2.0 COSTAR OVERVIEW

COSTAR replaces the High Speed Photometer in the Axial bay of HST, in the −V2, +V3 quadrant (see Figure 7). It is a "passive" instrument, in that it has no detector of its own, its sole purpose being to deploy a set of mirrors in front of the other Axial Scientific Instruments (ASI). These mirrors, and their associated mounts and arms, serve only to block the aberrated OTA beam from entering the ASI entrance apertures and to correct the spherical aberration of a different part of the OTA field of view before re-directing the corrected beam into the ASIs. A schematic diagram of the COSTAR optics in front of the F/96 relay is shown in Figure 1. There is a separate set of mirrors that corrects the F/48 channel, mounted on the same arms as those for the F/96 channel.

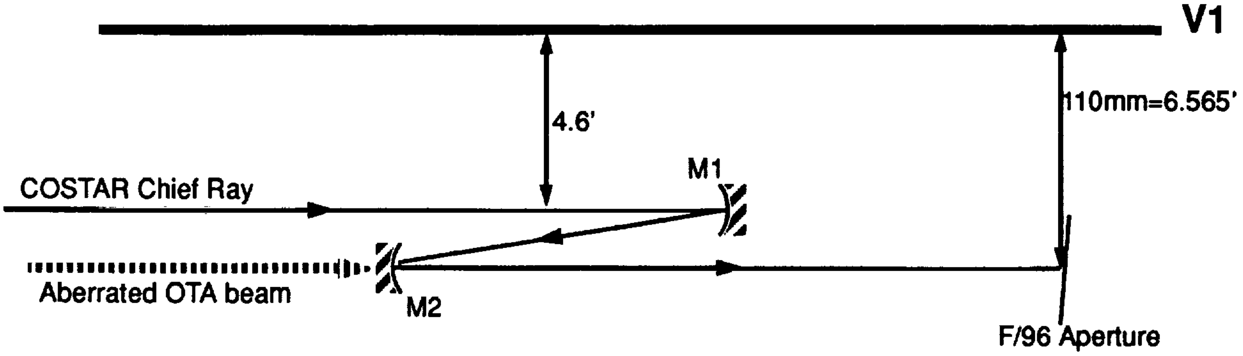

Figure 1. Diagram showing the COSTAR correction principle for the F/96 relay. The aberrated OTA beam (**dashed line**) is blocked from reaching the FOC aperture by the M2 mirror.

Before COSTAR, the aberrated F/24 OTA beam at 6.565 arcminutes from the V1 axis formed an image at the FOC focal plane aperture 110mm from the V1 axis. After the deployment of COSTAR, the M2 mirror and its mounting arm blocks this light from entering the aperture. The beam that would have formed an image 4.658 arcminutes from the V1 axis is re-directed by the spherical M1 mirror to form an image of the OTA exit pupil on the M2 mirror. This mirror becomes the exit pupil of the OTA+COSTAR optical system, and the anamorphic aspheroidal figure fulfills three functions:

- it re-directs the corrected beam into the FOC, forming an image at the FOC focal plane aperture;
- it corrects for the OTA spherical aberration;
- it increases the astigmatism from that present at 4.658 arcminutes to that appropriate to 6.565 arcminutes because the FOC is designed to correct for exactly the latter amount of astigmatism.

However, there is one major difference between the COSTAR-corrected beam and the unaberrated OTA: the F/ratio is increased from F/24 to F/37. **This results in a change in the F/number of the FOC relays from F/48 to F/75.5 and from F/96 to F/151. Because the names "F/48" and "F/96" are deeply-rooted in the HST ground system at all levels, from proposal entry to data archiving, we are forced to retain these names despite the fact that they do not describe the true focal ratios of the cameras anymore. As a result, the user must take particular care in reading this handbook, for whenever we mention the new F/48 and the new F/96 relays, we are really referring to the relays with new focal ratios of F/75.5 and F/151 respectively.**

A schematic diagram of COSTAR when deployed is shown in Figure 2. The FOC M1 mirrors are mounted on an arm which can be tilted in each of 2 orthogonal directions. This adjustment is necessary to accurately center the image of the OTA exit pupil on the M2 mirror, and was done on orbit. Any error in this centering results in the introduction of coma into the PSF. Since the M1 mirrors for both of the new relays are on the same mount ("ganged"), only one channel (the new F/96) can be optimized in this way. It is anticipated that the tilt of the new F/48 M1 mirror relative to that of the new F/96 mirror was set during ground alignment to sufficient accuracy that no appreciable residual coma is left in the new F/48 PSF. Optimization of the M1 tilt was accomplished during the Servicing Mission Observatory Verification (SMOV) period shortly after the installation of COSTAR.

The M2 mirrors for both of the new channels are also on a single arm mounting, but there is no tip/tilt capability. Both arms are connected to the Deployable Optical Bench (DOB), which can be commanded to move over a 16mm range parallel to the V1 direction. This was used to focus the new F/96 channel during SMOV. Again, it is anticipated that the focus position of the new F/48 channel relative to that of the new F/96 channel was set to an accuracy of 0.1mm or less during ground alignment.

The correction of the spherical aberration of the OTA by COSTAR does introduce a small number of side-effects that were not present in the original design of HST+FOC. Firstly, the focal plane tilt of the OTA at the FOC entrance apertures cannot be duplicated by the 2-mirror COSTAR system. The tangential and sagittal image planes produced by COSTAR are tilted with respect to those in the OTA, and tilted appreciably with respect to each other. This means that perfect astigmatism correction can only be achieved at one field point. Similarly, the mean focal surface produced by COSTAR is tilted with respect to the mean focal surface produced by the OTA, so that there is a field-dependent focus variation. These effects are described more fully in Section 6.1.

Secondly, the HST+COSTAR exit pupil is now only 530mm from the FOC entrance apertures (compared to 7m for the uncorrected OTA). This causes unavoidable vignetting in the new F/48 camera for field positions more than about 12 arcseconds away from the optimally-corrected field point. The effects of this vignetting are discussed in sections 4.2 and 6.9. The new F/96 channel does not suffer from vignetting.

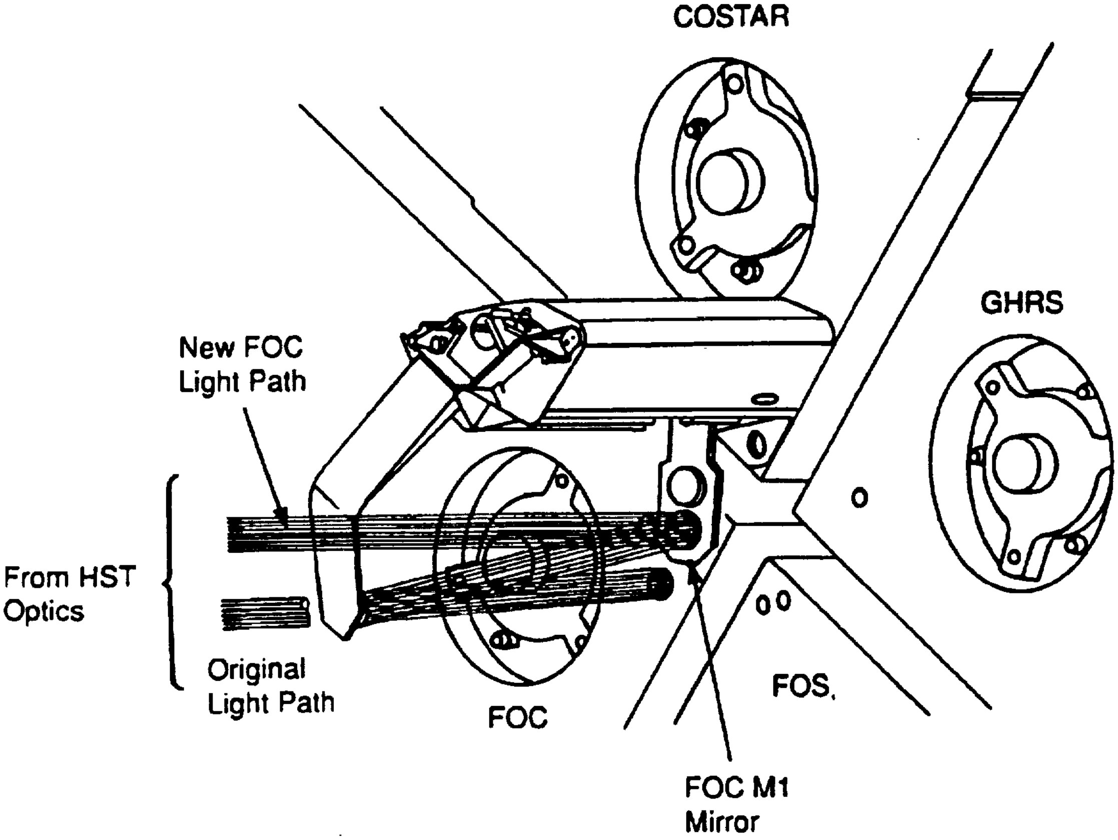

Figure 2. A Schematic View of COSTAR, after deployment, showing the FOC light paths. For clarity, the FOS and GHRS M2 arms are omitted.

For this reason, it was decided to make the new F/96 channel the 'preferred' channel of the FOC, and attempt to optimize the image quality of this channel.

3.0 INSTRUMENT OVERVIEW

The Faint Object Camera (FOC) is one of the four axial scientific instruments sharing the HST focal plane. It is located in the −V2, −V3 quadrant (see Figure 7), has overall dimensions of 0.9 ×0.9 × 2.2 meters, weighs 320 kg and consumes 130W of power on average in operation. An overall operational and data flow block diagram of the instrument is shown in Figure 3 with the FOC itself contained within the dashed line. Radiation from an astronomical source focused onto the OTA focal plane is reimaged by COSTAR and fed into either of two separate and independent cameras each with its own entrance aperture, imaging optics and detector system.

One camera magnifies the image on the OTA focal plane by a factor of two to an effective focal ratio of F/75.5 while the other magnifies the focal plane by a factor of four to an effective focal ratio of F/151. This transfer is accomplished mainly in order to match the OTA resolution performance with the available detector pixel size.

Each optical relay consists of segments of a full optical figure of revolution the axis of which is perpendicular to the OTA focal plane at the FOC entrance aperture location. Both cameras have the same overall length and operate at the same distance from the OTA optical axis. The re-imaging optics transfers the COSTAR corrected OTA image onto the photocathode of a photon counting detector with negligible spherical aberration or coma and corrects for the residual OTA off-axis astigmatism. The FOC optical system also provides means for dispersing, filtering, attenuating, polarizing and focusing the image formed by the OTA and for in-flight calibration of the relative and absolute response in the visible.

All the optical elements and both detectors are supported on an optical bench which is rigidly connected to the focal-plane structure of the OTA and is contained within the load-carrying structure which also provides a light-tight enclosure. To meet the image stability requirements, the internal surfaces of the load-carrying structure which enclose the optical bench are actively thermally controlled during all operational modes with a stability of better than 0.5° C. An exploded schematic view of the FOC is presented in Figure 4.

The two detectors are two dimensional photon counting devices of identical design. Each consists of a three-stage image intensifier which is optically coupled by a relay lens system to an Electron Bombarded Silicon Target (EBS) TV tube. The tube detects scintillations at the output of the intensifier corresponding to the arrival of individual photons at the first stage photocathode. The central x-y position of each burst of visible light is measured by a dedicated video processing unit (VPU), and the contents of a memory location in the scientific data store (SDS) unit associated with that position are incremented by one. At the end of the exposure, the accumulated image in the SDS is sent directly out of the FOC to a dedicated unit in the ST Scientific Instrument Control and Data Handling (SI C&DH) subsystem which consists of a computer with a reprogrammable non-volatile memory. The two detectors in orbit produce a dark noise typically of $\simeq 7 \times 10^{-4}$ counts sec^{-1} pixel^{-1} for the new F/96 relay and $\simeq 2 \times 10^{-3}$ counts sec^{-1} pixel^{-1} for the new F/48 relay (see also Section 6.4).

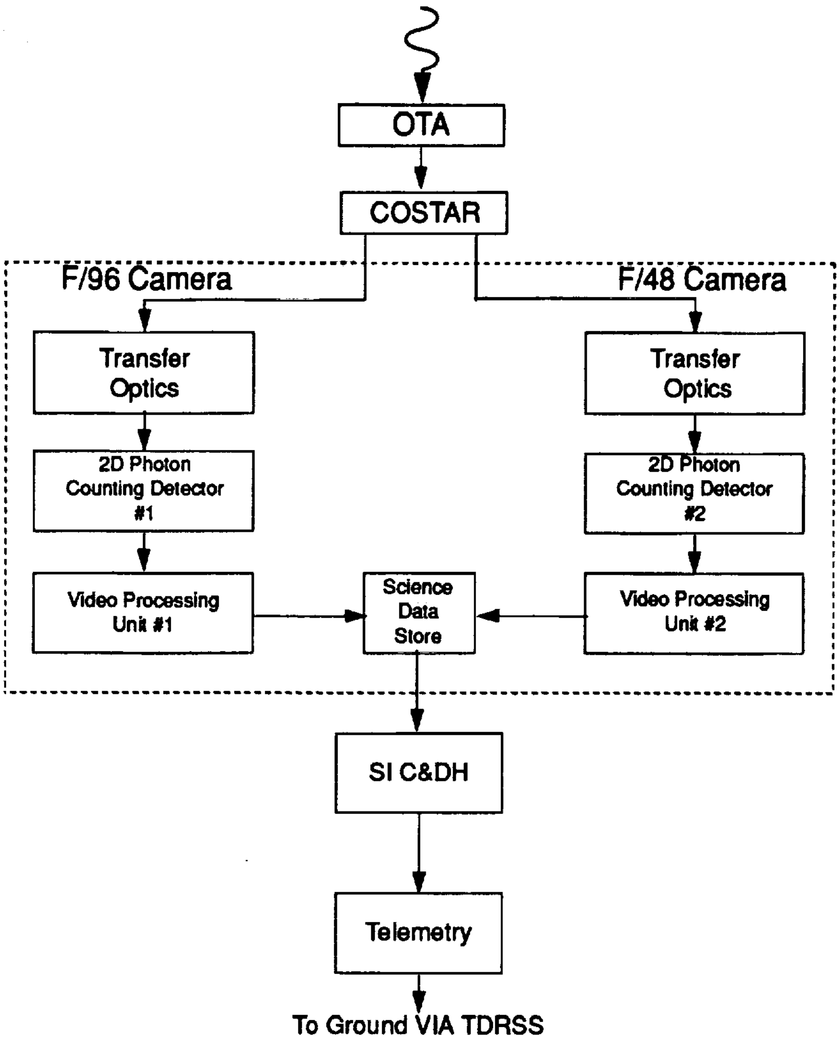

Figure 3. FOC Operational and Data Flow Block Diagram

The SDS storage capacity is adapted to an image area of 512 × 512 resolution elements and provides a 16 bit data word for each pixel. This results in a memory capacity of 256K words of 16 bits each or 0.5 Mbyte in total. The word length can also be commanded to 8 bits to store data in a 512 × 1024 pixel format with reduced dynamic range. Because of operational constraints, a time interval of at least 3.9 minutes must elapse between the end of an exposure and the start of the next.

The detectors are sensitive to radiation between 1150 and 6500Å, the lower limit being set by the MgF_2 input window and the upper limit by the bialkali photocathode material. The useful photocathode area is 40 millimeters in diameter while the size of an independent resolution element (pixel) is on average normally $\simeq$ 24 × 24 microns squared, but one dimension can be stretched (zoomed) to $\simeq$ 48 microns. The longer pixel dimension is in the

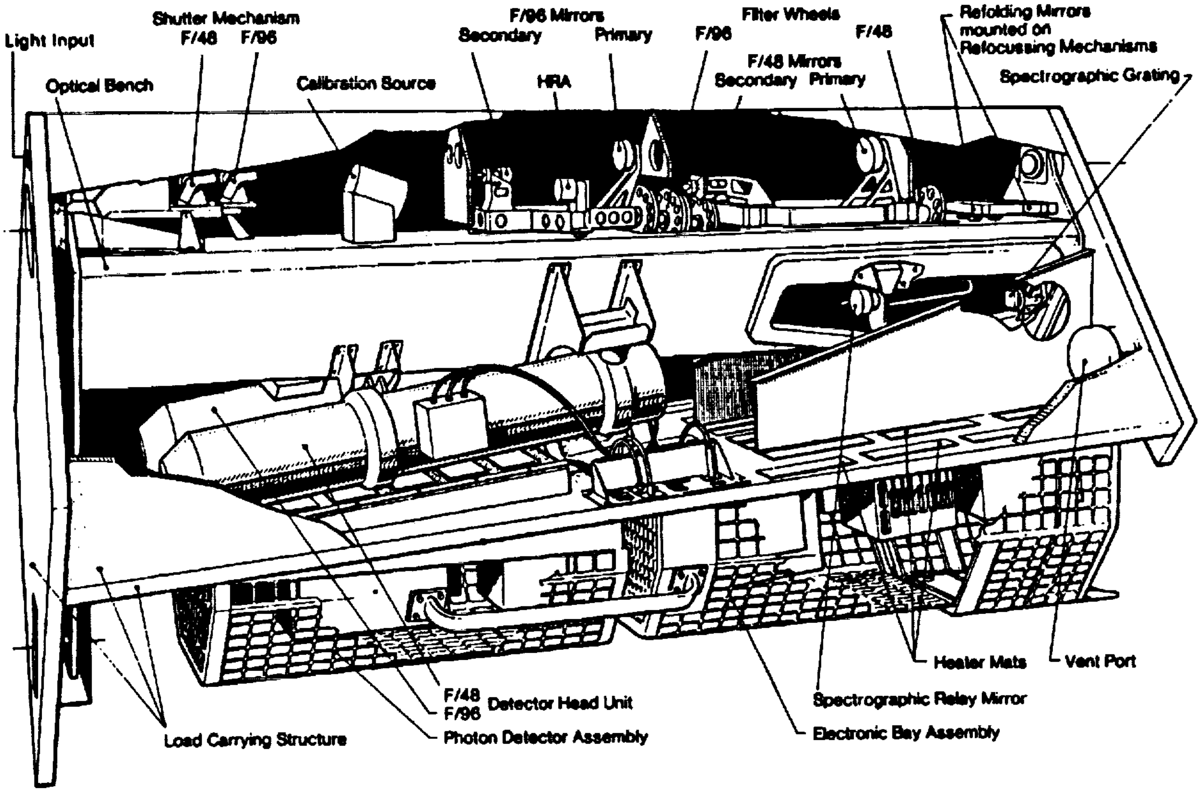

Figure 4. Schematic Drawing of the FOC

TV frame scan direction and perpendicular to the dispersion direction of all but one (the FOPCD) of the dispersing elements. The plate scales for the new F/48 and the new F/96 relays are 1.131 and 0.569 arcseconds mm^{-1} respectively.

These parameters, coupled to the quoted maximum SDS capacity, imply that the new F/48 camera has a maximum achievable field of view of $\simeq 28 \times 28$ arcseconds squared imaged at a pixel size of 0.056×0.028 arcseconds squared (512 zoomed × 1024, 48 × 24 micron squared pixels with 8- bit words). The corresponding values for the new F/96 relay are $\simeq 14 \times 14$ and 0.028×0.014 arcseconds squared. Smaller fields can be imaged at higher spatial resolution and extended dynamic range (see Table 6 for a partial list, and Section 5.1 for more details).

In summary, the key operating features of the FOC are its low noise, high angular resolution, high sensitivity in the UV range and extreme versatility due to its occultation, polarization, and objective prism capabilities. Its most significant limitations, on the other hand, are its relatively small field of view, further restricted by COSTAR, and the non-linearity of response at high count rates which limits its useful application to objects yielding less than $\simeq 2$ counts sec^{-1} pixel^{-1}, corresponding to a $U \simeq 18.5$ A0V star observed through the F342W filter with the new F/96 relay, for example. A summary of the most important performance characteristics of the FOC as presently known is given in Tables 1 and 2 for the imaging and spectrographic modes, respectively.

Table 1: Summary of FOC Performance Characteristics I. Imaging

Optical Modes	F/48[a]	F/96
Focal Ratio	75.5	151
Operating Range (Å):	1150-6500	1150-6500
Number of Bandpass Filters:	11	39
Bandpass FWHM (Å) Max:	2700	2600
Bandpass FWHM (Å) Min:	300	34
Maximum ND attenuation (mag.):	0	9
Field of View (arcsec) Max:	28x28	14x14
Field of View (arcsec) Min (128x128):	3.6x3.6	1.8x1.8
Unzoomed Pixel Size (arcsec):	0.028	0.014
Minimum Wavelength for Critical Sampling (Å):	6500	3250
Peak Efficiency (%):	6.6	7.9
Peak Wavelength (Å):	3400	3700
Limiting Magnitude, Point Source[b]:	27	27.5
Limiting Magnitude Arcsec^{-2}, Extended Source[c]:	23.5	23
Dynamic Range, Point Source[d] (mag):	18.5-27	17.5-27.5
Dynamic Range, Extended Source[e] (mag arcsec^{-2}):	18-25	17-25
Overload Magnitude:	9	9
Number of Polarizing Prisms[f]:	0	3

[a] **The F/48 mode is not available for Cycle 5.**
[b] S/N = 5, 5 hour integration, U band.
[c] Same as b. over 0.1" × 0.1" area.
[d] 2 counts sec^{-1} pixel^{-1} upper limit
[e] 0.5 counts sec^{-1} pixel^{-1} upper limit
[f] 0°,60°, 120° direction of polarization

Table 2: Summary of FOC Performance Characteristics II. Spectroscopy

Spectral Modes[a]:	F/48-FUVOP	F/48-NUVOP	F/96-FUVOP	F/96-NUVOP	F/48-SP	F/48 SP-CD	F/48 SP-SS
Operating Range[b]:	1250-3000	1700-4000	1150-3000	1700-4000	3600-5400 (1) 1800-2700 (2) 1200-1800 (3) 1150-1350 (4)	3600-5400 (1) 1800-2700 (2) 1200-1800 (3) 1150-1350 (4)	3300-5100 (1) 1650-2550 (2) 1150-1700 (3) 1150-1350 (4)
Maximum Field of View (arcsec):	28×28	28×28	14×14	14×14	0.06×12.5	0.06×12.5	
Number of Bandpass or Order Sorting Filters Available:	7	7	33	33	11	5	11
Number of ND Filters Available:	0	0	1	1	0	0	0
Spatial Resolution (arcsec):	0.1	0.1	0.05	0.05	0.063×0.1	0.063×0.1	0.1
Resolving Power:	150	80	300	250	1150	1150	1150
Wavelength (Å):	1500	2500	1500	2500	(1) - (4)	(1) - (4)	(1) - (4)
Spectrum Length (pix):	55	90	160	450	1024	1024	850
Spectrum width (pix):	2	223	3	3	≤450	≤450	≤450
Maximum Spectral Resolution (Å):	15	30	5	10	4 2 1.3 1.0	4 2 1.3 1.0	4 (1) 2 (2) 1.3 (3) 1.0 (4)
Peak Efficiency (%):	6.2	5.7	8.9	8.8	1.2 (1) 0.64 (2) 0.18 (3) 0.15 (4)	1.2 (1) 0.62 (2) 0.16 (3) 0.10 (4)	1.2 (1) 0.64 (2) 0.18 (3) 0.15 (4)
Limiting Flux, Point Source[c] (ergs $cm^{-2} s^{-1}$):	3×10^{-16}	7.5×10^{-17}	6×10^{-16}	1×10^{-16}	2×10^{-16}(1) 5×10^{-16}(2) 4×10^{-15}(3) 8×10^{-15}(4)	2×10^{-16} (1) 5×10^{-16} (2) 5×10^{-15} (3) 2×10^{-14} (4)	2×10^{-16} (1) 5×10^{-16} (2) 4×10^{-15} (3) 4×10^{-15} (4)
Limiting Flux, Extended Source[d] (ergs $cm^{-2} s^{-1} arcsec^{-2}$):	10^{-14}	2×10^{-15}	2×10^{-14}	4×10^{-15}	2×10^{-14} (1) 5×10^{-14} (2) 4×10^{-13} (3) 8×10^{-13} (4)	2×10^{-14} (1) 5×10^{-14} (2) 5×10^{-13} (3) 2×10^{-12} (4)	2×10^{-14} (1) 5×10^{-14} (2) 4×10^{-13} (3) 8×10^{-13} (4)

a. SP = Spectrograph; SP-CD = Cross Dispersion Spectrograph; SP-SS = Slitless Spectrograph; **F/48 Modes are Not Available for Cycle 5.**

b. Spectrograph characteristics are given at the following wavelengths for each order: (1) 5000Å, (2) 2500Å, (3) 1500Å, (4) 1250Å

c. S/N = 5, 3 hour integration, flux in emission line at 1500Å(FUVOP) and 2500Å(NUVOP).

d. Same as c. over 0."063 × 0."063 area.

4.0 DETAILED INSTRUMENT DESCRIPTION

4.1 TRANSFER OPTICS

A component block diagram of the FOC transfer optics is shown in Figure 5. A conceptual schematic optical layout in a plane containing the V1 axis and the chief ray is shown in Figure 6. Radiation from the COSTAR corrected OTA enters the FOC through a baffled tube that leads to a field-defining entrance aperture located in a plane tangential to the OTA focal surface and centered on or near the best focus point at the position of each relay. Just beyond the entrance aperture, the radiation encounters a light tight shutter mechanism that, in its closed position, introduces a calibration mirror into the beam to intercept light emitted by an internal source of visible radiation and to uniformly illuminate the FOC object plane.

Once past the shutter, radiation impinges on a two element aplanatic optical system consisting of a spherical concave primary and an elliptical convex secondary mirror. This optical system magnifies the OTA focal plane by a factor of two for the new F/48 relay and four for the new F/96 relay with negligible spherical aberration or coma. The mirrors are all made of Zerodur and overcoated with Al + MgF_2 for a reflection efficiency exceeding 0.7 above 1200Å.

Near the exit pupil, in the new F/96 relay are located four independently commandable rotating filter wheels. Two such wheels are located at or near the exit pupil in the new F/48 relay. The filter wheels for the new F/96 relay each have 12 equidistant working positions while for the new F/48 relay each wheel has 8 equidistant positions. Each wheel has one clear position. These devices carry a full complement of wide, medium and narrow bandpass and neutral density filters, polarizing and objective prisms.

In order to fold the light beam back onto the detector and to focus the FOC, a cylindrical concave mirror is placed into the slowly converging beam past the filter wheels. This mirror also corrects for the residual off-axis OTA astigmatism and is made of the same materials as the primary and secondary mirrors. This mirror is mounted on a commandable focusing mechanism that allows it to internally compensate for variations in optical path length introduced by the OTA focus variations, FOC internal stability and by the differing optical thicknesses of the various optical elements on the filter wheels. The focusing mechanism changes the length of the optical path by ± 16 millimeters maintaining the position of the image on the detector typically within 0.05 millimeters whatever the location of the mirror along the stroke. The FOC focal plane is designed to coincide with the detector photocathode plane. The detector samples an area of 24.6×24.6 millimeter squared corresponding to 1024×1024 pixels, each $\simeq$ 24 micron squared in size, averaged over the field of view.

Absolute image position on the FOC focal plane can be referred to a grid of 17×17 reseau marks, each 75×75 microns squared in size evaporated on the inner surface of the photocathode MgF_2 window. The overall wavefront distortion of the FOC+COSTAR optical system is less than $\lambda/10$ for the new F/48 relay and the new F/96 relay at λ6328Å.

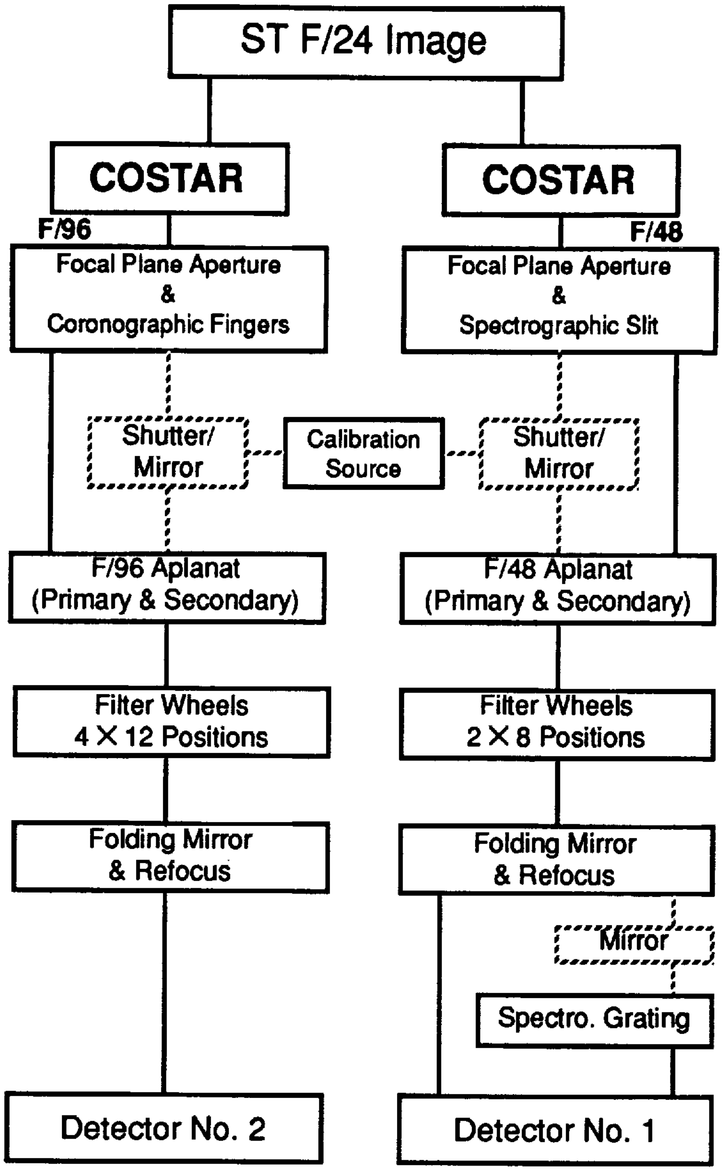

Figure 5. The Transfer Optics Block Diagram. The removable components are shown in the dashed frames.

In the new F/48 relay, the beam from the folding mirror may be relayed by a removable toroidal convex mirror to a fixed spherical concave reflection grating which re-images a spectrum of a portion of the field of view onto the detector photocathode. This portion contains a fixed width rectangular slit that is located on the entrance aperture (see Figure 9). The grating works with a divergent beam in the Rowland condition at fixed wavelength ranges in the first (3600–5400Å), second (1800–2700Å), third (1200–1800Å) and fourth (900–1350Å) order at a resolution $\lambda/\Delta\lambda \simeq 1000$. Only the 1150–1350Å portion of the fourth order spectrum can be measured in practice, of course, due to the MgF_2 cut-off of the detector.

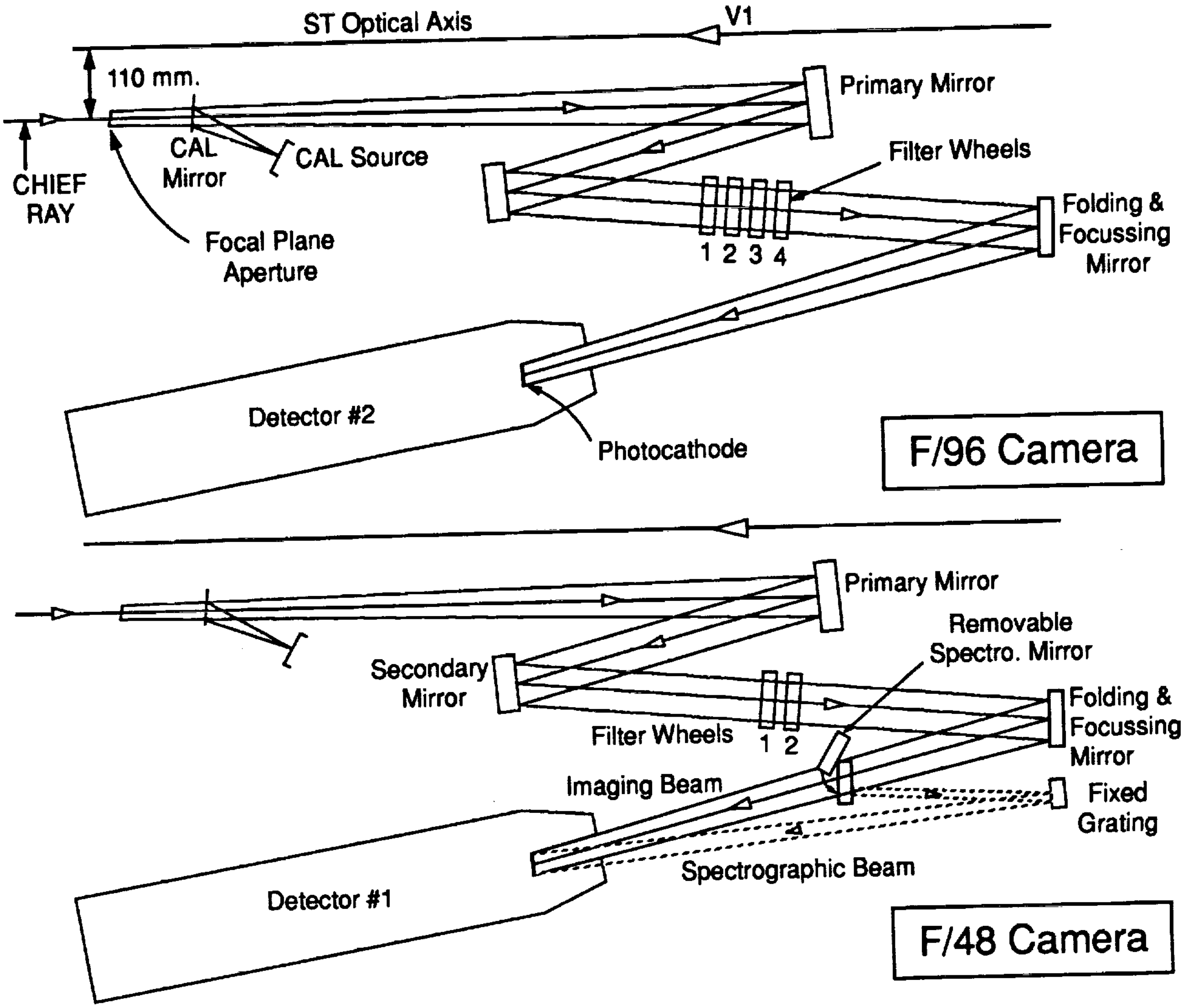

Figure 6. The schematic optical layout of the two cameras in the planes containing the V1 axis and the chief rays.

Wavelength range selection is accomplished by introducing suitable bandpass filters into the optical path of the new F/48 relay or by using the objective prism (FOPCD) whose dispersion axis is oriented at ≃ 90° to the grating dispersion direction as a cross disperser.

4.2 FOCAL PLANE APERTURES

The two FOC field defining entrance apertures are each located in a plane tangent to an OTA focal surface at the center point of the aperture. The center of each aperture is located at a linear distance of 110 millimeters from the V1 axis. Each FOC channel of COSTAR redirects part of the OTA field of view into an FOC entrance aperture. For the new F/96, the field is centered on a point 4.658 arcminutes from the V1 axis, while for the new F/48 the field is centered on a point 4.312 arcminutes from V1. The projections of these apertures onto the plane of the sky are shown in Figure 7; the dotted circles show the projection through the OTA only (i.e. the pre-COSTAR positions), while the solid circles are the new positions through the COSTAR+OTA optics. In this figure, the V1 axis runs into the paper at the center of the WFPC2 field of view and V1, V2, V3, U2, and U3 are the HST axes defined in the Call for Proposals and Proposal Instructions. The observant reader will notice that in Figures 8 and 9 the V2-V3 directions are reversed from previous versions of the FOC Handbook: this is because COSTAR forms an intermediate image between the M1 and M2 mirrors.

At the locations of the FOC entrance apertures, the OTA focal plane makes an angle of 10.05° with the normal to the ST axis. This plane is the object plane for the FOC optical relays. The COSTAR-corrected focal plane is inclined to this plane, which induces a field-dependent focus variation that is described more fully in Section 6.1.2. The axes of symmetry of the two FOC cameras D96 and D48 that run through the center of the apertures, perpendicular to and intersecting on the V1 axis form an angle of 30°. The D96 axis forms an angle of 30° with the +V2 axis and D48 an angle of 30° with the +V3 axis.

An expanded view of the two apertures in exactly the same perspective is shown in Figures 8 and 9. The camera aperture for the new F/96 relay is a circular diaphragm of 10.5 millimeters in diameter corresponding to 24 arcseconds on the sky in the COSTAR-corrected field, centered at point O with two 2 millimeter-long protruding opaque metal fingers oriented $\simeq 30^\circ$ to the D96 line and parallel to the V2 axis. The finger on the right is 0.112 millimeters thick (0.25 arcsecond in the sky) while the other is 0.223 millimeters thick (0.5 arcsecond in the sky). The directions of increasing sample (S) and line (L) numbers for the extended SDS format define the image coordinate system with its center at point C_{96}. This system is aligned with the X, Y reference system used to designate the orientation of the apertures on the sky in the Proposal Instructions. The corners ABCD of the 512 × 1024 zoomed format are marked on Figure 8. The large 14 × 14 arcsecond square marks the limit of the extended format. The opaque coronographic fingers are indicated by the hatched regions. The V1 axis is 4.658 arcminutes from O in the direction indicated to V1. The fully corrected field point for the new F/96 relay coincides with C_{96}.

The new F/48 entrance aperture is shown in Figure 9. The center O of the main aperture coincides with the center of the extended SDS format and lies on the sagittal focus while the center J of the slit lies on the tangential focus of the OTA.

Because of vignetting induced in the FOC by moving the OTA exit pupil from 7 meters to 530 millimeters from the new F/48 entrance aperture, it is not possible to have the center of the extended field unvignetted as well as all of the slit. The best compromise, which maintains the utility of the long slit as well as providing an imaging field useful for spectrograph acquisitions, was to move the optimally corrected field point from the center of the extended format to the point P, which is where the hypothetical extension of the slit would meet the edge of the extended imaging format. The default 512 × 512 imaging format has therefore

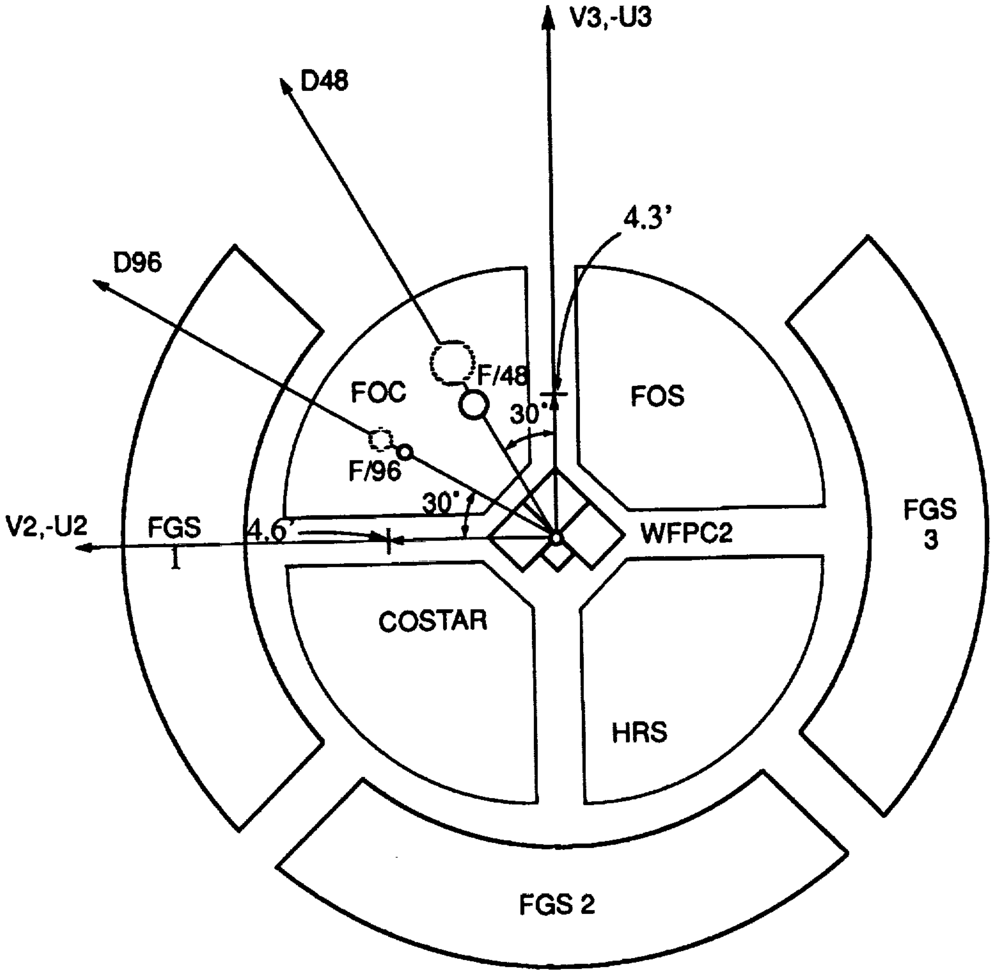

Figure 7. The location of the FOC entrance apertures on the HST focal plane projected onto the plane of the sky. In this perspective V1 is directed into the paper at the center of the WFPC2 pattern. V1, V2 and V3 form the HST right handed coordinate system defined in the Call for Proposals.

been moved to that corner of the extended format, and has been outlined in Figure 9. In this way, over half of the slit suffers less than 20% vignetting while the newly moved 512 × 512 imaging format is unvignetted over more than 80% of its area. Full vignetting contours are shown in Section 6.9.

The main aperture is essentially a circular diaphragm with a diameter of 21 millimeters corresponding to 48 arcseconds on the sky in the COSTAR-corrected field, except for an oblique truncation at points E and H. A thin, 0.15 arcsec wide opaque finger points to O from point G. A 5.689 millimeters (12.8 arcsecond) long, 0.028 millimeters (0.064 arcsecond) wide slit centered at J is located between points I and K. This slit forms the defining aperture of the spectrograph for the new F/48 relay. The corners of the 512z× 1024, 28 × 28 arcsecond

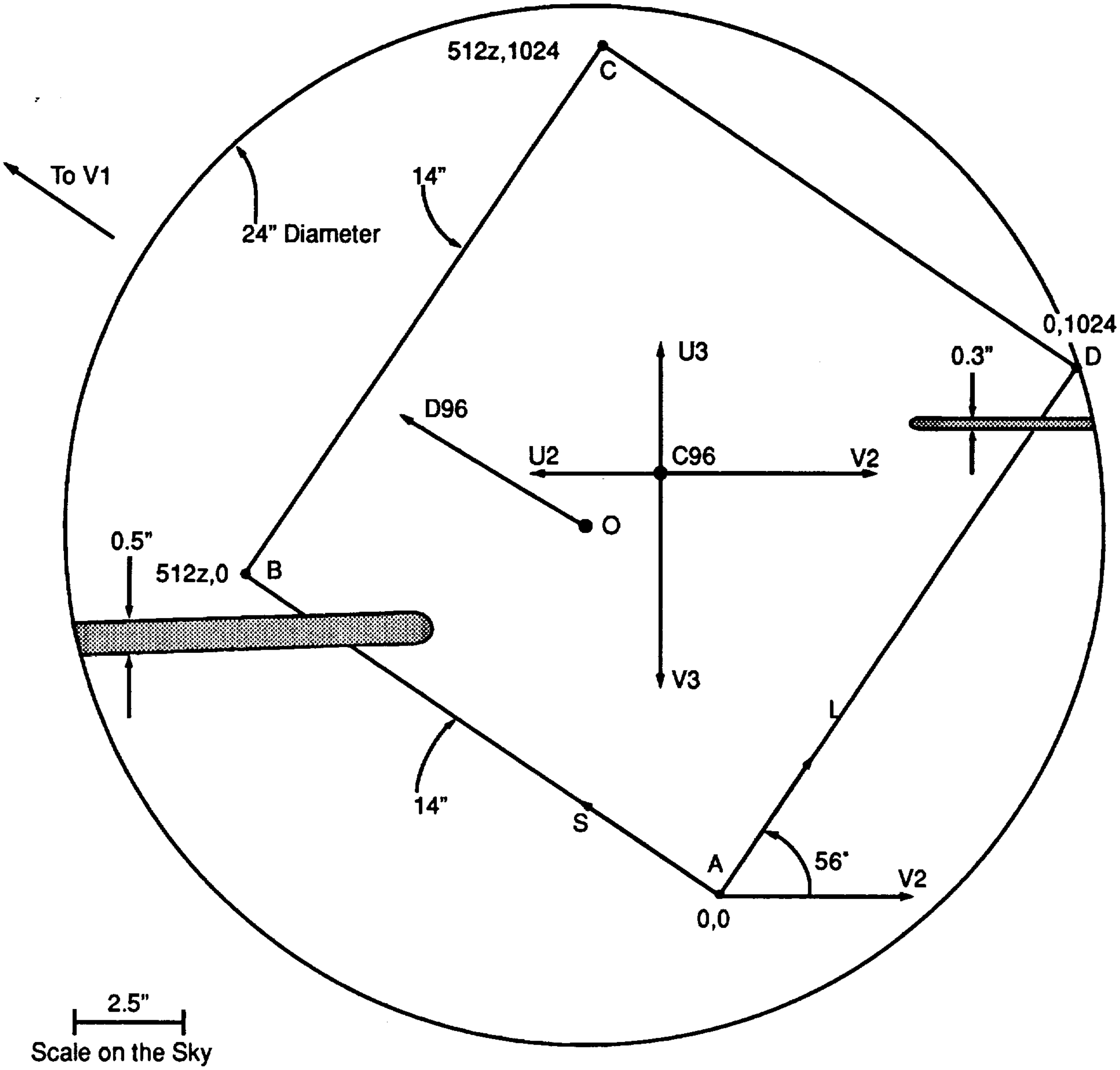

Figure 8. The camera entrance aperture for the new F/96 relay projected onto the sky.

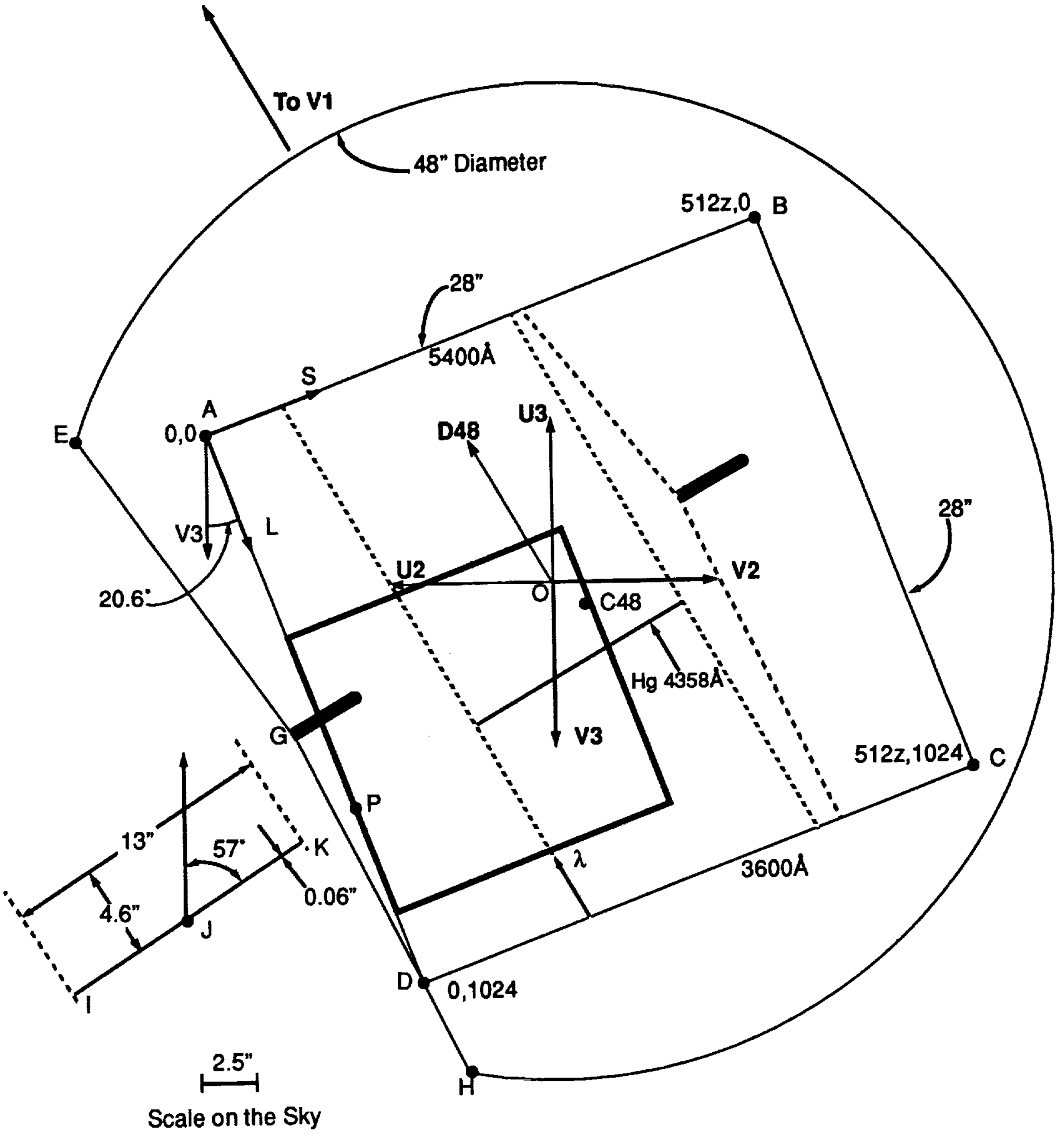

Figure 9. The camera entrance aperture for the new F/48 relay projected onto the sky. KI along the spectrograph slit coincides with the reference axis x that is used to designate the orientation of the apertures on the sky in the Proposal Instructions. The point P is the optimally corrected field point for the new F/48 relay and the new 512 × 512 imaging format is shown outlined with a **bold** line.

squared extended imaging format are given on Figure 9 as points A, B, C and D. When the spectrograph mirror is in place, the aperture is imaged onto the extended SDS format as shown in Figure 9 with the dashed lines representing the inner and outer edge of the spectrally dispersed image of the slit and the edge of the main aperture drawn for the specific case of the Hg line at 4358Å. The opaque target acquisition finger is indicated by the dark region. V1 is 4.312 arcminutes from P in the direction indicated to V1. A part of the dispersed main aperture falls in the right hand quarter of the extended format and may be eliminated by tailoring the observing format to the region inside the slit area. Wavelength increases in the direction indicated by λ from 3600Å to 5400Å in first order. Slitless spectroscopy can be performed in the clear region to the right of the dashed lines (see Section 3.6 and Figure A3 in the Appendix).

In order to predict with reasonable accuracy the location and orientation of an extended source in the FOC fields of view and to determine whether or when the required instrument orientations are compatible with the HST roll angle restrictions, it may be useful to locate with respect to the S, L axes on Figures 8 and 9 the celestial reference axes for that particular target and viewing configuration. To accomplish this, simply follow the procedures described in the Call for Proposals.

To specify a particular orientation of the apertures with the ORIENT special requirement of the exposure logsheets (see Proposal Instructions, section 7.2 for a more detailed description), place the object to be observed in the proper configuration on the entrance aperture shown in Figures 8 and 9. This will determine the desired positions of the N and E directions on the same apertures. The angle between these directions and the U3 axis drawn on these figures (measured E from N) is the angle to specify in this special requirement.

The aperture configurations described in this section for the F/96 correspond to the position determined during the first inflight calibrations of the FOC + COSTAR system. More similar calibrations will be performed in Cycle 4 to assess the stability of these positions. No inflight calibration has been performed for the F/48 yet. Actual images of the extended $512z\times$ 1024 pixels squared pre-COSTAR F/48, pre-COSTAR F/96, and pre-COSTAR F/48 spectrograph fields obtained in orbit with external flat field illumination of the FOC entrance apertures are shown in Figures A1–A3 in the Appendix. The extended format $512z\times$ 1024 pixel images have been dezoomed and displayed in a 1024 × 1024 pixel format. The occulting fingers, spectrograph slit, reseau marks appear clearly together with some blemishes and large scale response inhomogeneities. The latter are discussed in more detail in Section 6.9.

4.3 INTERNAL CALIBRATION SYSTEM

When the shutter is closed, an Al + MgF_2 mirror (see Figure 6) reflects the light beam from a light emitting diode (LED) calibration source into the optical path of the relay. The position of the source and the curvature of the mirror insure a quasi flat field illumination of the object plane. The unit consists of seven LEDs (two red, two yellow, two green and one blue) illuminating an integrating sphere. Their normalized emission spectra are shown in

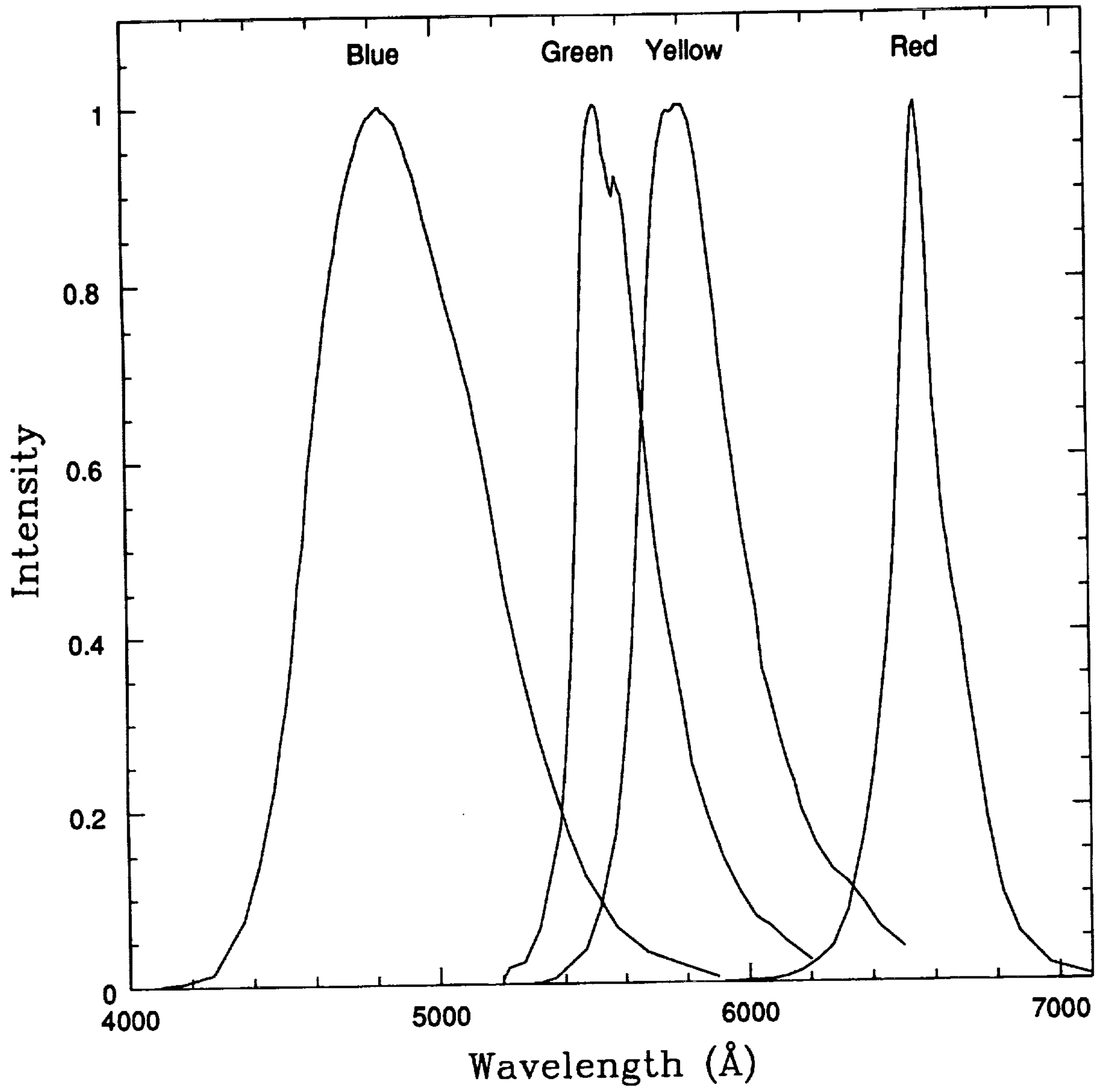

Figure 10. Normalized Emission Spectra of the Calibration LEDs.

Figure 10. The unit is capable of illuminating both calibration mirrors simultaneously. Each LED output can be set to 256 separately commandable intensity levels. The calibration system will be used to determine the detector's intensity transfer function, the uniformity of response, the FOC response to visible light and the geometric distortion. A ground-based comparison between external and LED flat field illumination of the detectors at the same wavelengths shows that the spatial variations of LED illumination are less than ±3% peak to peak over most of the field of view. The only exception is due to one edge of the circular mirror on the back of the shutter for the new F/48 relay preventing LED light from illuminating the upper left hand corner of the new F/48 frame. The calibration unit does not experience the same vignetting of an external source. This must be taken into account when

comparing internal and external flat fields. As mentioned previously, the F/96 detector is not expected to have any vignetting, nor is there any evidence of it. UV flat fields must be obtained by observing an external UV source since there is no onboard UV lamp. UV flat fields are currently obtained using observations of the inner region of the Orion Nebula.

4.4 FILTER WHEELS

The FOC has six commandable rotating filter wheels holding 58 optical elements and six clear apertures. Four wheels are on the the new F/96 relay and two on the new F/48 relay. The filter wheels of the new F/96 camera have 3 long pass, 9 wide band, 20 medium band, 2 narrow band and 5 neutral density filters. They also contain 3 polarizers and 2 objective prisms. The filter wheels of the new F/48 relay contain 3 long pass, 8 wide band, and 3 objective prisms. A complete list of the optical elements ordered by increasing peak wavelengths λ_o is given in Table 3 for the filters of the new F/96 relay and in Table 4 for the filters of the new F/48 relay. In these tables, FW indicates the filter wheel number (1-4 for the new F/96, 1-2 for the new F/48), ID the filter identification code, λ_0 the wavelength at the peak of the curve representing the product of the filter transmission (T) with the OTA + FOC response function, (Q) described in Section 6.3, $\Delta\lambda$ the full width at half maximum of this curve, and $T(\lambda_0)$ is the filter transmission at λ_0, and $QT(\lambda_0)$ is $T(\lambda_0)$ multiplied by Q. Δm gives the magnitudes of attenuation of the neutral density filters at 3000Å. These filters are placed on the wheels in such a way as to allow beam attenuation in increments of 1 magnitude from 1 to 9 magnitudes.

The filter wheel system of the new F/96 camera allows, in principle, up to 12^4 or 20,736 and up to 8^2 or 64 different combinations of optical elements for the new F/48 relay. Clearly, only a fraction of these will find a useful astronomical application. Observing configurations requiring more than one filter on the same wheel are not possible, of course. Filter positions on the wheels were carefully selected in order to minimize this possibility. The time required to change some filter combinations may reach 3 minutes. This implies a considerable expense in overhead time for programs requiring extensive cycling between filters.

4.4.1 Bandpass and Neutral Density Filters

In general, the long pass filters are Schott colored glass combined with a low pass filter, the wide band filters are metallic UV filters, the medium band filters are multi-dielectric multi-element with ZnS-Th F_4 layers, and the interference filters are multi-dielectric multi-element with ZnS chiolithe layers. The measured transmission versus wavelength curves for all filters and attenuators for the new F/96 relay and the new F/48 relay are shown in Figures 11–15.

In order to suppress ghost images, the external faces of all mono-element filters are parallel to within 5 arcseconds or better. For multi-element filters the tolerance is 1 arcminute. The cemented elements have a wedge angle of 1° or less. In order to minimize losses in the modulation transfer function, the external faces are flat to $\lambda/5$ peak to peak at 6300Å and

Table 3: New F/96 Optical Element Characteristics Ordered by Peak Wavelength

FW	ID	λ_0(Å)	$\Delta\lambda_0$(Å)	T(λ_0)	QT(λ_0)	Comments
3	F120M	1230	82	0.10	0.0009	Medium band
3	F130M	1280	88	0.10	0.0010	Medium band
2	F140W	1370	298	0.21	0.0029	Wide band
3	F140M	1400	178	0.08	0.0011	Medium band
3	F152M	1500	184	0.08	0.0012	Medium band
3	F165W	1700	910	0.28	0.0042	Wide band
3	F170M	1760	184	0.18	0.0025	Medium band
2	F175W	1730	716	0.24	0.0039	Wide band
3	F195W	2110	946	0.42	0.0091	Wide band
3	F190M	2000	276	0.15	0.0027	Medium band
3	F210M	2156	214	0.18	0.0048	Medium band
2	F220W	2280	480	0.39	0.0127	Wide band
3	F231M	2330	228	0.18	0.0067	Medium band
4	F253M	2550	236	0.18	0.0087	Medium band
2	F275W	2770	594	0.40	0.0227	Wide band
4	F278M	2800	316	0.26	0.0153	Medium band
4	F307M	3080	328	0.26	0.0187	Medium band
4	F130LP	3750	2202	0.92	0.0731	Long pass ($\lambda \geq 1300$Å)
2	F320W	3360	844	0.89	0.0695	Wide band, image shift of ≅85 pixels
2	F342W	3410	702	0.81	0.0633	Wide band, U filter
4	F346M	3480	434	0.58	0.0453	Medium band, u filter
4	F372M	3710	406	0.73	0.0573	Medium band, bar in PSF(see Fig 25c.)
2	F430W	3940	832	0.74	0.0544	Wide band, B filter
2	F370LP	4020	984	0.83	0.0580	Long pass ($\lambda \geq 3700$Å)
4	F410M	4100	194	0.58	0.0391	Medium band, v filter
4	F437M	4290	438	0.71	0.0406	Medium band, ghost
4	F470M	4710	212	0.79	0.0257	Medium band, b filter
2	F486N	4870	34	0.63	0.0180	Interference filter centered on H_β line
4	F502M	4940	530	0.82	0.0222	Medium band, ghost
2	F501N	5010	74	0.68	0.0175	Interference filter centered on [O III],ghost
2	F480LP	5100	744	0.82	0.0212	Long pass ($\lambda \geq 4800$Å), V filter
4	F550M	5460	188	0.77	0.0108	Medium band, y filter
1	F600M	5800	410	0.8	0.0068	Medium band

Table 3: New F/96 Optical Element Characteristics Ordered by Peak Wavelength

FW	ID	λ_0(Å)	$\Delta\lambda_0$(Å)	$T(\lambda_0)$	$QT(\lambda_0)$	Comments
1	F630M	6382	208	0.67	0.0010	Medium band
1	CLEAR	3700	2208	1.0	0.0962	Clear aperture
1	F8ND	3440	2100	9×10^{-4}	7×10^{-5}	Neutral density, $\Delta m = 8.0$
1	POL120	3700	2180	0.91	0.0728	Polarizer, 120°
1	F2ND	3400	2176	0.19	0.0156	Neutral density, $\Delta m = 2.0$
1	POL0	3700	2180	0.92	0.0730	Polarizer, 0°
1	F4ND	3400	2176	0.03	0.0024	Neutral density, $\Delta m = 4.0$
1	F6ND	3200	2348	0.005	0.0003	Neutral density, $\Delta m = 6.0$
1	PRISM2	3700	2124	0.94	0.0742	Near UV objective prism (NUVOP)
1	POL60	3740	2076	0.92	0.0740	Polarizer, 60°
1	PRISM1	3700	2232	0.94	0.0740	Far UV objective prism (FUVOP)
3	F1ND	3400	2162	0.39	0.0300	Neutral density, $\Delta m = 1.0$

Table 4: New F/48 Optical Element Charactersitics Ordered by Peak Wavelength

FW	ID	λ_0(Å)	$\Delta\lambda_0$(Å)	$T(\lambda_0)$	$QT(\lambda_0)$	Comments
1	F140W	1320	300	0.20	0.005	Wide band
1	F150W	1400	628	0.23	0.007	Wide band
1	F175W	1730	678	0.18	0.004	Wide band
1	F195W	2110	1076	0.36	0.013	Wide band
1	F220W	2250	480	0.36	0.018	Wide band
2	F275W	2750	656	0.29	0.019	Wide band
2	F130LP	3400	2722	0.94	0.062	Long pass ($\lambda \geq 1300$Å)
2	F180LP	3400	2702	0.92	0.061	Long pass ($\lambda \geq 1800$Å)
2	F342W	3400	706	0.83	0.055	Wide band, U filter
1	F305LP	3450	1692	0.92	0.059	Long pass ($\lambda \geq 3050$Å)
2	F430W	3950	938	0.75	0.043	Wide band, B filter
1	CLEAR	3400	2732	1.0	0.066	Clear aperture
1	PRISM3	3360	2722	0.96	0.064	Far UV Cross Disperser Objective Prism (FOPCD)
2	PRISM2	3400	2704	0.88	0.058	Near UV Objective Prism (NUVOP)
2	PRISM1	3400	2738	0.96	0.064	Far UV Objective Prism (FUVOP)

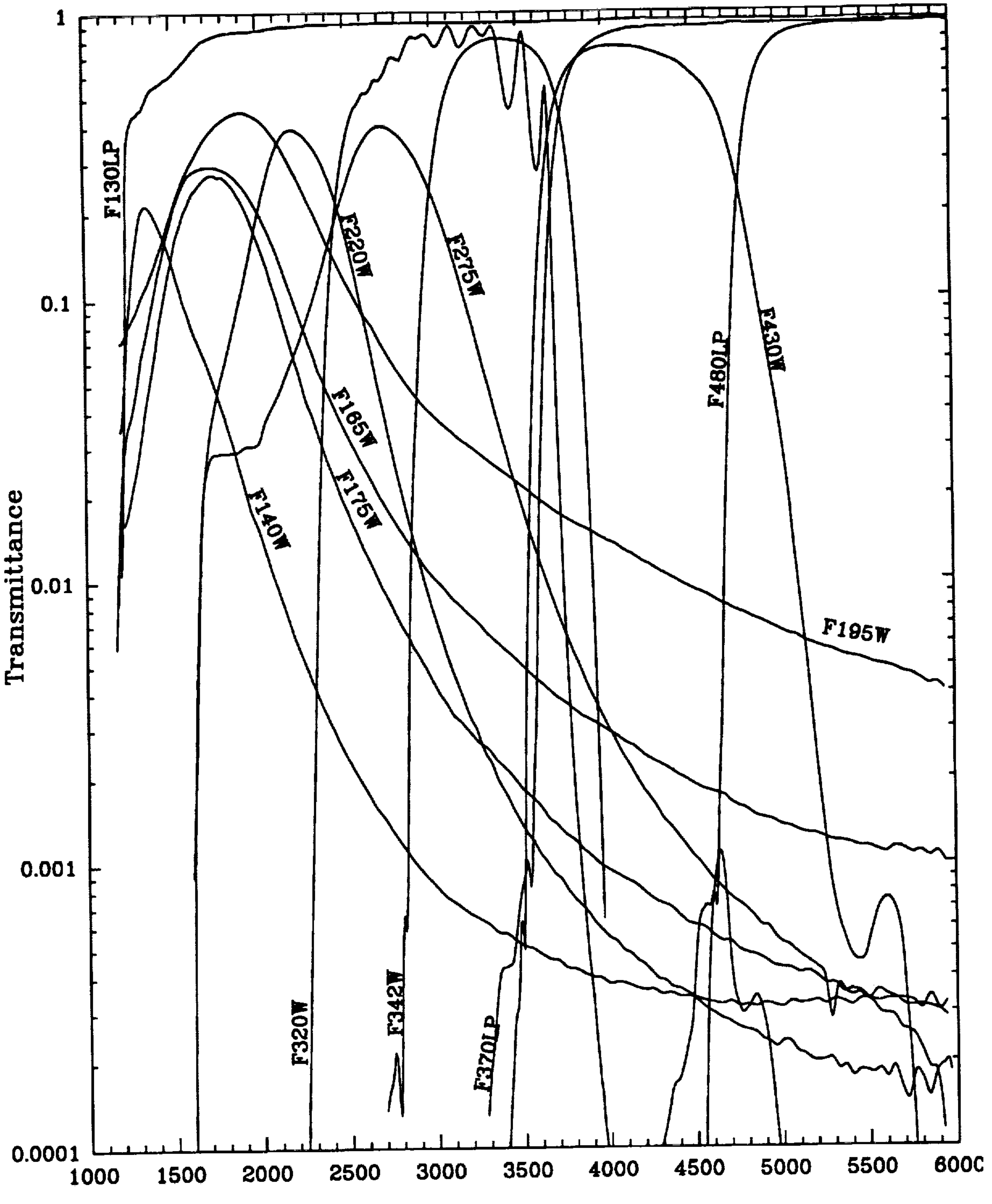

Figure 11. Transmittance of the long pass and wide band filters on the filter wheels of the new F/96 relay as a function of wavelength.

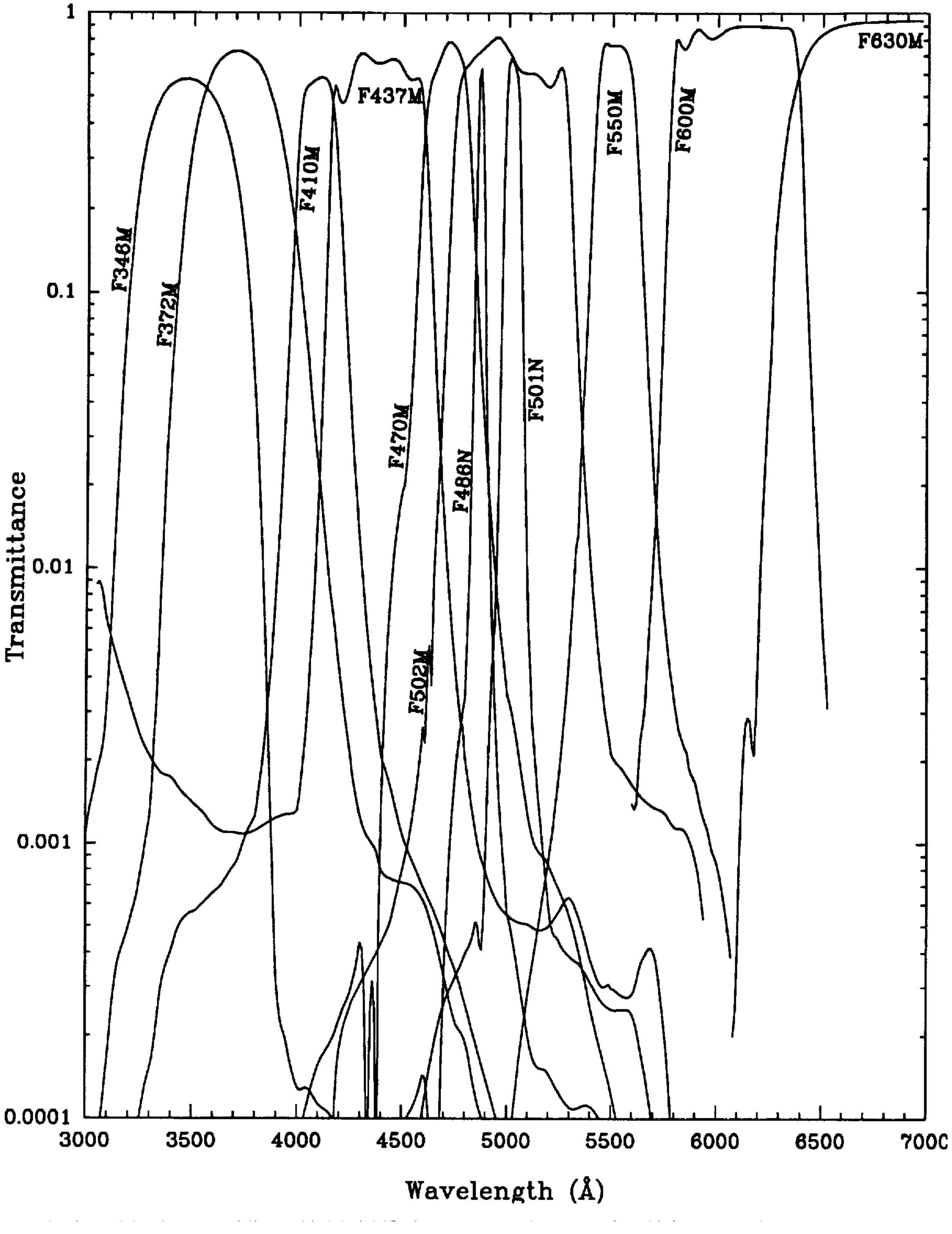

Figure 12. Transmittance of the visible medium and narrow band filters in the filter wheels of the new F/96 relay as a function of wavelength.

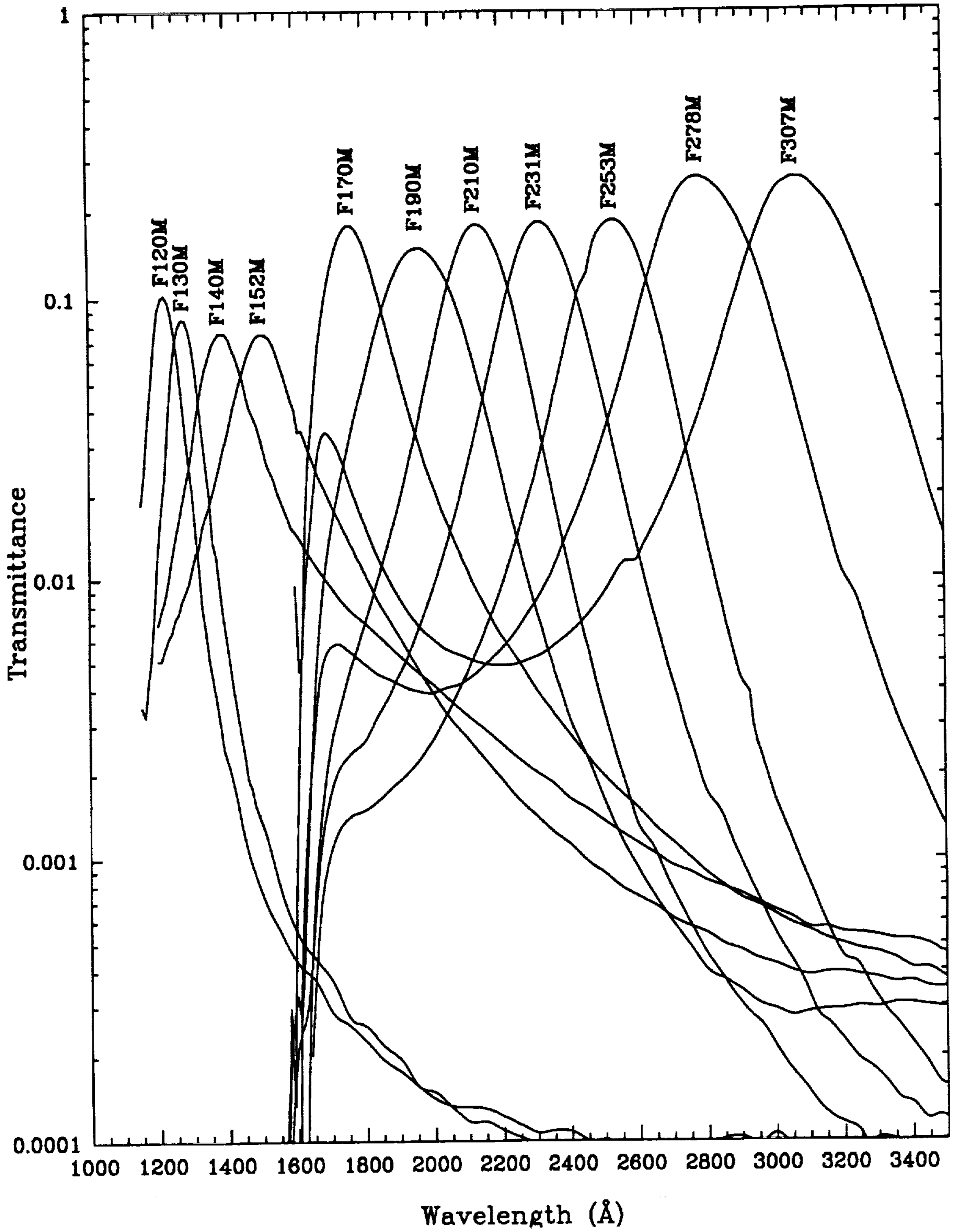

Figure 13. Transmittance of the UV medium band filters on the filter wheels of the new F/96 relay as a function of wavelength. The F120M and F130M filter transmission curves remain essentially flat at 10^{-4} beyond $\simeq$ 2500Å.

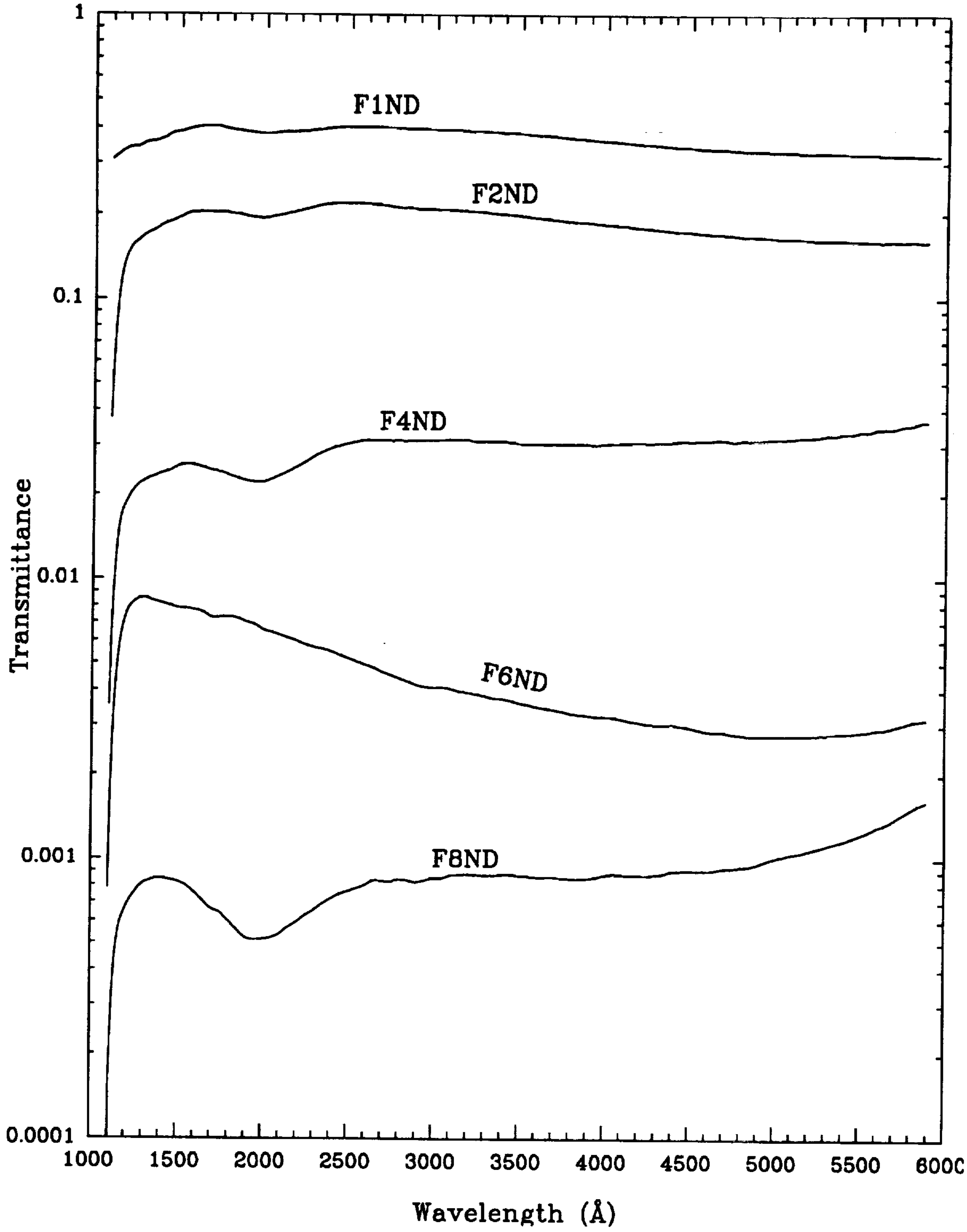

Figure 14. Transmittance of the neutral density filters on the filter wheels of the new F/96 relay as a function of wavelength.

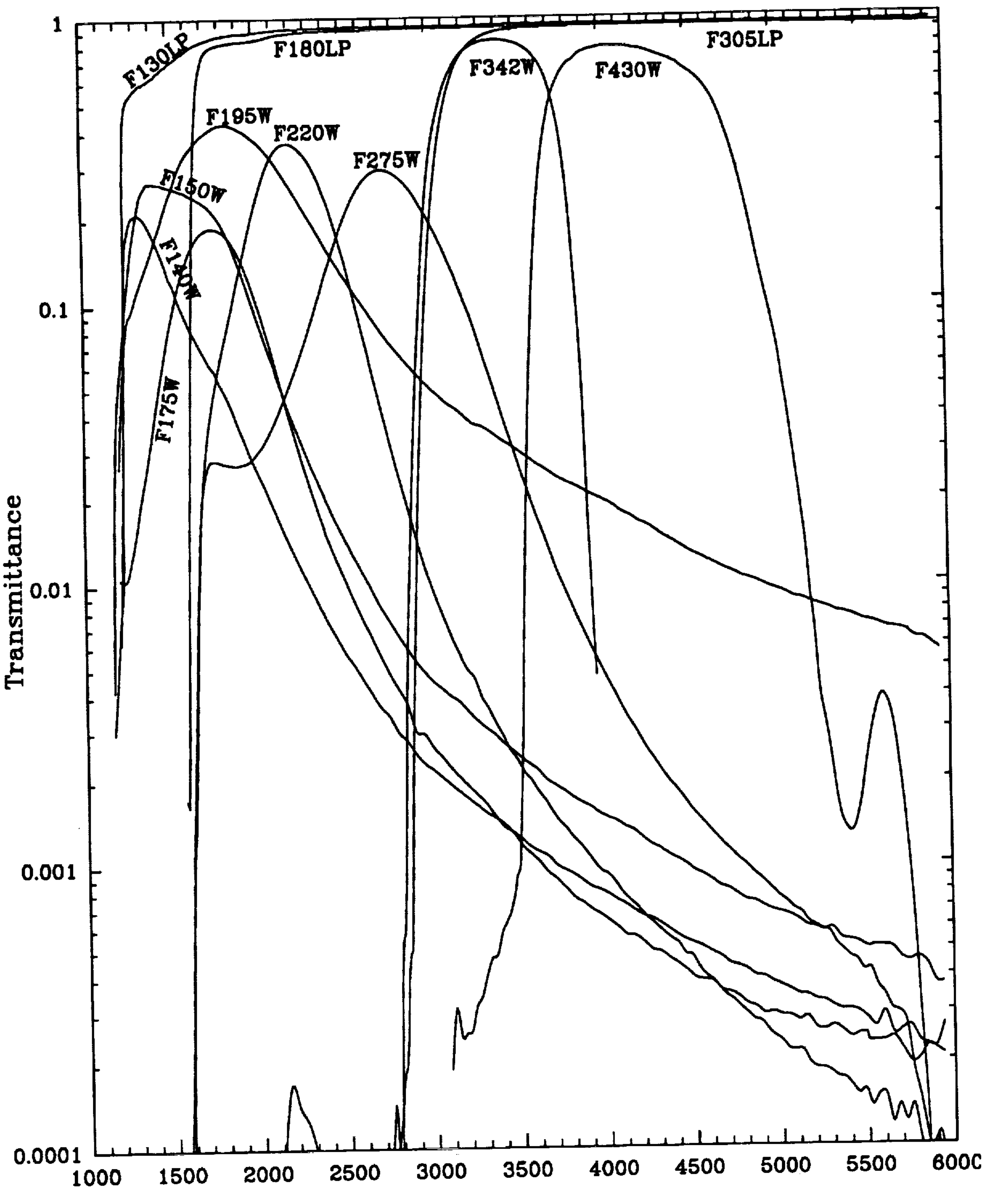

Figure 15. Transmittance of all the filters on the filter wheels of the new f/48 relay as a function of wavelength.

the internal faces in the multi-element filters are flat to $\lambda/2$ peak to peak. The refractive index is homogeneous to a level of $\Delta n < 2 \cdot 10^{-5}$ to be consistent with the $\lambda/5$ flatness constraint. These conditions have been complemented by the introduction of appropriate tilt angles of the different filter wheels themselves. Transmission non-uniformities are held to within ±5% over the whole surface. Ground tests of the FOC with a point source projector have been performed with all filters. A few have been found to exhibit faint ghost images and image shifts. These filters are flagged in the Comments column.

4.4.2 Objective Prisms

The objective prisms consist of either a single 30 millimeter diameter, 3 millimeter thick wedged crystal of MgF_2 (the FUVOP and FOPCD, called PRISM 1 and PRISM 3 in the Instructions) or a combination of two wedged crystals of MgF_2 and SiO_2 glued together (the NUVOP called PRISM 2 in the Instructions). The former operates down to 1150Å with a wavelength resolution $\lambda/\Delta\lambda \simeq 50$ at 1500Å while the latter has a dispersion $\lambda/\Delta\lambda \simeq 100$ at 2500Å but transmits only above $\simeq$ 1600Å. All of the prisms disperse in a direction oriented roughly anti-parallel to the increasing line number (L) direction except FOPCD on FW # 1 of the new F/48 camera that, instead, disperses in a direction roughly perpendicular to L or about 90° to the others. This last one is meant as a cross disperser (CD) for the long slit spectrograph (see Section 4.5). The MgF_2 prisms (FUVOP and FOPCD) on the new F/48 relay (Prisms 1 and 3) are both preceded by a 3 mm. thick CaF_2 window in order to reduce geocoronal Lyman alpha contamination. These prisms, therefore, have negligible transmissions below $\simeq$ 1250 Å.

The essential features of the FOC objective prism facility are listed in Table 5 and illustrated schematically in Figure 16 for the FUVOP of the new F/96 relay. The left hand side of this diagram corresponds to a view of the extended format for the new F/96 relay in the same orientation as the one shown in Figure 8 and approximately to scale. The direction of dispersion of the prism is represented by the vector $\vec{I}$ emanating from the center C_{96} of the format and making an angle θ with $-L$ with θ increasing clockwise from $-L$. The spectrum of an object located at C_{96} will lie along the line defined by $\vec{I}$. The position of any specific wavelength is defined then by giving the linear coordinate x in pixels from C_{96} on this line with negative values for positions above C_{96} (towards $+L$), positive below it (towards $-L$) consistent with the $\vec{I}$ directions shown in Figure 16.

A blow-up of this spectrum extending from 1200 to 6000 Å as dispersed by the FUVOP is shown on the right hand side of this figure where the solid curve gives the position x along $\vec{I}$ of any wavelength for this case. The reciprocal of the slope of this curve yields the resolution R in Å/pixel given in the figure for several representative wavelengths. Values of the linear coordinate $x(\lambda)$, $R(\lambda)$, $T(\lambda)$ the transmission of the prism and the value of θ for each prism is listed in Table 5 as a function of wavelength. Please note that the angle θ for the prisms of the new F/96 relay increases clockwise from $-L$ while it increases counterclockwise from $-L$ for the prisms of the new F/48 relay due to the different orientation of the new F/48 format shown in Figure 9. The position of the entire dispersed FOV with respect to the undispersed

FOV is also shown in Figure 16. The former is displaced upwards by 5.88 millimeters at the red limit at 6000Å at the upper edge and 9.96 millimeters at the far UV limit at 1200Å at the lower edge of the field.

A composite image showing the central 256 × 512 pixels of the undispersed image of a star in the post-COSTAR F/96 256 × 1024 image and its associated Far-UV objective prism spectrum is shown in Figure A4 in the Appendix. In this 256 × 1024 centered format, the star was placed well below the center of the format so that in the next image, the dispersed FUVOP spectrum is roughly centered. The two images were then co-added to produce Figure A4. It should also be apparent from an inspection of Figure 16 and Table 5 that careful consideration must be given to the positioning of the format and/or the target object in the format in order to ensure that the ensuing spectrum falls on the correct part of the frame. This is especially critical for the FUVOP's that have a large offset and a spectrum length which is a sizable fraction of a typical field of view. The simplest way to handle this problem is through judicious use of the POS TARG special requirement described in the Proposal Instructions. Suppose, for example, that one desires to place a particularly interesting feature in the spectrum of an object located at ≃ 1500 Å close to the center of the image for the new F/96 relay listed in Table 6 using the FUVOP. According to the data given in Table 5 and the situation illustrated in Figure 16, one would specify a POS TARG 0, −4.4 because 1500Å falls 312 pixels or 4.37 arcseconds from the undispersed position of the object in the positive Y(or L) direction specified on Figure 10.2 of the Proposal Instructions.

4.4.3 Polarizers

The FOC polarimeter consists of three MgF_2 double Rochon prisms located on FW1 in the new F/96 relay. Each prism consists of an optically contacted double Rochon prism combination acting as a three element birefringent beam splitter. The pass directions of the prisms are at 0°, 60°, and 120°, counterclockwise from the image X axis (−S direction) as projected onto the sky. A schematic drawing of the device is shown in Figure 17.

The optical axes of the outer components A and B are oriented perpendicular to the optical beam axis while the central component C has its optical axis parallel to the beam axis. The entrance face is at the base of the central prism. In this configuration, the ordinary ray is transmitted without deviation while the extraordinary rays are deviated by the interface between the outer and central prisms. Thus, three exit beams emerge from the polarizer. The orientation of polarization is parallel to the face of the octagon to within ± 5 arcminutes and the external faces are parallel to within ± 5 arcseconds. This insures that the wavefront distortion is less than $\lambda/10$ at λ 6328Å. The beam deviation δ depends on the ordinary and extraordinary indices of refraction and the prism wedge angle. These parameters were chosen such that the angular separation of the beams will yield a central undeviated 11 arcseconds squared image without overlap of the two orthogonally polarized beams. Thus, $\delta = 1.155°$ for λ =1300Å and 1.165° for λ =6328Å. In these conditions, the images on the focal plane of the new F/96 relay will be located as shown in Figure 18 for the three prisms.

Table 5: FOC Objective Prism Characteristics

F/96 FUVOP θ = 9° x(pix); R(Å/pix) T	F/96 NUVOP θ = 6° x(pix); R(Å/pix) T	F/48 FUVOP θ = 12° x(pix); R(Å/pix) T	F/48 NUVOP θ = 12° x(pix); R(Å/pix) T	F/48 FOPCD θ = 100° x(pix); R(Å/pix) T	λ(Å)
-431;1.7 0.44					1200
-374;2.4 0.58		-183;5.1 0.61		-208;5.1 0.62	1300
-350;4.1 0.64		-168;8.8 0.69		-191;8.8 0.70	1400
-325;5.6 0.73		-159;13.7 0.76		-181;13.7 0.76	1500
-314;9.3 0.85		-153;19.5 0.82		-174;19.5 0.82	1600
-303;11.7 0.88		-149;25.9 0.86		-169;25.9 0.86	1700
-297;15.9 0.91	-353;0.7 0.77	-145;33.0 0.9	-50; 0.78	-165;33.0 0.9	1800
-290;19.1 0.92	-238;1.1 0.79	-142;40.7 0.92	-46; 0.79	-161;40.7 0.91	1900
-286;23.9 0.93	-161;1.7 0.8	-140;49.2 0.92	-32;15.7 0.8	-159;49.2 0.92	2000
-282;29.6 0.95	-108;2.1 0.82	-138;58.6 0.94	-19;10.5 0.82	-157;58.6 0.93	2100
-280;38.8 0.95	-69;3.0 0.83	-137;69.0 0.95	-11;11.6 0.84	-156;69.0 0.94	2200
-272;50.4 0.96	1.6;4.4 0.86	-133;107.6 0.96	5;20.9 0.86	-151;107.6 0.96	2500
-265;92.3 0.96	62;11.7 0.88	-130;203 0.96	23;41.8 0.88	-148;203 0.96	3000
-261;161 0.94	99;18.7 0.94	-128;348 0.97	33;67.9 0.89	-145;348 0.96	3500
-259;279 0.94	123;25.4 0.94	-127;55 0.98	40;99 0.89	-144;554 0.97	4000
-257;526 0.94	153;38.5 0.94	-125;1192 0.98	47;168 0.89	-142;1192 0.97	5000
-255;1562 0.92	168;70.4 0.9	-125;2192 0.98	52;247.5 0.85	-142;2197 0.85	6000

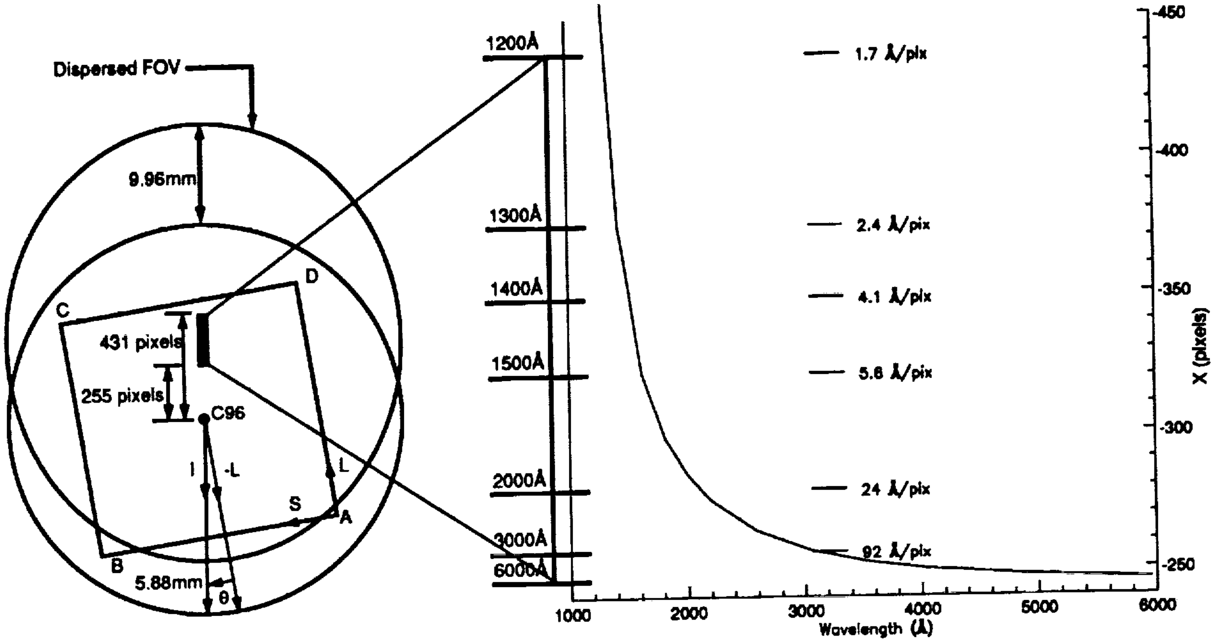

Figure 16. Optical layout of the focal plane of the new F/96 relay with the FUVOP inserted in the beam. The star is assumed located at C_{96} in the entrance aperture of Figure 7.

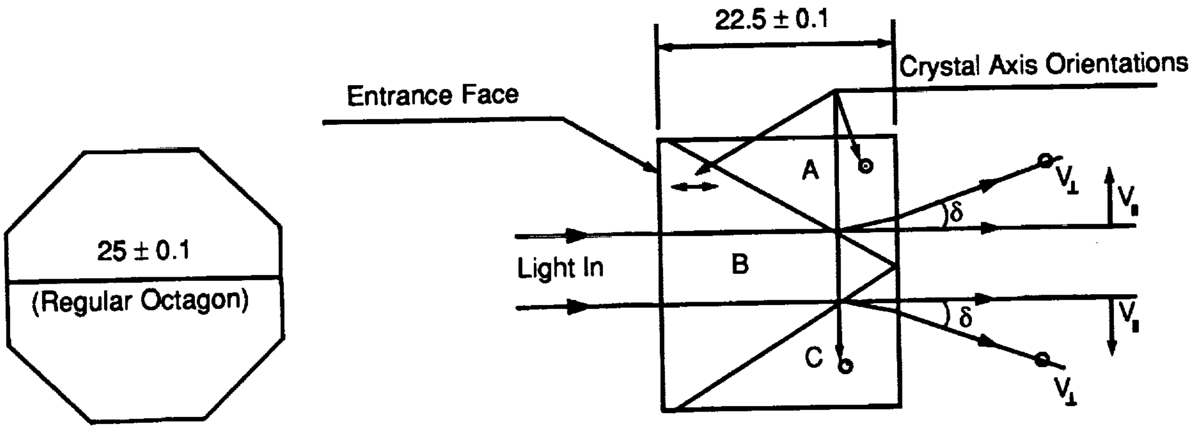

Figure 17. The Physical Layout of the FOC Polarizers. Dimensions are in millimeters.

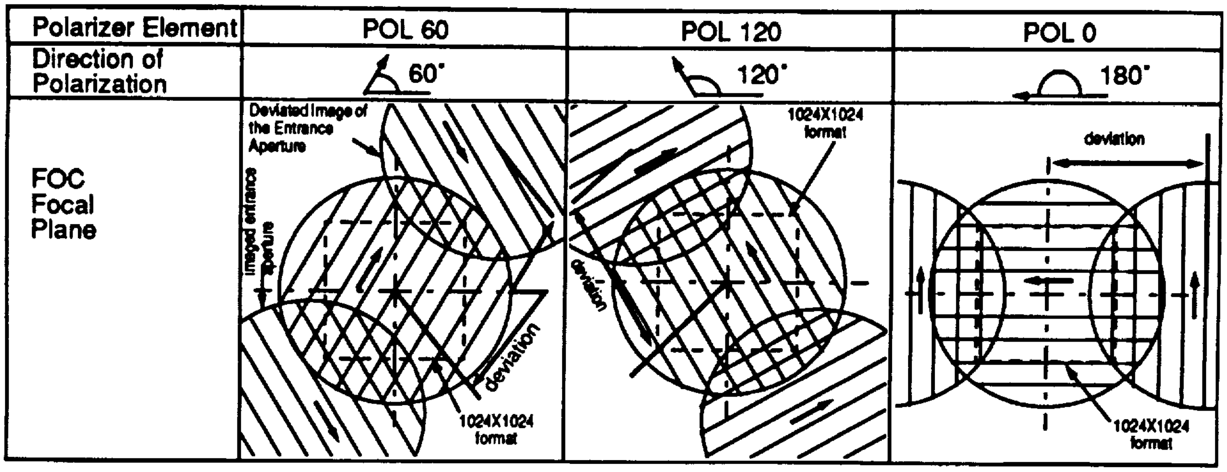

Figure 18. Image configurations on the focal plane of the new F/96 relay for the three polarizers.

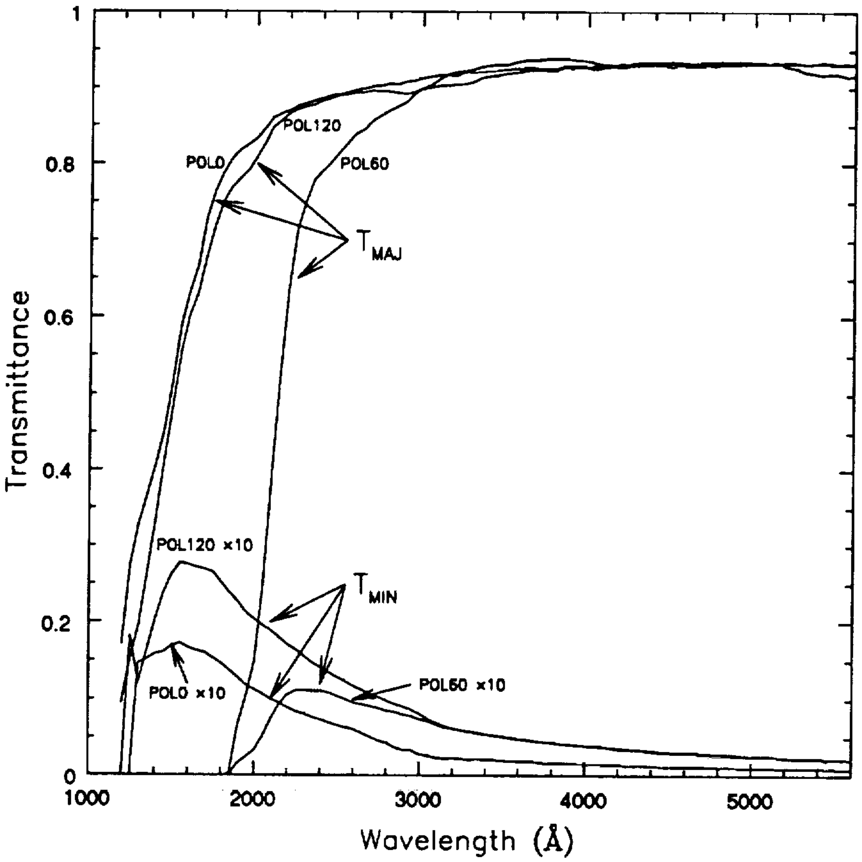

Figure 19. The major principal transmittance T_{MAJ} and the minor principal transmittance T_{MIN} of the three FOC polarizers as a function of wavelength.

The major principal transmittance (T_{MAJ}) of the undeviated beam through the three prisms and the minor principal transmittance (T_{MIN}) of the normal nonpolarized light are given in Figure 19. Notice that one of the polarizers (POL60) does not transmit below ≃ 1800Å. There are limitations on the accuracy which is attainable with this facility. A major factor is that the three different polarizers have somewhat different throughputs, even longward of 3000 Angstroms. While the filter transmissions have been measured, filters do change with time, and color variations in the source will result in small differences in the actual throughput. In addition, the light reaches the polarizers only after reflection off the OTA, COSTAR and the FOC primary and secondary mirrors (but before the fold mirror). Each of these six reflections is at a non-zero angle of incidence, ranging from a few minutes of arc for the OTA primary to about 11.5 degrees for the FOC secondary. Such reflections introduce a phase shift in incident polarized light and a slight instrumental polarization, but these effects are below the calibration accuracy. The reflections off the COSTAR optics are at angles of incidence that are comparable to the angles for the FOC optics, so we expect the polarizers to perform as well as before COSTAR. At the time of the writing, post-COSTAR calibration of the F/96 polarizers has not yet been performed.

4.5 LONG SLIT SPECTROGRAPHIC FACILITY

Due to the high background count rate and high-voltage turn-on problems which have occurred in the F/48 relay (see Section 6.4), the F/48 camera will not be made available in Cycle 5, pending further testing and data analysis.

This facility consists of the following four elements:

1. a rectangular (0.063 × 12.5 arcsecond) slit placed on the new F/48 camera entrance aperture at the OTA tangential focus as shown in Figure 9,
2. order sorting bandpass filters and/or a cross dispersing objective prism on the filter wheels of the new F/48 relay,
3. a removable toroidal convex mirror which picks off the new F/48 beam between the folding mirror and the DHU and reflects it towards
4. a fixed spherical concave reflection grating which reimages the slit spectrum onto the detector photocathode as shown in Figure 6.

The last two optical elements are slightly tilted and decentered with respect to the optical relay axis of the new F/48 in order to center the spectrum of the slit onto the photocathode. Since, as shown in Figure 9, the slit is considerably offset from the extended 28 × 28 arcseconds squared normal imaging field, its image falls outside the scanned area of the photocathode in the normal imaging mode. Only when the convex mirror is placed into the new F/48 beam does the dispersed image of the slit become visible on the scanned area in the position indicated in Figure 9. The effective wavelength range of the device in first order is 3600–5400Å, in second 1800–2700Å, in third 1200–1800Å and in fourth 900–1350Å. The MgF_2 window of the detector limits this last range to 1150-1325Å.

The spectrograph mirror and the grating are both made of Zerodur overcoated with Al + MgF_2 with a reflection efficiency exceeding 0.7 beyond 1200Å. The grating is ruled with 150 grooves mm^{-1} and a blaze angle of 1.94° for maximum efficiency at 4500Å in first order. Its radius of curvature is 94cm and the angle of diffraction is 2.6°. This implies a linear dispersion at the photocathode of 71, 36, 24, and 18 Å mm^{-1} and, with a beam diameter of $\simeq$ 20 mm., a theoretical resolving power of $\simeq$ 3000, 6000, 9000 and 12000 for the four orders, respectively. The FOC spectrograph resolution, however, is limited, in practice, by the slit size and the OTA Point Spread Function (PSF) that correspond to $\simeq$ two to three 24 micron pixels. Using the Rayleigh resolution criterion, the actual resolving power of the instrument is $\simeq$ 1150 in all orders with a spectral resolution of 4, 2, 1.3, and 1Å for first, second, third, and fourth orders respectively. These values have been confirmed by ground-based calibration using line source stimulation.

Both the spectrograph mirror and the grating work with unit magnification. The convex mirror corrects the astigmatism introduced by the spectrograph's optical elements. The resulting image is nearly free of astigmatism and image tilt with respect to the photocathode plane. The fixed grating configuration of the long slit spectrograph implies that light from all orders falls simultaneously on the same area of the detector. Because of the limitations of the UV bandpass filters, any order may be contaminated with light from another, resulting in possible ambiguities in line identification and degradation of achievable signal to noise ratio (S/N) due to line or continuum overlap. This can be a serious problem in some applications, especially those involving objects with a bright visible spectrum where the spectrograph's overall quantum efficiency peaks.

Even in the most complicated situations, however, it is still possible, at least in principle, to separate the different orders by executing a number of exposures with judiciously chosen bandpass filters. Light from the first order, for example, can be unambiguously identified by means of the F305LP filter that completely blocks radiation below 3000Å. Since the filter transmissions are well known, shorter wavelength information can be recovered from a confused spectrum by appropriately subtracting the calibrated data. The F220W for the second order, F150W for the third and F140W for the fourth may be considered as the standard FOC spectrograph order sorting filters but others may be selected, at the discretion of the observer, instead of or in addition to these for more specialized applications. This procedure can always be used at the expense of increased observation time required by the multiple exposures and of degraded S/N due to the effectively increased background uncertainty. For extended sources larger than 1.6 arcsecond in size this is the only viable alternative.

For objects of limited spatial extent (including point sources), the four overlapping orders can be spatially separated by using the FOPCD objective prism as a cross disperser. The position of the four orders on the detector field of the new F/48 relay in this case is shown in Figure 20. The prism dispersion direction PD is orthogonal to the grating dispersion direction GD and close to antiparallel to the increasing sample number direction S. The reader is referred to Figure 9 for a broader perspective of this viewing configuration. The largest achievable physical separation between orders is 7 pixels (0.20 arcseconds) between the first (I) and second (II), 15 pixels (0.42 arcseconds) between the second and third (III) and 36 pixels (1.01 arcseconds) between the third and fourth (IV) order. The background is significant only for wavelengths which are harmonics of bright geocoronal lines like OI, 1304Å. This option is very attractive because of its high efficiency due to the spectral multiplex gain of a factor of 4 and to the gain of a factor of 3 – 5 resulting from the elimination of the bandpass filters. The CaF_2 blocking filter on the FOPCD effectively removes the contaminating effect of the bright geocoronal line at Lyman α at 1216Å.

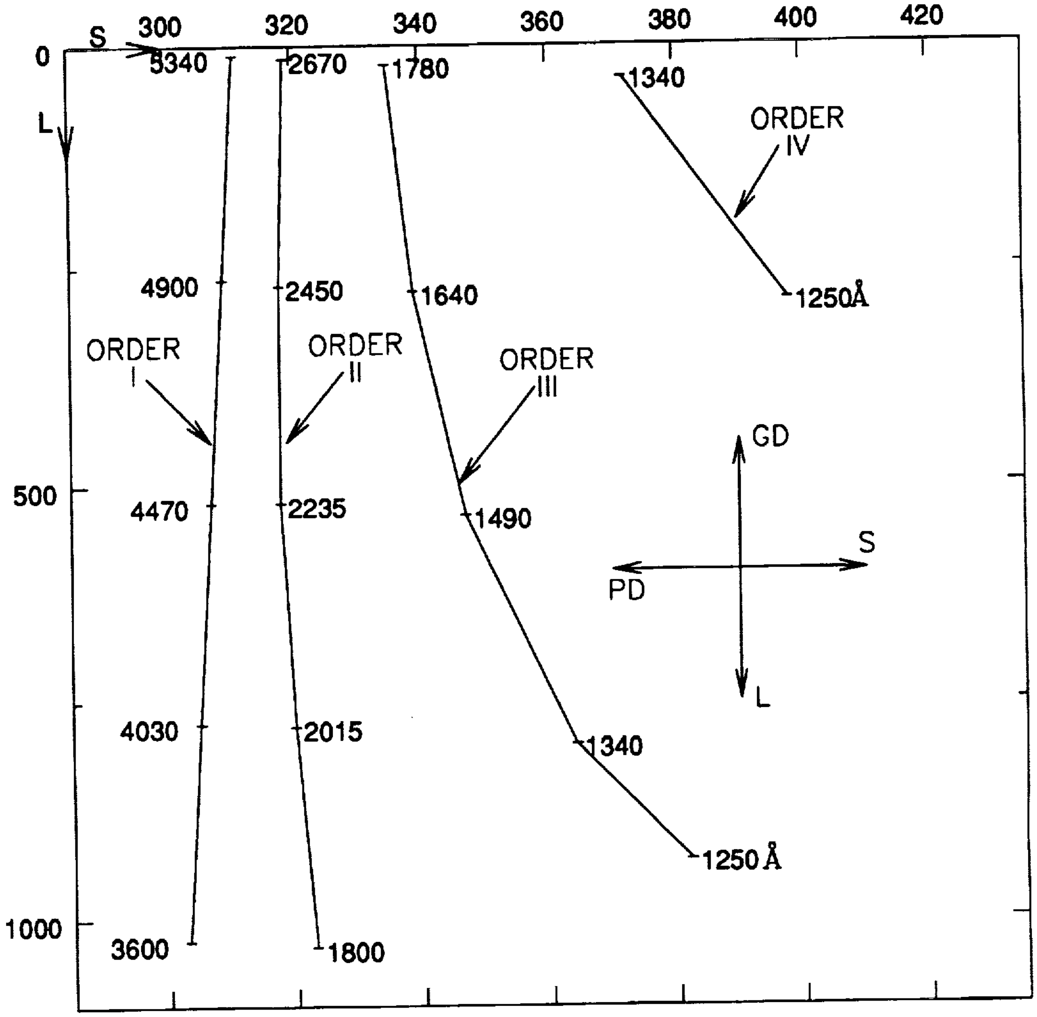

Figure 20. Optical layout of the new F/48 focal plane in the spectrograph mode and the FOPCD in the beam. The coordinates are line numbers (L) as ordinates and sample numbers (S) as abscissas. Notice the different scales for S and L.

The open area to the right of the dotted line in the extended format of the new F/48 relay in the spectrograph mode shown in Figure 9 and Figure A3 of the Appendix is normally blanked out by selecting the 256z× 1024 format with initial sample and line positions 160 and 0. It should be kept in mind, however, that dispersed light from this part of the aperture is still falling on the photocathode and, if the field here is very bright (a bright galactic nucleus, or the central part of a nebula, for example), some contamination of the right edge of the slit spectrum due to scattering should be expected. On the other hand, this area can be exploited for slitless high spatial and spectral resolution observations of compact sources. For this purpose, the user should specify the standard format 512 × 1024-CD described in Table 6. Provided the undispersed source is placed with a POS TARG special requirement near the end of the opaque spectrograph finger in the new F/48 image aperture shown in Figure 9, a full two dimensional series of quasi monochromatic images of the object will appear in this special format which has the initial sample and line positions set at 512,0. Because of the 4.6 arcseconds offset of the slit from the finger along the L direction, the wavelength range covered by the slitless mode is slightly different than that of the standard slit mode *i.e.*, ≃ 3300 to 5100Å in first, 1650 to 2550Å in second, 1150 to 1700Å in third and 1150 to 1275Å in fourth.

The slitless mode is, obviously, most advantageous when dealing with compact line emission sources that minimize the risk of overlapping monochromatic image contamination and is not recommended for extended continuum sources. One important advantage of the slitless mode for point sources is the elimination of the uncertain slit function which depends on the OTA PSF at the time of observation and the accuracy of the target acquisition procedure that places the object on the narrow spectrograph slit. A disadvantage is the rapidly decreasing sensitivity with increasing distance of the object from the slit finger due to vignetting, which can be seen in Figure A3.

4.6 DETECTORS

The transfer optics described in Section 4.1 relay the image produced on the OTA focal plane to the photocathode of a two dimensional photon counter drawn schematically in Figure 21. The detector consists of three basic parts: a three stage image intensifier tube, a coupling lens, and a TV camera tube.

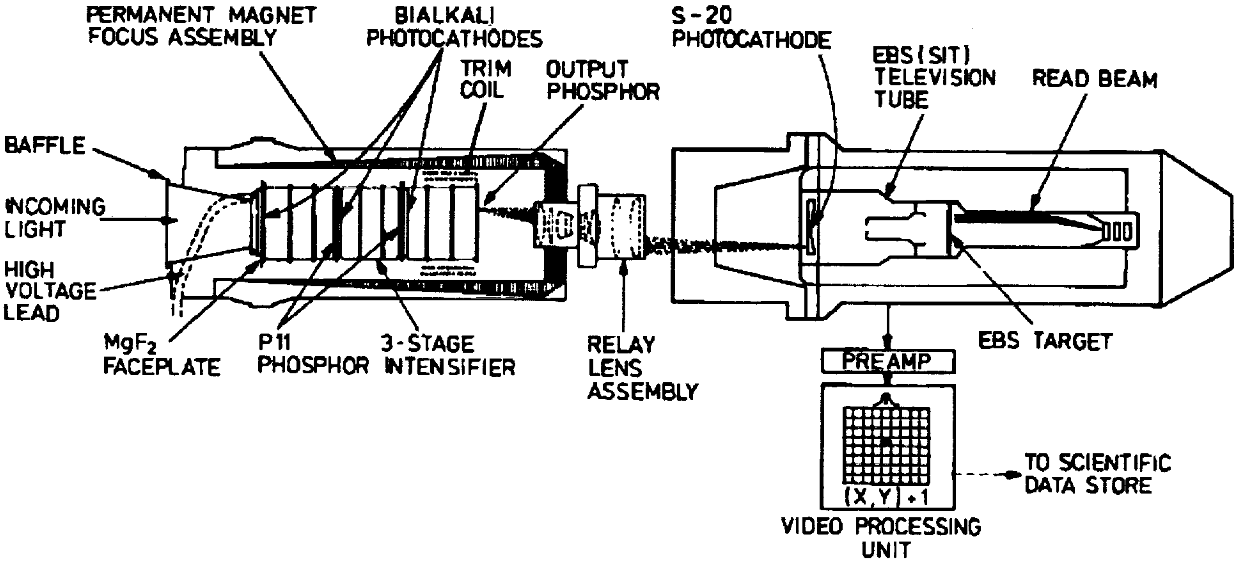

Figure 21. Physical Layout of the Imaging Photon Counting Detectors

4.6.1 Image Intensifier and Coupling Lens

The intensifier is an EMI 9614 three stage tube magnetically focused by means of a permanent magnet. The first-stage photocathode (like the following two) is a hot bialkali for the highest quantum efficiency in the UV-blue region and the lowest dark-count rate at 17°C. It has a useful diameter of 40mm and is deposited on a MgF_2 input window.

The photoelectrons generated at the first stage are accelerated by a 12 kilovolt potential and impinge on a P11 phosphor layer coupled by a 4 micron thick mica membrane to the second photocathode. This amplification process is repeated in the second and third stages to achieve an overall photon gain of 1.3 $\times 10^5$. Focusing of the intensifier electrons is accomplished with a carefully shaped permanent magnet assembly and a trimcoil is added around the third stage for fine adjustments.

The limiting spatial resolution of the intensifier is 35 line-pairs per millimeter. The dark current at an ambient temperature of 17° C is less than 10 counts cm^{-2} s^{-1} (10^{-4} counts $pixel^{-1}$ s^{-1} in the normal mode). Both of these characteristics are essentially limited by the first stage of the intensifier tube.

A lens assembly consisting of 9 components in a double Gaussian design is used to transfer the image from the output phosphor of the intensifier to the fiber-optic faceplate of the TV camera. It is designed to operate at f/2.7 with a slight magnification (1.15) to compensate for the demagnification of the image intensifier. The 80% energy width for point object images varies between 22 and 35 microns over the whole of the useful area and the light transmission is more than 60%.

4.6.2 TV Tube

The camera tube is a Westinghouse WX32719 low-light TV tube. This is a high-sensitivity, high resolution EBS tube (Santilli and Conger in *Photo-Electronic Devices*, AEEP, ed. L. Marton, 33A, 1972) with a 25 millimeters square diode array target, magnetic focus and deflection coils and an electrostatically focused image section with a 40 millimeter diameter useful photocathode area. The S-20 photocathode is evaporated onto the concave inner surface of the input fiber-optic faceplate. The emitted photoelectrons are accelerated by a potential of up to 12 kilovolts and focused onto the target which is an N-type silicon wafer with diffused P-type regions arranged in an hexagonally-packed diode array.

During operation each diode is reverse biased. Incoming photoelectrons generate electron-hole pairs which discharge the diodes. An amplified charge pattern corresponding to the image is then stored in the diodes. The charge flowing in the target lead, when the scanning beam recharges the diodes, is the signal current. The target gain is about 2500 and the modulation transfer function is 50% at 8 line-pairs per millimeter. The video signal coming from the TV tube is amplified by the preamplifier and then transmitted to the Video Processing Unit (VPU).

4.7 VIDEO PROCESSING UNIT

Each camera has its dedicated VPU which accepts the amplified signals from the camera preamplifier. The purpose of the VPU is to determine the x-y centroid of each event, determine if a true photon event has occurred and to increment the SDS memory address corresponding to the location where the photon event was detected. During any one scan of a frame of duration of 30 milliseconds for the 512 × 512 format down to 520 microseconds for the smallest 64 × 64 format there will only be a few scattered photon events. A photon event is typically a spot with a diameter of 3 or 4 pixels. It is read by the scanning beam on successive lines of the raster scan. Figure 22 illustrates how such a signal would look using the z axis to represent the magnitude of the charge.

As a line is scanned, a gaussian shaped pulse is produced. As successive lines are scanned, additional pulses, corresponding to slices of the event, increase in peak amplitude until a maximum is reached. The pulse amplitude then decreases. This video signal is amplified and presented to the VPU which takes the incoming video lines and produces two signals needed to analyze the waveform, Peak Signal and Extent Signal. The Peak Signal corresponds to the point of maximum amplitude of an event on a single scan line or slice. The Extent Signal is used to determine the time or extent of the event during a single line.

A true photon event is present on several successive lines. Analysis of these events characterized by the peak and extent signals on successive lines is the task of the VPU. By using delay lines and shift registers, each event is examined in a 4 × 9 pixel area by real time analysis so that the same event on successive lines can be analyzed. The z-dimension event center is tagged in the x and y direction. The Pattern Recognition Logic analyzes the event's shape to determine true photon events and reject other noise and ion events.

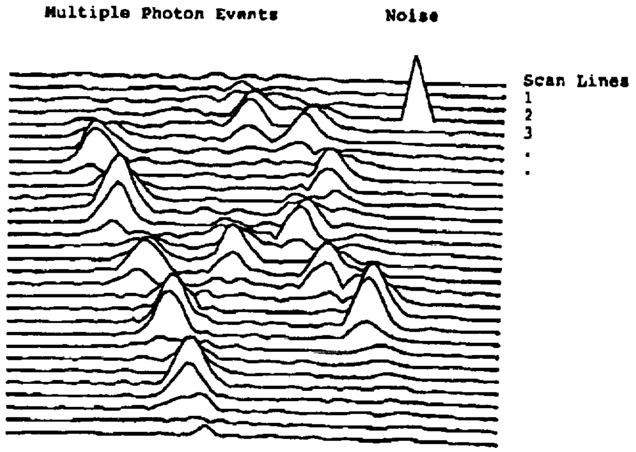

Figure 22. Schematic Drawing of a Typical Raster Scan Output of the Detectors

4.8 SCIENCE DATA STORE

As an event is detected and classified as valid, the video processing unit causes the science data store (SDS) to increment by one the memory location corresponding to the event centroid. The image is gradually built up over the exposure time. After stopping the exposure, the SDS can be read out without disturbing the stored image. The SDS can accept a 512 × 512 line image in the 16 bit word mode or a 512 × 1024 line image in the 8 bit word mode. The cycle time for the SDS is compatible with the camera scan rate of $\geq 10^6$ pixels per second. This rate is maintained for all formats and zoom. In this latter mode, the camera read beam scans the target twice as fast in the line direction as it does in the normal imaging mode but the pixels are twice as long. The detector generates an increment command for every pixel in which a photon event has been detected. A scan of 256K pixels occurs in less than 30 milliseconds while a scan of 4K pixels (*i.e.*, a 64 × 64 pixel squared format) takes place in approximately 512 microseconds.

There are two different interface circuits in the SDS (SDS-1 and SDS-2), with unit 1 dedicated to the camera of the new F/48 relay and unit 2 to the camera of the new F/96 relay. The SDS memory is physically divided into 22 modules of 16K 16-bit data words each holding 32 words from each of 512 lines, but only 16 modules are active at any given time. These 16 modules are accessed in sequence to reduce the required memory cycle time. Each SDS word has 22 bits, with the extra 6 bits being used for "single-bit" error correction and "two-bit" error detection. Included in the engineering telemetry are error detection and correction bits set for each logical module. If more than 6 SDS memory modules fail, the memory can still be operated in a reduced data mode. In this case, zeros will appear in the downlink for those modules that are not available. Data loss occurs from the "right-hand" side, so if only 15 modules are up, words 0-479 for each of the PDA lines of 512 pixels would be obtained.

The SDS can be operated in either the normal imaging mode or the SDS dump mode so it is necessary to interrupt the pixel increment commands from the detector to read out the SDS memory to the downlink. Each readout is a dump of the 256K 16-bit words of SDS memory, and hence contains 4M data bits regardless of the image format. Readout of science data is normally done under control of the NSSC-1, which controls the gating of signals to the Remote Interface Unit (RIU) of the SI C&DH including the Science Data Formatter (SDF). From the SDF, the data is fed to the downlink or the tape recorder.

5.0 OBSERVING ARRANGEMENTS

5.1 IMAGING, OCCULTATION AND SPECTROGRAPHIC MODES

Operationally, the observation of an astronomical source with the FOC is defined once the following physical parameters are specified:

1. The configuration or optical relay (the new F/96 or the new F/48 camera)
2. The positions of the filter wheels (4 for the new F/96, 2 for the new F/48 camera)
3. The spectrograph mirror position (in or out of the new F/48 beam)
4. The S×L imaging format ($S \leq 512$, $L \leq 1024$ pixels with S the number of SDS pixels in the line scan direction and L the number of SDS pixels in the increasing line direction)
5. The word length (8 or 16 bits per word)
6. The pixel size (normal 24 × 24 microns squared or zoomed 48 × 24 microns squared)
7. The position (S_0, L_0) of the starting pixel. This can be specified with a least increment corresponding to 0.25 pixel both in the S and L directions. Telemetry monitoring, however, can only verify the starting pixel with an accuracy of 32 pixels.
8. The position of the target in the chosen format.

Due to the high background count rate and high-voltage turn-on problems which have occurred in the F/48 relay (see Section 6.4), the F/48 camera will not be made available in Cycle 5, pending further testing and data analysis.

In general, selections 4, 5, and 6 have to be made consistent with the 4 Mb SDS memory size limitation. This means that the word length is completely defined, once the format is selected, as all formats larger than 512 × 512 pixels squared will automatically require an 8-bit word length while any format of that size or less will be imaged with 16-bit words.

Obviously, only a small fraction of all the possible observational modes allowed in principle by the FOC will find practical astronomical application and, therefore, be accurately and extensively understood and calibrated prior to use. Table 6 lists the main characteristics of the anticipated standard imaging and spectrographic observing modes for the new F/96 and the new F/48 relays. The first column in this table gives the format size (S×L), the second the pixel size in microns and arcseconds squared in the sky, the third the starting pixel (S_0, L_0), the fourth the word length, the fifth the zoom configuration, the sixth the overall field of view in arcseconds squared for that format, the seventh the maximum count rate per pixel N_{MAX} for that format (see Section 6.2.1), and the last column lists the main scientific justification for the selection, the mode names used in the Proposal Instructions for HST, if appropriate, and the proposal entry required for that format. S_0 is given in the 1–1024 range on a dezoomed extended format.

For the spectrographic modes of the new F/48 relay, the pixel size and the FOV are given in units of arcseconds × Angstroms in first order. The pixel size (selection 6 in the list above) is considered an optional parameter in the Phase II Exposure Logsheet of the ST Proposal Forms. The default value, if none is specified, is 24 × 24 microns squared for imaging and 48 × 24 microns squared for spectroscopy. The position and orientation of the target in the aperture (selection 8) should be specified in the Special Requirements column of the Phase II Exposure Logsheets.

Table 6a: New F/96 IMAGE or OCC Modes

Format (S × L)	Pixel Size (μm^2) ($arcsec^2$)	Offset (S_0,L_o)	Word Length	Zoom	FOV ($arcsec^2$)	N_{MAX}[a] (cs^{-1})	Comments/ Proposal Entry
512 × 1024	50 × 25 (0.028 × 0.014)	0,0	8 bit	on	14 × 14	0.04	Largest FOV. IMAGE or OCC Mode. 512 × 1024, PIXEL = 50 ×25
512 × 1024	25 × 25 (0.014 × 0.014)	256,0	“ “	off	7 × 14	0.08	Largest FOV with highest resolution IMAGE Mode. 512 × 1024
512 × 512	50 × 25 (0.028 × 0.014)	0,256	16 bit	on	14 × 7	0.08	Largest FOV with highest photometric accuracy. IMAGE mode. 512 × 512, PIXEL = 50 × 25
512 × 512	25 × 25 (0.014 × 0.014)	256,256	“ “	off	7 × 7	0.15	Highest photometric accuracy. IMAGE Mode. 512 × 512
512 × 512	“ “	0,512	“ “	“ “	“ “	“ “	Covers 0.4 coronographic finger. OCC Mode. 512 × 512-F0.3
512 × 512	“ “	421,0	“ “	“ “	“ “	“ “	Covers 0.8 coronographic finger. OCC Mode. 512 × 512-F0.5
256 × 256	“ “	384,384	“ “	“ “	3.6 × 3.6	0.6	Wider dynamic range, highest photometric accuracy. IMAGE Mode. 256 × 256
128 × 128	“ “	448,448	“ “	“ “	1.8 × 1.8	2.4	Widest dynamic range. IMAGE Mode. 128 × 128

[a] Maximum count rate to maintain <10% non-linearity for uniform illumination. Point sources may be observed at count rates in the peak of the core at about 6 times this level and still maintain <10% non-linearity (see Section 6.2.2).

Table 6b: New F/48 Image Modes[Not Available in Cycle 5]

Format (S × L)	Pixel Size (μm^2) ($arcsec^2$)	Offset (S_0,L_o)	Word Length	Zoom	FOV ($arcsec^2$)	N_{MAX} (cs^{-1})	Comments/ Proposal Entry
512 × 1024	50 × 25 (0.056 × 0.028)	0,0	8 bit	On	28 × 28	0.03	Largest FOV. 512 × 1024, PIXEL = 50 × 25
512 × 1024	25 × 25 (0.028 × 0.028)	0,0	" "	Off	14 × 28	0.05	Largest FOV with highest resolution. 512 × 1024
512 × 512	50 × 25 (0.056 × 0.028)	0,384	16 bit	On	28 × 14	0.06	Largest FOV with highest photometric accuracy, 512 × 512, PIXEL = 50 × 25
512 × 512	25 × 25 (0.028 × 0.028)	0,384	16 bit	" "	14 × 14	0.10	Highest photometric accuracy. 512 × 512
256 × 256	" "	0,512	" "	" "	7 × 7	0.4	Wider dynamic range. 256 × 256
128 × 128	" "	0,576	" "	" "	3.6 × 3.6	2.4	Widest dynamic range. 128 × 128. This format exhibits reduced sensitivity.

Table 6c: New F/48 SPEC Modes [Not Available in Cycle 5]

Format (S × L)	Pixel Size (μm^2) (arcsec × Å)	Offset (S_0,L_o)	Word Length	Zoom	FOV (arcsec × Å)	N_{MAX} (cs^{-1})	Comments/ Proposal Entry
512 × 1024	50 × 25 (0.056 × 1.8)	0,0	8 bit	On	28 × 1800	0.04	Widest field for main aperture correction. 512 × 1024-SLIT
512 × 1024	25 × 25 (0.028 × 1.8)	192,0	" "	Off	14 × 1800	0.08	Highest spatial and spectral resolution with widest spectral range. 512 × 1024, PIXEL = 25 × 25
" "	" "	512,0	" "	" "	" "	" "	Slitless spectrograph format. 512 × 1024-CD, PIXEL = 25 × 25
256 × 1024	50 × 25 (0.056 × 1.8)	192,0	" "	On	14 × 1800	0.03	Widest dynamic and spectral range. 256 × 1024-SLIT
256 × 1024	25 × 25 (0.028 × 1.8)	320,0	" "	Off	7 × 1800	0.10	Widest dynamic range and highest spatial resolution. 256 × 1024-SLIT, PIXEL = 25 × 25

5.2 TARGET ACQUISITION MODES

Two acquisition modes are available for use with the FOC as described in the Proposal Instructions: INTeractive ACQuisition (Mode I) and blind pointing (Mode III). On-Board Acquisition (Mode II) is not available any longer due to technical limitations. In addition, an EARLY ACQuisition can be specified where an examination of the field is necessary prior to science exposures to help measure a target in a crowded field or to determine a slit alignment angle, for example.

5.2.1 Mode I Target Acquisition - INTeractive ACQuisition

Designed to be the most accurate acquisition procedure for use with the coronographic fingers, the slit or small image formats, this procedure requires the involvement of the observer, in real-time, to identify the field and measure the center of the target on an FOC image. First, using a blind pointing acquisition, the target is placed in a standard field of view and an image is taken, with instrument parameters such as filters and exposure time selected by the user. The resulting image of the field is then read down for immediate display in the Observation Support System (OSS) area at ST ScI. Once the observer identifies the target using an interactive image display system and measures the target position from the display screen, a slew request is generated and up-linked, and the telescope is maneuvered to place the target in the selected destination. There is no verification of the subsequent field unless specifically requested by the observer on the exposure logsheets.

INTeractive ACQuisition is expected to be the standard acquisition procedure for OCC mode. For the long slit spectrograph, which has a slit width of only 0.06 arcseconds, INTeractive ACQuisition is the only safe way to ensure proper centering of a point source. The procedure also may be useful in IMAGE mode when an object needs to be placed in a particular place in one of the imaging apertures or when using very small fields of view.

In IMAGE mode, objects of 9th magnitude or brighter require a more accurate INTeractive ACQuisition strategy to ensure the safety of the detector. The following steps will be automatically scheduled whenever an acquisition is required of a target brighter than 9th magnitude:

- Step 1 will be the first acquisition exposure taken with sufficient neutral density and color filters to ensure the FOC is operating in a safe regime. The spacecraft will be pointing at a blank field 30" away from the bright target. It is the responsibility of the observer to include this pointing offset in the target coordinates, and to coordinate this with the Instrument Scientist. The image is downlinked to OSS where the Instrument Scientist will check that the proper filter configuration is in place and will agree on the small angle maneuver to bring the bright target into the FOC field. In an attempt to reduce the overhead times, this first exposure will be a DARK, and will be executed during Earth occultation. If and only if the proper filter configuration is in place, the spacecraft will be commanded to slew to the bright target. The exposure time for the first image is selected by the user.
- If the filters are properly placed, Step 2 will be the scientific exposure, with the same filter configuration and format used for the acquisition. If the telemetry indicates that the correct filters are not in place, no maneuver will be executed, and the observation will continue on the blank field.

In general, the interactive nature of this acquisition, requiring TDRSS links, means that the procedure is classed as a "limited resource" in the Proposal Instructions. Furthermore, our initial testing of the acquisition procedure suggests that it is extremely time consuming for the user, and therefore must be used only when strictly required. The current estimates of the overhead times give 1 orbit for each Bright Object Acquisition. The procedure must be repeated whenever a different filter configuration is selected. We are currently working on an alternative Bright Object Acquisition procedure which will be fully automatic and will execute in a much shorter time. Please contact the Instrument Scientist for further details.

5.2.2 Mode III Target Acquisition - Blind Pointing

Mode III is the default acquisition procedure for the FOC. When no target acquisition is specified in the Special Requirements section on the proposal exposure logsheets, the telescope performs a straight-forward blind pointing on the coordinates provided by the user. After the acquisition, no explicit verification of the target position in the fields of view aperture is performed. No overhead time in addition to the guide stars lock time is charged to the user for this acquisition.

Mode III is expected to be the standard acquisition procedure for IMAGE mode in all instrument configurations, except for those formats with fields of view of less than 3 arcseconds square, providing the target has a coordinate position measured with the Guide star selection system Astrometric Support Package (GASP) ensuring best accuracy with respect to the guide star astrometric catalogue. The procedure will not be useful for point sources in either OCC or SPEC modes, because blind pointing is unlikely to provide the precision needed to accurately place a target on the slit of the new F/48 relay (width = 0.06 arcseconds) or on one of the coronographic fingers. However, for extended objects where accurate pointing is not important, blind pointing can be used. Again, targets of magnitude 9 and brighter cannot be acquired on the fingers using blind pointing. In this case, see Mode I.

5.2.3 EARLY ACQuisition

When necessary, it is possible to take an acquisition image some time before the scientific observation. The acquisition image can be used for a better identification of the field, or a better evaluation of the source flux, etc. In order to update the observation parameters, a minimum turnaround time of two months is necessary between the acquisition and the science exposure.

Presently, the system does not have the capability to select for the science observation the same pair of guide stars successfully used for the acquisition exposure, thus eliminating the possibility of using the acquisition image to measure the target coordinates at the accuracy level required to perform, for example, a blind pointing on the new F/48 0.06 arcseconds slit.

Table 7: Target Acquisition Formats

Relay	Format Name	Size	USE
	Mode I Target Acquisition and Early Acquisition		
F/48	512z × 512	1024 × 512	spectrograph slit[a]
F/48	512 × 512	512 × 512	spectrograph slit[a]
F/96	512 × 512	512 × 512	
F/96	512z × 1024	1024 × 1024	
F/96	512 × 512-A0.3	512 × 512	0.3" finger
F/96	256 × 256-A0.3	256 × 256	0.3" finger
F/96	512 × 512-A0.5	512 × 512	0.5" finger
F/96	256 × 256-A0.5	256 × 256	0.5" finger

a. NOT AVAILABLE in CYCLE 5.

5.3 THE FOC TARGET ACQUISITION APERTURES

For convenience, a number of special formats to be used in the Mode I acquisition exposures have been defined. These formats (listed in Table 7) have offsets that have been chosen in order to optimize the small angle maneuvers necessary to move the targets to the required locations. Their positions have been calibrated during SV and are being monitored for stability and electronic distortions to ensure good pointing accuracy.

For example, in addition to the usual centered formats, a number of acquisition formats have been defined which are conveniently located close to the 0.3 arcseconds and 0.5 arcseconds fingers of the new F/96 relay. Different sizes are available for each of these combinations, but it is strongly recommended to use the larger images due to the initial position error of the target's coordinates with respect to the Guide Stars ($\simeq 0.33$ arcseconds). For the acquisition to the spectrographic slit of the new F/48 relay, the 512 × 512 format is recommended.

6.0 INSTRUMENT PERFORMANCE

6.1 THE POINT SPREAD FUNCTION (PSF)

Before COSTAR, the HST PSF suffered from severe spherical aberration, which meant that a circular aperture of 0.1 arcsecond radius contained only 15–18% of the light from a star instead of the expected 70%. The principal effect of the spherical aberration was a loss in sensitivity, because most of the light in the halo of a faint star is effectively lost in the background noise. COSTAR has restored much of the OTA capability, in that the COSTAR-corrected PSF contains more than 75% of the light within a radius of 0.1 arcsecond at visible wavelengths while only losing less than 20% of the light to the two reflections at the two extra mirror surfaces. The net increase in sensitivity is a factor of approximately 3—4 at visible wavelengths. The correction COSTAR made to the PSF is illustrated in Figure 23, which shows the radial profile of a aberrated image and a COSTAR-corrected image.

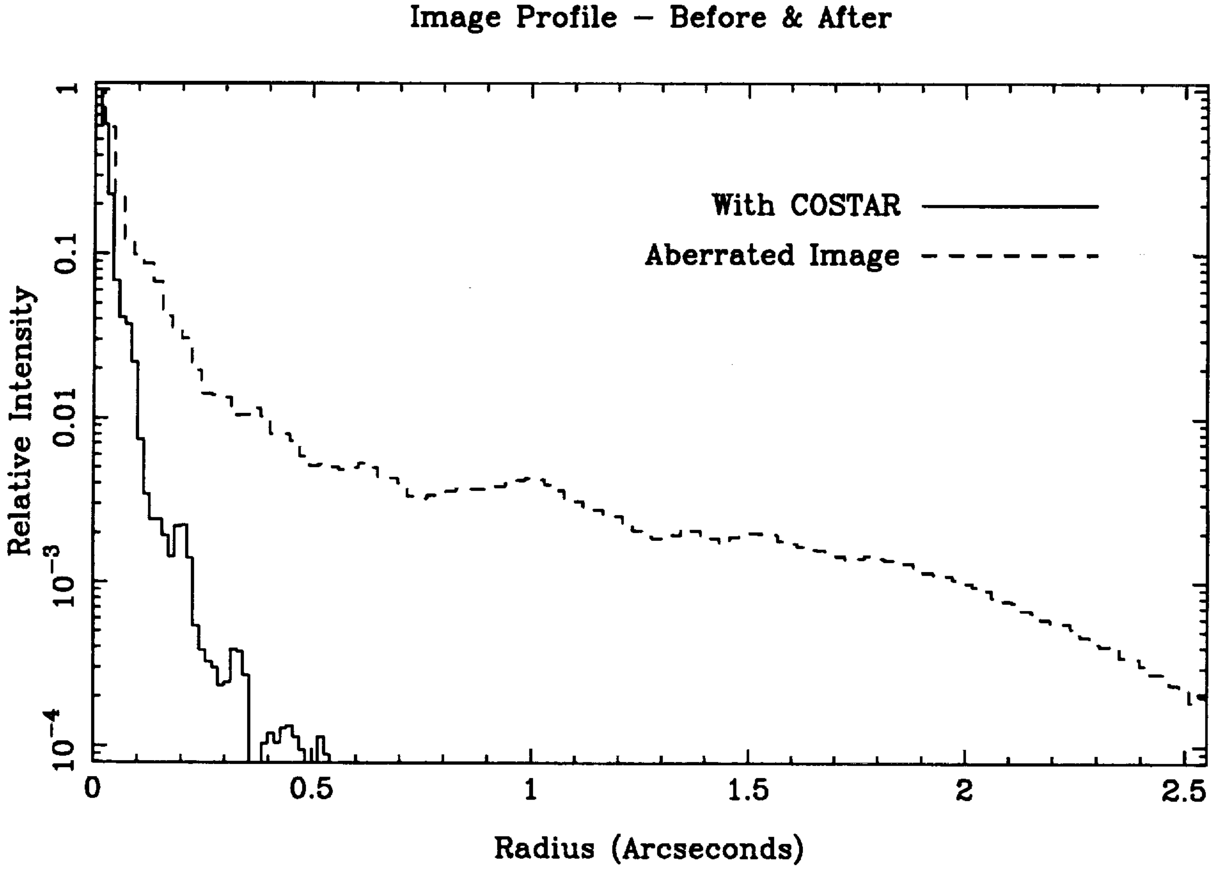

Figure 23. Radial profiles of pre-COSTAR aberrated PSF (**dotted**) and COSTAR-corrected PSF (**solid** at Hβ).

Table 8: Measured Energy Fraction ε(λ) for the New F/96 Relay

	r	Filter								
n	(arcseconds)	F120M	F140M	F170M	F210M	F278M	F346M	F410M	F486N	F550M
1	0.000	0.039	0.061	0.055	0.094	0.093	0.087	0.071	0.064	0.054
9	0.024	0.214	0.294	0.319	0.415	0.452	0.409	0.385	0.380	0.345
21	0.037	0.315	0.421	0.463	0.555	0.621	0.528	0.543	0.548	0.532
37	0.049	0.393	0.499	0.558	0.626	0.712	0.601	0.627	0.613	0.611
69	0.067	0.491	0.577	0.652	0.688	0.774	0.722	0.744	0.697	0.670
97	0.080	0.536	0.619	0.696	0.722	0.802	0.773	0.799	0.769	0.727
137	0.095	0.578	0.657	0.739	0.768	0.832	0.809	0.830	0.831	0.807
177	0.108	0.599	0.682	0.763	0.798	0.858	0.833	0.844	0.855	0.851
225	0.121	0.626	0.703	0.781	0.821	0.886	0.856	0.858	0.870	0.870
293	0.139	0.653	0.724	0.798	0.841	0.909	0.877	0.877	0.886	0.881
349	0.151	0.664	0.736	0.808	0.851	0.919	0.896	0.888	0.897	0.888
421	0.166	0.682	0.749	0.819	0.859	0.928	0.916	0.905	0.909	0.898
489	0.179	0.696	0.762	0.829	0.867	0.934	0.927	0.922	0.917	0.906
577	0.194	0.712	0.777	0.841	0.873	0.942	0.938	0.934	0.928	0.915
665	0.209	0.723	0.790	0.850	0.877	0.948	0.944	0.941	0.941	0.921
749	0.222	0.734	0.799	0.855	0.883	0.951	0.948	0.945	0.950	0.929
861	0.238	0.747	0.810	0.863	0.889	0.954	0.952	0.950	0.955	0.942
973	0.253	0.750	0.821	0.871	0.896	0.958	0.956	0.953	0.958	0.949
1085	0.260	0.765	0.830	0.879	0.902	0.961	0.958	0.957	0.961	0.952
1201	0.281	0.774	0.839	0.886	0.909	0.964	0.959	0.961	0.964	0.955
1313	0.293	0.790	0.847	0.892	0.913	0.967	0.961	0.964	0.966	0.958
1457	0.309	0.803	0.856	0.900	0.917	0.970	0.964	0.967	0.969	0.961
1597	0.324	0.813	0.865	0.907	0.923	0.972	0.966	0.970	0.972	0.963
1741	0.338	0.822	0.875	0.914	0.929	0.974	0.968	0.973	0.975	0.964

In Table 8, the encircled energy fraction $\epsilon\ (\lambda\ )$ is tabulated for various circular apertures against the number of pixels in the aperture and the effective radius (defined as $\sqrt{\#pixels/\pi}$), with the definition that the encircled energy is 1.0 at a radius of 1 arcsecond (70 pixels). A more thorough discussion of the definition of the encircled energy calculation and the rationale behind it is given in the Detective Quantum Efficiency section, 6.3. The improvement in performance over the aberrated PSF is shown in Figure 24, where the encircled energy curve is compared to that of the aberrated OTA and with a perfect diffraction-limited image from a 2.4m circular aperture with a 0.33 central obstruction. It can be seen that the COSTAR-corrected FOC PSF approaches that of an ideal imaging system in both encircled energy performance and in the FWHM of the PSF core.

Despite the outstanding performance of the OTA+COSTAR+FOC imaging system in terms of encircled energy within small radii, the PSF appearance does not match a true diffraction-limited simulation perfectly at all wavelengths. All of the COSTAR alignment was done using the F486N filter, and it can be seen that the first diffraction ring shows a non-uniform azimuthal intensity distribution (Figure 25a). There is also some residual coma that varies with time, possibly due to some slack in the M1 tilt mechanism.

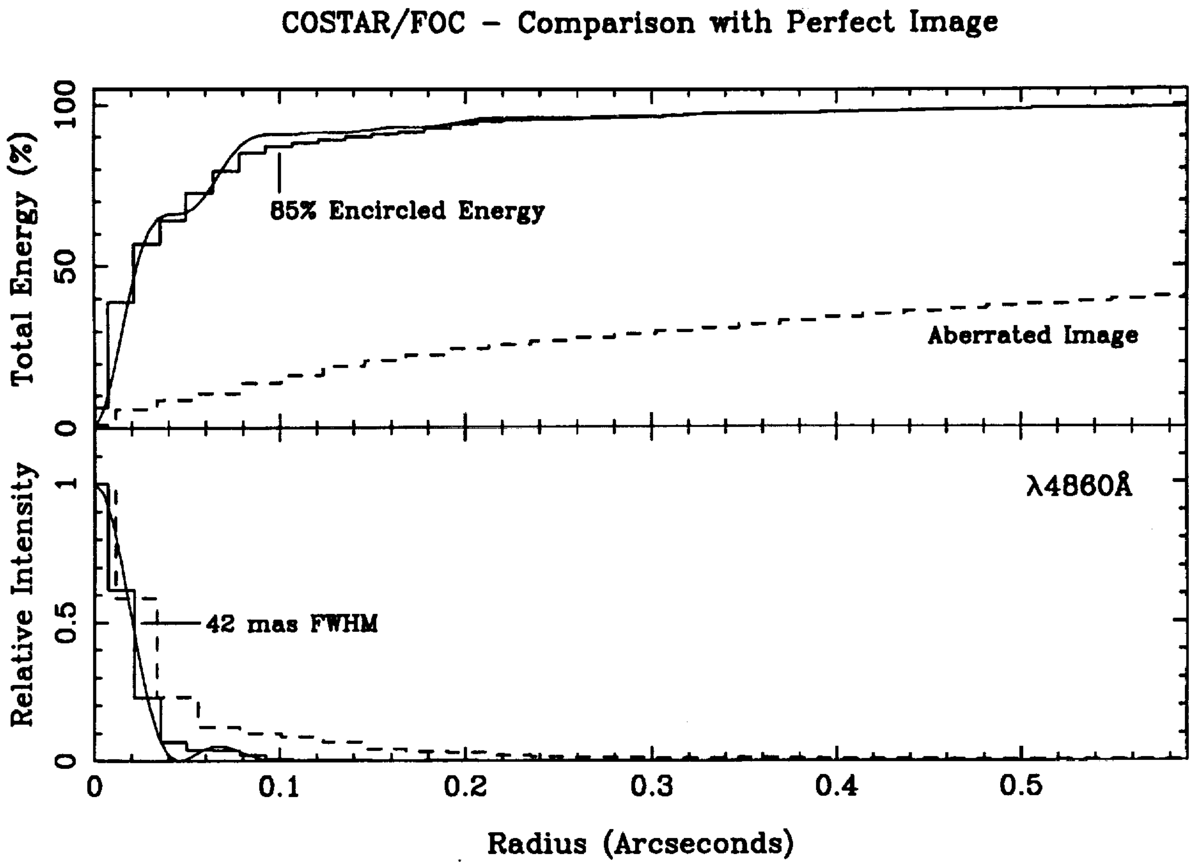

Figure 24. The encircled energy fraction and PSF profile for the COSTAR-corrected F/96 and pre-COSTAR F/96 relays compared to those expected from a perfect diffraction limited OTA.

In the ultraviolet, the PSF shows a fairly strong jet-like feature pointing approximately in the -V3 direction (Figure 25b). The strength decreases with increasing wavelength but is still quite noticeable at 4000Å. The cause of this feature and the asymmetry in the first diffraction ring is unknown.

Three filters have been found to have artifacts. The F372M filter shows a strong linear feature in the PSF wings, at approximately 45° to the OTA spider (Figure 25c). The F501N and F502M filters both show a faint ghost image approximately 60 and 24 pixels respectively from the PSF center.

A selection of PSF images is available on STEIS, the STScI archives. STEIS contains proposal information, exposure catalogs, and STSDAS software releases (including the instrument filter and DQE tables) and is accessible via anonymous FTP, gopher, or WWW's Mosaic interface at *stsci.edu*.

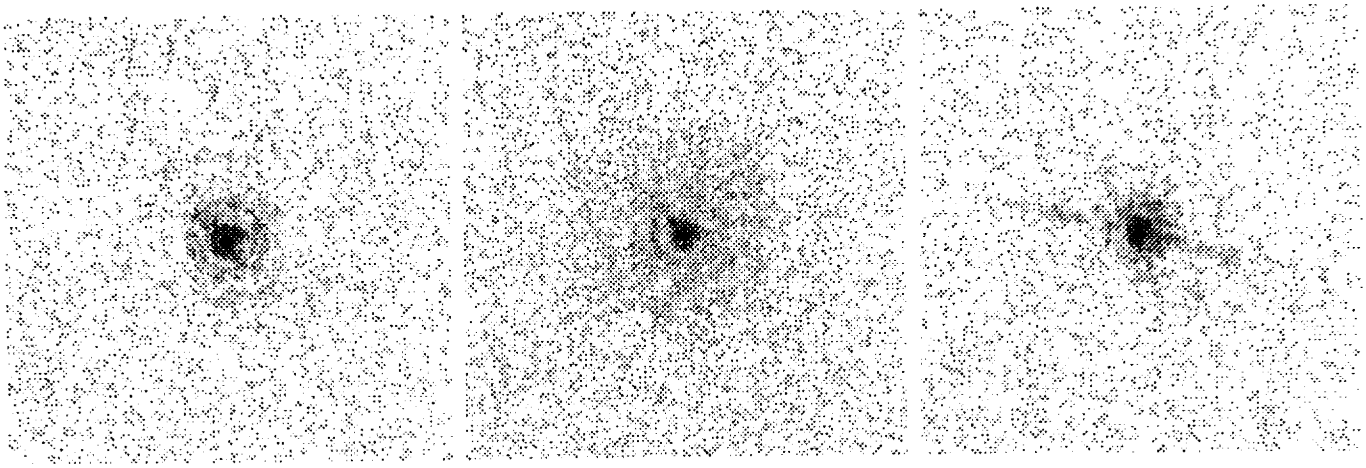
a. b. c.

Figure 25. Images of PSFs taken with the COSTAR-corrected F/96 camera. **a.** F486N filter **b.** F120M filter **c.** F372M filter.

6.1.1 Image quality and Field Dependence of the PSF

The FOC was designed to image the HST focal plane in an off-axis position, 6.56 arcminutes from the optical axis. At this distance, the focal plane is tilted with respect to the V1 axis by 10°. It is this plane that the FOC cameras image onto their photocathodes. However, the focal surface produced by COSTAR is tilted with respect to the plane that the FOC images. This results in a field-dependent focus variation of approximately 0.7mm over the full field of the new F/96 relay. Similarly, the tangential and sagittal focal surfaces are tilted with respect to each other, and this introduces field-dependent astigmatism. Both of these effects increase linearly with distance from the fully-corrected field point.

The field-dependence of the PSF was investigated during SMOV, but the limited observations do not allow detailed characterization of the performance as a function of field position. It is clear from calibration observations that the PSF is visibly different away from the central field point across the largest formats. However, this does not affect the encircled energy within 0.1 arcsec radius by more than a few percent for any field position within the 512X512 aperture. A more thorough evaluation of the field dependence of the PSF will follow in a future Instrument Science Report.

6.2 DYNAMIC RANGE

If two or more photon events overlap during a given frame, the VPU detection logic will only count one detected photon. This 'undercounting', or non-linearity, sets a hard limit on the maximum allowable photon rate for the FOC. This limit depends on the frame scan time, which is proportional to the area in pixels of the selected format. Users can improve the linearity performance by choosing a smaller imaging format (but at the cost of field of view).

The linearity performance also depends on the image structure. If the illumination is nearly uniform, then the non-linearity depends on the frame scan time and the photon event size (typically 3 × 3 pixels). However, if the illumination comes from a perfect point source, then the photon event size does not matter, since there are no neighboring photon events, only those that arrive in the illuminated pixel. For FOC images, no source is truly pointlike, but the linearity characteristics of astronomical point sources and flat fields are sufficiently different that they are discussed separately. The situation for more complex image structure (i.e. just resolved or linear) will of course be intermediate between these two limiting cases.

6.2.1 Uniform Illumination

Here 'uniform illumination' refers to the case where the intensity varies by less than 20% over scales of 20 pixels. The frame scan time is given by

$$T_f = \frac{z(S \times L)}{8.8 \cdot 10^6} \mathrm{sec}$$

where $z = 1$ for normal and $z = 2$ for zoomed pixels. For the most widely-used format (512 × 512, normal pixels), this comes to 30 milliseconds. If, during a frame, more than half of the format area is occupied by photon events, a further event will overlap one or more existing events and will not be counted as a detected photon. This would predict a maximum count rate for the 512 × 512 format of 0.05 counts/pixel in 30 milliseconds, or about 1.7 counts/sec/pixel. In practice the saturation level is reached at a lower level, because most of the overlapping events are much larger than a single photon event and are classified as ion events and rejected.

The flatfield nonlinearity was measured on-orbit during OV and SV using observations of the internal LED calibration lamps. It was found that the intensity of the light from these lamps is directly proportional to the commanded intensity level. The linearity curve was measured for several different formats to verify the format dependence of the saturation, and the dependence on zoom mode was also investigated. A plot of the measured linearity relation for the 512 × 512 formats of the pre-COSTAR F/96 and pre-COSTAR F/48 detectors is shown in Figures 26*a* and 26*b*, respectively. Superposed is a curve that describes the behavior of the linearity relation for intensity values up to approximately 80% of the saturation value, originally suggested by Jenkins (*M.N.R.A.S.*, 226, 341 (1987)):

$$r = a(1 - exp(\frac{-\rho}{a}))$$

where r is the measured count rate, ρ is the 'true' count rate and a is a fitting parameter that is identified as the asymptotic measured count rate.

When the FOC is configured for zoomed pixels, the linearity performance is slightly different from what would be expected from scaling the results for normal pixels by the ratio of frame scan times. This is because the event sizes and the VPU detector logic are different for zoomed pixels. However, once the linearity performance of one format is calibrated for each camera in zoom mode, the performance at other formats in zoom mode can be derived by scaling by the ratio of format areas, as is the case for normal pixels. The validity of the scaling assumption for both normal and zoomed pixels was checked and found to be true.

Table 9: Calculated Flat-Field Linearity Parameters

Camera	Format (FxL)	Linearity Parameter *a*	N_{MAX} (cs^{-1})
F/96	512zx1024	0.11	0.04
	512x1024	0.37	0.08
	512x512	0.73	0.15
	256x256	2.93	0.60
	128x128	11.7	2.40
F/48	512zx1024	0.065	0.03
	512x1024	0.26	0.05
	512x512	0.52	0.06
	256x256	2.09	0.40
	128x128	8.37	2.40
F/48 SPEC	256zx1024	0.13	0.03
	256x1024	0.52	0.10

Values of a for the most commonly-used formats are given in Table 9. The values refer to dezoomed data in the case of formats that were originally zoomed. In practice, the value of a depends somewhat on position in the image, since it is effectively a measure of the photon event size, and this varies over the format due to slight focus quality variations. To ensure that non-linearity does not compromise the science data, users are advised to ensure that the count rate is kept below N_{MAX}, which is the count rate that would give 10% nonlinearity, as given in the third column of Table 9. Correct and quantifiable operation of the FOC at count rates exceeding N_{MAX} cannot be guaranteed.

6.2.2 Non-Uniform Illumination

When the illumination comes from a star, the FOC is able to count at a much higher rate before saturation occurs. This is because photon events centered on pixels close to the central pixel of a star are much less probable than in the flatfield case. However, because it is difficult and time-consuming to obtain stellar images at a large number of intensity levels, it was not possible to calibrate the point-source non-linearity relation for the pre-COSTAR PSF to the same accuracy as could be achieved in the flatfield case. The dependence of the core structure of the PSF on such factors as secondary mirror position, jitter and wavelength also made such an investigation impractical.

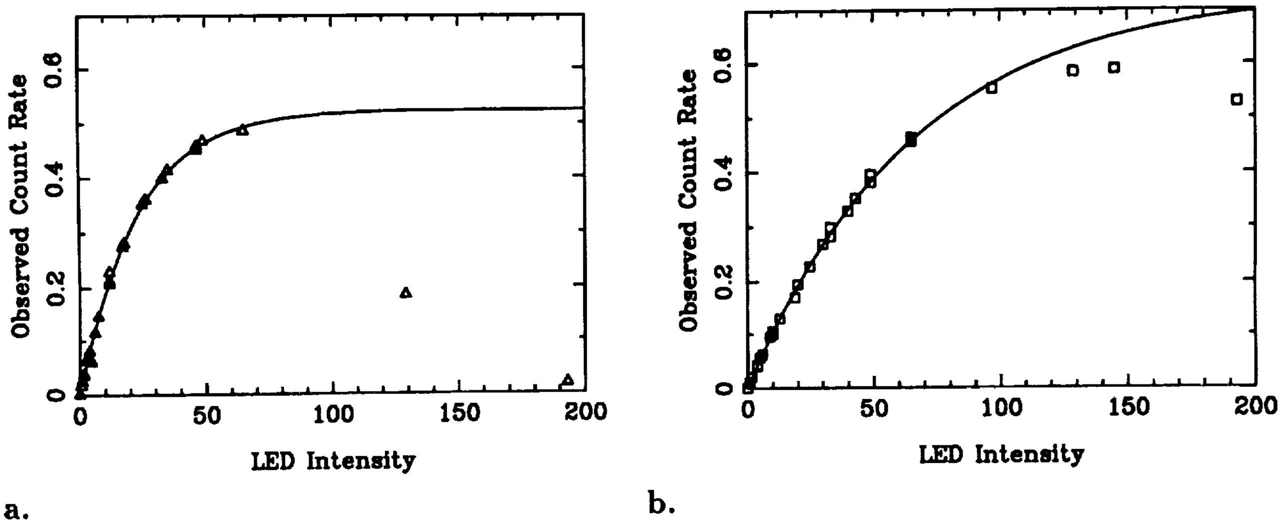

Figure 26. Flat-field linearity plots for the detectors in the pre-COSTAR F/48 and pre-COSTAR F/96 relays, **a** and **b** respectively, based on 512 × 512 pixel flat-field images of the internal LEDs at different intensities. The solid line in each plot is the best-fit solution for the linearity function given in the text.

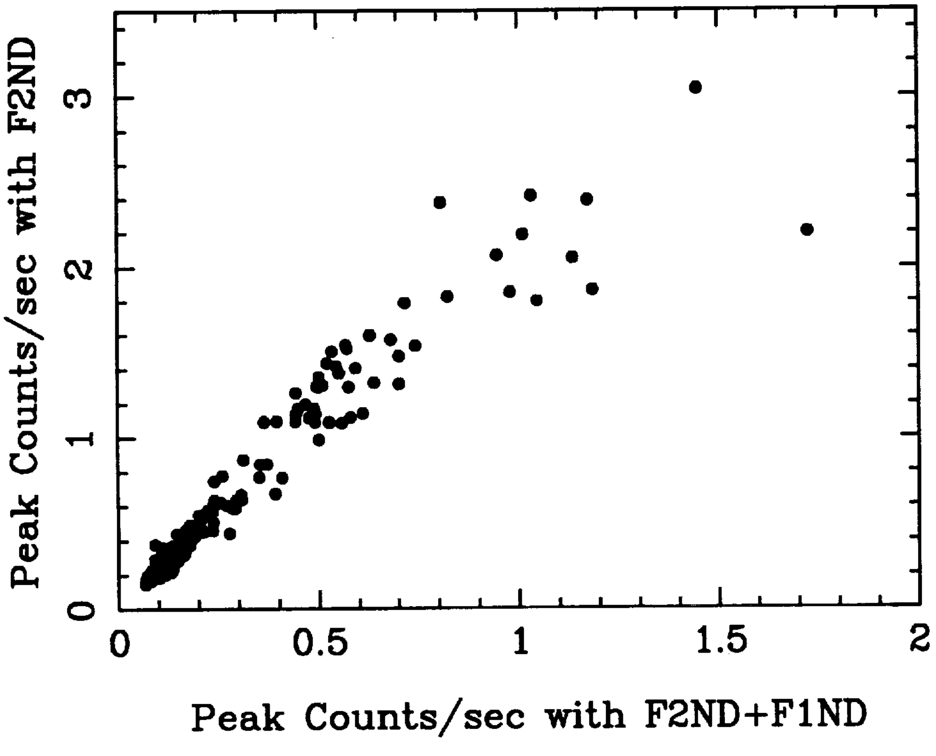

Figure 27. Linearity relation for point sources based on 512 × 512 pixel images taken with the pre-COSTAR F/96 relay through the F342W filter.

During OV and SV it became clear that for the FOC pre-COSTAR F/96 camera when used in the 512 × 512 format, the maximum obtainable count rate in the core of a star was approximately 3 counts/second/pixel. Variations on this level occur because of jitter, focus, etc. At count levels higher than this, the core of the star turns into a dark 'hole', and a bright crescent appears to one side of the core. Comparison of PSF's taken with and without neutral density filters indicate that there is no noticeable deviation from linear behavior for core count rates up to 1 count/sec in the brightest pixel. This produces the simple guideline for observers: **keep the count rate in the central pixel below 1 count/sec**, and then any photometry method chosen will give results that are not biased by non-linearity effects. If the central count rate is above 1 count/sec, one will need to use other methods to determine the brightness of the star (such as measuring the intensity in the bright halo). Table 8 give

An example of the non-linearity relation for point sources is shown in Figure 27. This is a plot of the brightest pixel intensity for stars in two FOC pre-COSTAR F/96 512 × 512 images of the center of the globular cluster M15. One image was taken with F342W+F2ND filters, while the other was taken with F342W+F2ND+F1ND filter. Apart from the large scatter, which is understood, one can see that there is no measurable deviation from a linear relation for central count rates up to 1.8 counts/sec. Clearly, any photometry method that includes the brightness of pixels other than the brightest pixel will be even less susceptible to non-linearity effects.

To put some hard numbers around these figures, note that a 20th magnitude A0V star will give a total count rate with the F342W filter of 10.9 counts/sec. Referring to Table 8, one can see that for the new F/96 relay, the central pixel contains 8.7% of the total light, therefore the expected count rate for this star is 0.95 counts/sec in the central pixel, which is at the FOC linearity limit. To observe stars brighter than 20th magnitude, it is necessary to either use a smaller format, neutral density filters or a narrower filter (e.g. F346M).

6.3 ABSOLUTE QUANTUM EFFICIENCY

Spectrophotometric standard stars were observed during SMOV and Cycle 4 Calibration using a variety of filters to allow measurement of both the PSF characteristics and the detector quantum efficiency. These measurements were made after the COSTAR mirror tilts and DOB focus were set to optimize the imaging performance at 4860 Åwavelength for the new F/96 camera. To date, no attempt has been made to characterize the new F/48 camera, so this section refers to the new F/96 camera only.

The encircled energy and detector quantum efficiency are somewhat coupled since the PSF does not have a well-defined edge; instead the flux drops steadily with distance from the star center until it gets lost in the background noise. The flux in the wings is due to scattering by dust and small imperfections in the OTA+COSTAR+FOC optical train, and is more pronounced at shorter wavelengths. When constructing an encircled energy curve, which is the curve of the fraction of light enclosed within a circular aperture of a given radius as a function of radius, one naturally has to define how one measures the total flux. In the past, this was done by choosing an aperture size that was large enough to include the spherically aberrated PSF, or about 3.5 arcseconds radius. This aperture size could comfortably fit inside the workhorse 512X512 imaging format before COSTAR was installed.

Table 10: Overall (OTA+FOC+COSTAR) Absolute Quantum Efficiency Q(λ) in 10^{-3} counts photon^{-1}

λ(Å)	Q(F/48)	Q(F/96)	Q(SPI)	Q(SPII)	Q(SPIII)	Q(SPIV)
1150	2.66	0.78				0.23
1160	6.59	1.61				0.37
1170	9.89	2.67				0.46
1180	13.17	3.92				0.55
1190	15.15	5.34				0.71
1200	16.47	6.79			0.54	0.81
1250	23.02	10.53			0.73	1.10
1300	26.18	12.64			0.81	1.25
1400	25.56	14.30			1.02	1.46
1500	25.35	15.58			1.22	
1600	23.82	14.94			1.33	
1700	22.10	14.24			1.56	
1800	21.00	13.56		2.37	1.80	
1900	24.26	15.19		3.12		
2000	31.68	19.52		3.85		
2200	47.74	30.33		5.34		
2400	59.98	41.04		6.18		
2600	62.70	49.89		6.44		
2800	64.68	59.53		6.35		
3000	65.36	70.32				
3400	66.17	78.47	12.16			
3800	60.02	78.61	12.34			
4000	55.12	71.40	12.27			
4500	41.15	44.91	11.88			
5000	24.66	25.64	9.80			
5500	10.39	12.65	5.62			
6000	4.57	5.70				
6500	0.43	0.53				

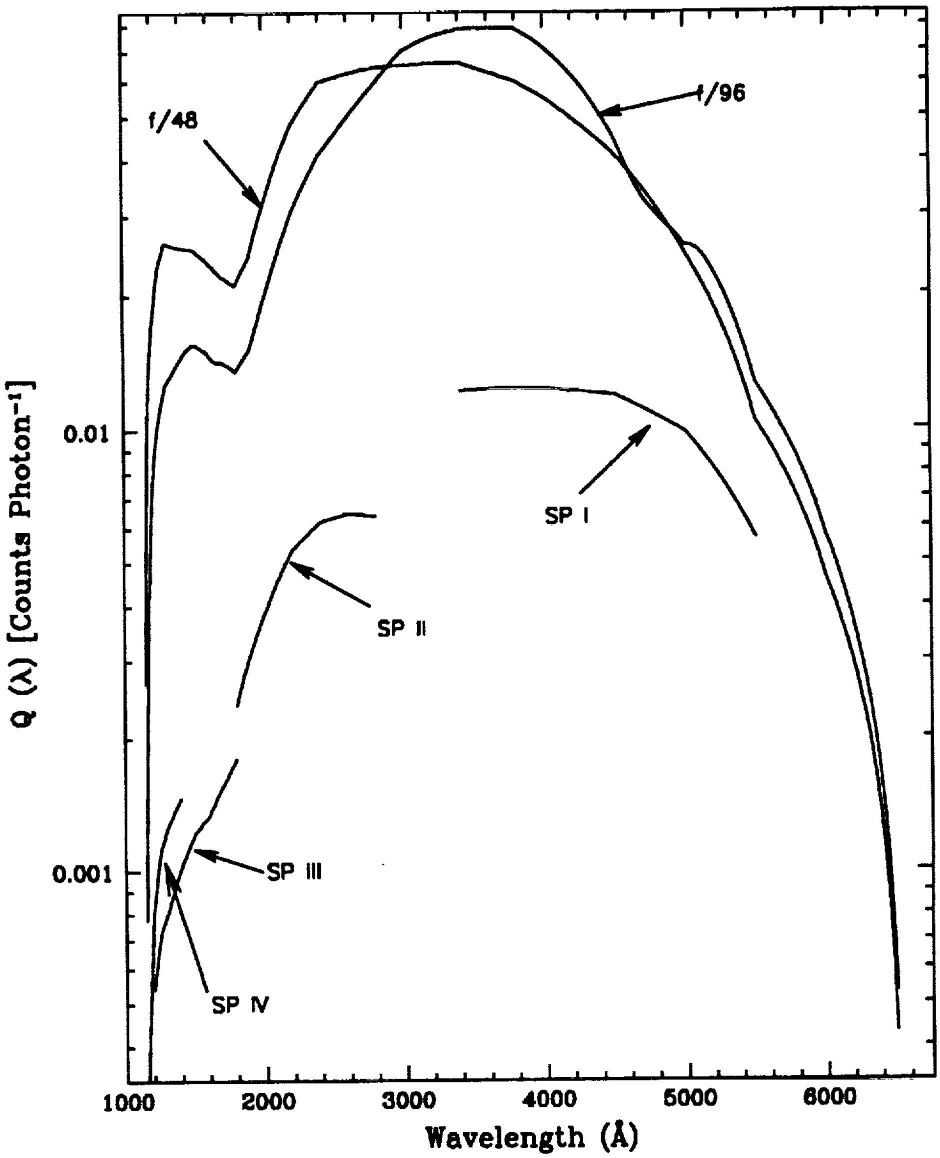

Figure 28. Baseline overall (OTA + COSTAR + FOC) absolute quantum efficiency in counts photon^{-1} as a function of wavelength for the three imaging modes and the four long slit spectrograph orders.

With COSTAR, the magnified plate scale means that such a large aperture size cannot be used for DQE measurements, particularly since most of the measurements of spectrophotometric standards were made using the 256X256 imaging format to improve the linearity performance. For this reason, it was decided to define the encircled energy to be 1.0 at a radius of 1.0 arcsecond (70 pixels) and to define the background as that value which minimizes the scatter of the points in the encircled energy curve with 0.8" $<$ r $<$ 1.0". In practice, this is equivalent to setting the background to the value measured at approximately 0.9" radius, and it does give encircled energy curves that are qualitatively in agreement with what such a curve would look like: the encircled energy asymptotically approaches a constant value at the last measured points. Users should be aware that there *is* some flux outside 1 arcsecond radius, especially in the ultraviolet, but this flux is not considered "useful" and its contribution to the total DQE is not included. The net result of using this approach is that the DQE appears to be lower than the values presented in the previous version of the FOC Handbook, particularly at ultraviolet wavelengths. There are three reasons for this. Firstly, a larger fraction of flux is scattered into the region between 1.0" $< r <$ 3.5" and is not counted towards the absolute sensitivity. This amounts to approximately 6% of the total flux for the F140M filter. Secondly, when the background is determined at a radius of 0.9 arcseconds, one is effectively subtracting more background than would make the encircled energy curve flatten asymptotically at larger radii. This effect amounts to about 7% of the total flux for this filter. Lastly, the COSTAR reflectivities that had been used to predict the DQE in the previous version of the Handbook were based on those measured just after the COSTAR mirrors had been coated; in the year between coating and launch the reflectivity had degraded by a few percent due to small amounts of molecular contaminants and some dust covering introduced in the COSTAR vibration testing. The apparent "loss" compared to the previous Handbook is offset by a corresponding increase in encircled energy at all radii, since the total flux is made smaller. All of this sounds like a long-winded discussion, but it is merely to explain why the DQE measurements presented here are significantly different from those in the previous version of this Handbook. An even more thorough discussion is given in FOC Instrument Science Report FOC-080.

The fluxes of the spectrophotometric standards within 1" were compared with synphot predictions. The spectrophotometric standards had been recalibrated using the best model of the white dwarf star G191B2B to redetermine the IUE sensitivity calibration (a correction of approximately 10% in the 1200-2000 Åwavelength range). It was found that the observed/expected flux values depended on wavelength linearly for the reasons outlined in the previous paragraph, so the DQE curve was transformed by this linear function to derive the new DQE curve.

The overall (OTA + COSTAR + FOC) central absolute quantum efficiency $Q(\lambda)$ in counts photon^{-1} with no filters in the beam is plotted and tabulated as a function of wavelength in Figure 28 and Table 10 for the four FOC imaging and spectrographic configurations. The data represent the product of in-orbit measurements for the new F/96 relay+OTA absolute quantum efficiency, and ground-based reflectance calibrations of the COSTAR mirrors for the new F/48. The predicted loss of light from two reflections of MgF_2 coated aluminum COSTAR mirrors amounts to a 20% loss in the visible and a 35% loss in the ultraviolet. The loss due to the COSTAR mirrors is more than compensated by the improvement in image quality, since the encircled energy performance is improved from 18% within a 0.1" radius to $\simeq$80% within the same area, based on theoretical PSFs.

The spectrograph efficiency is shown for the four orders of the grating (I, II, III and IV) with no order sorting filters in the beam. For the new F/96 relay, errors do not exceed ± 20% while, for the others, errors in the 2000–6500Å range for the imaging modes should not exceed ± 20% and for wavelengths below 2000Å they are expected to be of the order ± 50%. This latter uncertainty should be applied to all the spectrograph data especially in the orders III and IV.

6.3.1 Format-dependent Effects

It has been found that the DQE is a function of detector format (see Instrument Science Report FOC-075). The cause of this is not known. The relative sensitivities for each format are given in Table 11, where the 512X512 format is set to 1.0 by definition. The DQE values given in Table 10 and Figure 28 refer to the 512X512 format.

Table 11: Format-Dependent Sensitivity Ratios

Camera	Format (FxL)	Relative Sensitivity
F/96	512zx1024	1.25
	512zx512	1.45
	512x512	≡1.0
	256x256	1.20
	128x128	1.23
F/48	512zx1024	1.44
	256zx1024	1.28
	512x1024	1.02
	512x512	≡1.0
	256x256	0.85

6.4 DETECTOR BACKGROUND

The detector background arises primarily from thermal electrons at the first photocathode and high energy particles. In the 600 km altitude, 28° inclination orbit of HST, substantial fluxes of magnetospheric electrons and protons are encountered in the South Atlantic Anomaly (SAA). The more energetic of these particles are capable of generating intense flashes of Ĉerenkov radiation in the MgF_2 faceplate of the FOC intensifiers. Since this noise source originates as photons at the very front end of the detector, the Video Processing Unit of the FOC is not able to distinguish between real celestial photons striking the cathode and Ĉerenkov generated photons.

The threshold energy for Ĉerenkov radiation in MgF_2 is $E > 220$ keV for electrons and $E > 400$ MeV for protons. Shielding of 4 mm aluminum or more was built into the design of the FOC in order to prevent electrons of energies $E < 3 - 5$ MeV from reaching the detectors from any direction.

The effects of the SAA on the FOC were extensively mapped during the commissioning phase. The FOC turned out to be considerably less sensitive to SAA electrons than had been feared. This is presumably due to the additional shielding to electrons provided by the rest of the HST spacecraft. The response of the FOC to SAA protons on the other hand is in good qualitative agreement with the expectations—although the sensitivity of the two FOC detectors differs somewhat.

The highest background rates (0.2 counts pixel^{-1} s^{-1} in the new F/48 and 0.02 counts pixel^{-1} s^{-1} in the new F/96) are encountered over South America within the peak of the

SAA proton density distribution. Since these rates are not high enough to cause damage to the FOC detectors, the FOC is kept fully operational during SAA passages. However, such high background rates do exclude useful scientific observations. A ground-track contour delineating the observed region of high background has been installed within the HST ground system in order that FOC observations not be scheduled within it. Users of the FOC need therefore not concern themselves with avoiding the SAA under normal circumstances (*i.e.*, periods not having unusually high solar activity). The typical detector background rates experienced well outside the SAA are 7×10^{-4} counts pixel^{-1} s^{-1} in the detector for the new F/96 relay and 2×10^{-3} counts pixel^{-1} s^{-1} in the detector for the new F/48 relay. Upward fluctuations of a factor ≈ 3 from these minimum values are, however, seen throughout the HST orbit. The minimum in-orbit background rates are, respectively, factors of ≈ 5 and ≈ 3 higher than the background rates measured during ground testing implying that the bulk of detector background counts are particle induced.

In addition to the orbital variations in the background rates, the detector for the new F/48 relay has exhibited a localized region of high background count rates seen as a 'white spot'. These high background events are most likely related to a delamination in the potting around the intensifier tube between the 8kV and 12kV supply lines. The region of high background rates is found near the center of the full format with an arc extending across the top of the full format as well.

The count rates in these regions vary, but are significantly higher than the normal background with rates ranging from 2-10 times the nominal rate. The regions can be seen in Figure A5 in the Appendix where the white spot has a count rate of 5.7×10^{-3} counts s^{-1} pixel^{-1} and a background region far from the spot only has a count rate of 2.83×10^{-3} counts s^{-1} pixel^{-1}. The count rates in the white spot and associated arc had been seen to be increase in intensity with usage. Any increase in the count rate in the region of the white spot and arc would eventually limit the usefulness of this relay for science.

The increase in background preceded the first failure of the F/48 camera to turn on, which occurred in September 1992. The high voltage tripped during its ramping up, at the beginning of an observation sequence. The F/48 camera was switched on again successfully in October 1992, and a number of darks and flat fields were taken which confirmed background values consistent with the ones previously measured. The next switch on attempt (January 1993) failed, but the F/48 was again successfully switched on December 22, 1993, before the deployment of the COSTAR corrective optics. The camera remained on for the duration of the observation. While the acquisition image showed a background level consistent with the previous dark count images, a preliminary analysis of the following frames showed immediately that the background increased dramatically with time, eventually reaching saturation levels approximately two hours after HV switch-on. Figure 29 shows the background count rate for all the exposures, where the triangles are the estimated background levels at the center of the image in counts s^{-1} pixel $^{-1}$. Whether this characteristic of increasing background is a permanent condition of the F/48 is not clear. **As a consequence, the F/48 will not be made available to GOs during Cycle 5, pending further testing and analysis.**

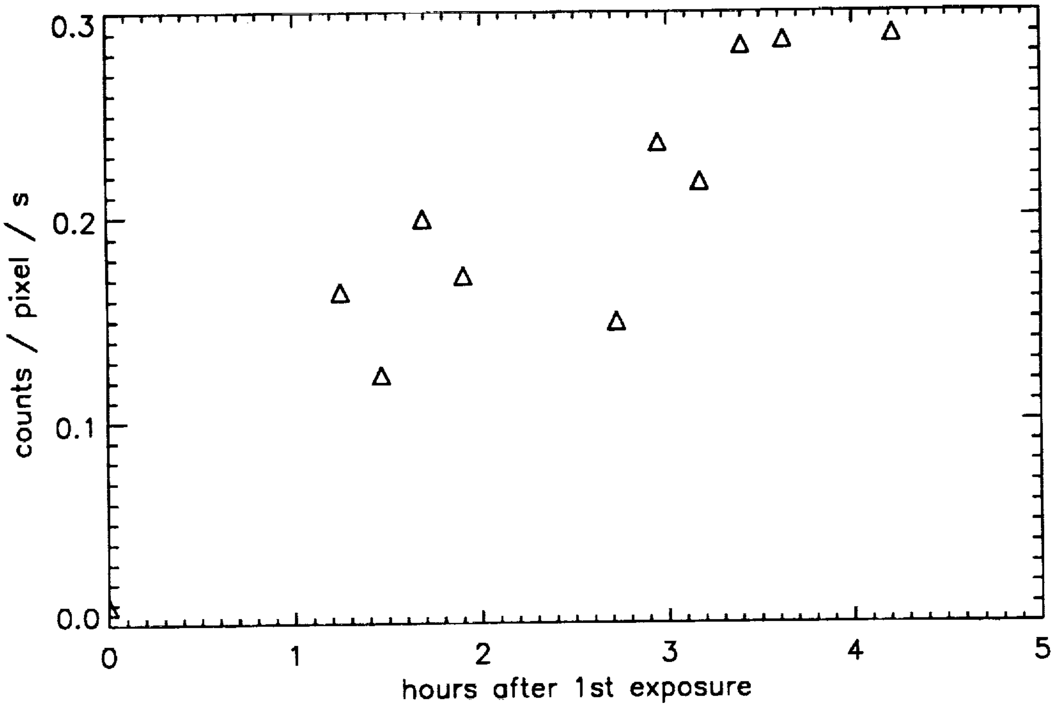

Figure 29. A steady increase in the background count rate has been observed during the most recent F/48 relay turn-on.

6.5 STRAY LIGHT

Normally, the FOC background is dominated by the detector, by zodiacal light in the visible and by geocoronal Lyman alpha and diffuse galactic light in the far UV (see Section 7 for detailed calculations of these components). When a bright object such as the Sun, Moon or the bright Earth limb is nearby, however, it may be dominated by stray light reaching the OTA focal plane due to scattering from the baffle system, the OTA tube and dust on the mirror. The expected brightness of stray radiation at the OTA focal plane due to the proximity of the Moon or bright Earth limb in the daytime part of the orbit in V magnitudes arcsec^{-2} as a function of the angle between the Moon or the limb and the OTA axis is shown in Figure 30. The two curves shown correspond to the two values of the primary mirror's dust coverage of 2% and 5% presently estimated to bracket the expected range of this parameter in orbit. The spectral shape of the stray radiation in the case of the Earth can be assumed to be, for most practical purposes, that of the Earth's average daylight nadir radiance given in Figure 31.

The average zodiacal light background of 120 S10 corresponding to $V \simeq 23$ magnitudes arcsec^{-2} is reached at angles greater than 80° to the limb, approximately. For viewing configurations in which the angle is less than this value, stray light will dominate in most situations. One of the most interesting of these is that encountered when observing in the continuous viewing zones (CVZ) which, in principle, allows for long uninterrupted integrations of very faint sources. Due to the altitude of the spacecraft and the depression of the horizon, the off-axis angle to the Earth limb in the CVZ will be in the range 20° – 44°, approximately. From Figure 30, the expected stray light illumination in this configuration in the visible will be between 18th and 20th magnitudes arcsec^{-2}. This means that observations in the visible will be limited mainly by this source of background. Specifically, assuming that one wishes to observe a $B \simeq 25$ magnitude A0V star with the new F/96 relay and the F430W blue filter with an accuracy of 10%, a background of this type of average brightness $V = 19$ magnitudes arcsec^{-2} in the CVZ requires an exposure time of 45 minutes or almost the entire daylit part of the orbit. At night, such an accuracy would be obtained in 16 minutes. Below 3000Å, this effect will be negligible as shown in Figure 31. Non-CVZ observations can also have bright limb approaches of 20° – 44° unless DARK TIME, which is very inefficient, is specified.

This particular example also shows that there is no advantage in exploiting the CVZ for long integrations or scheduling efficiency if the object is fainter than about 23rd magnitude since the gain in signal is more than offset by the increased background. Closing the shutter during the daylight pass, in other words, is recommended in this scenario. It is, therefore, of more than passing interest to the observers to pay some attention to the maximum allowable background they can tolerate for their specific observation and to communicate this information to the ST ScI in the Phase II proposal submission.

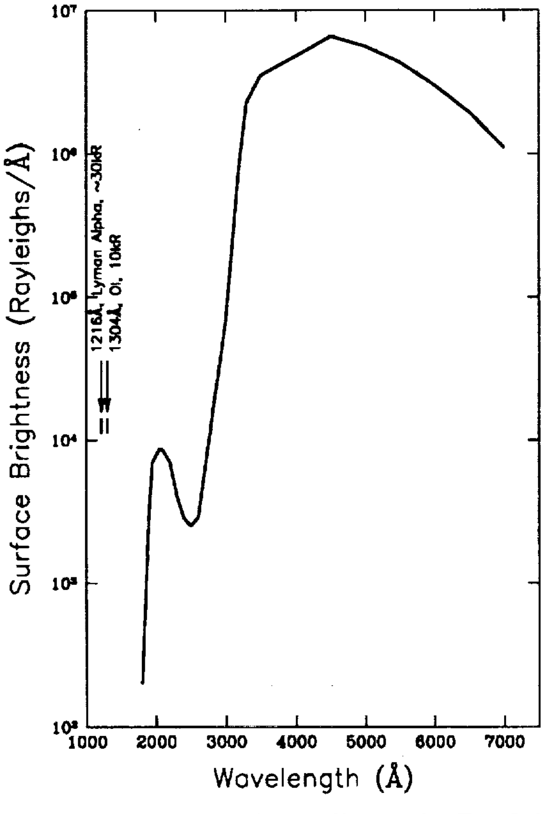

Figure 31. The Earth's average daylight nadir radiance in Rayleighs Å^{-1} *i.e.*, $10^6/4\pi$ photons cm^{-2} sec^{-1} Å^{-1} sr^{-1} as a function of wavelength.

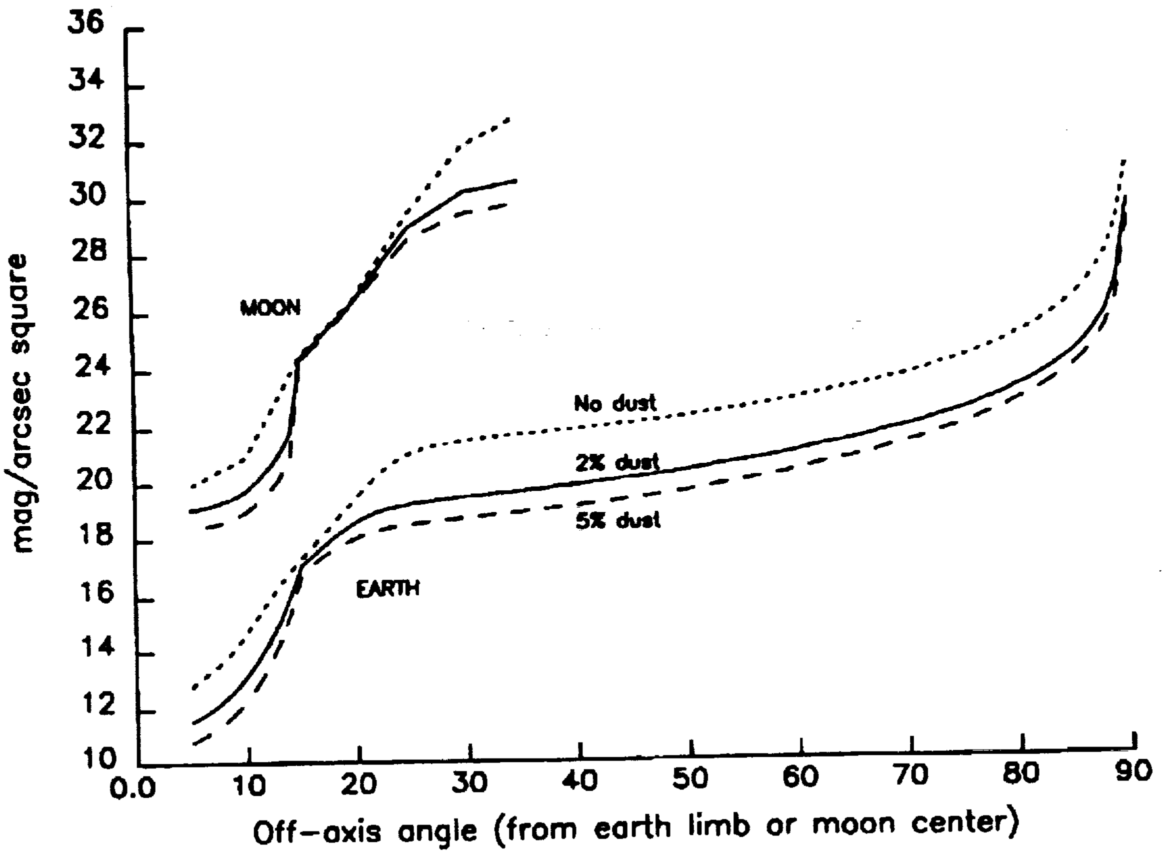

Figure 30. Stray light illumination in V magnitudes arcseconds^{-2} at the OTA focal plane due to the Moon and daylit Earth as a function of off-axis angle.

6.6 DETECTOR OVERLOAD

The FOC detectors described in Section 4.6 may be damaged by illumination levels exceeding 10^7 photons s^{-1} pix^{-1} at the photocathode due to point sources and by an average illumination from a diffuse source over the whole photocathode exceeding 10^4 photons s^{-1} pix^{-1}. Because of this danger, the 36 kV HV power supply on the 3 stage image intensifier is set to trip off when the point source illumination exceeds the value given above or if the average illumination from a diffuse source exceeds 200 photons s^{-1} pix^{-1}. Thus, for safety reasons, no point source delivering more than 10^6 photons s^{-1} pix^{-1} at the photocathode or a diffuse source delivering more than an average rate of 100 photons s^{-1} pix^{-1} over the whole photocathode will be allowed to be imaged by the FOC. These values correspond to an 9th magnitude blue star or a diffuse source of surface brightness 10 magnitudes arcsec^{-2} viewed through the F430W filter with the new F/96 relay. Targets brighter than this limit can still be observed by the FOC, provided that 1) enough neutral density filters are selected, so that a linear countrate is observed by the FOC, 2) the Bright Object Acquisition procedure is used to acquire the target onto the FOC aperture.

6.7 OVERHEAD TIMES AND MULTIPLE EXPOSURES

Assuming that the standard science data dump operations at the 32 kHz rate apply, it will take a constant 3.9 minutes plus a variable component to transition from the absolute time tag to stop an exposure to the absolute time tag to start the next one. The variable component depends on the mode change required and can be up to another 3.5 minutes for the worst case with the new F/96 relay (4 filter wheels) to 1.9 minutes for the worst case with the new F/48 relay (2 filter wheels). Thus, it could take up to a total of 7.4 and 5.8 minutes of time between successive exposures with an average of approximately, 6 and 5 minutes for the new F/96 and the new F/48 relays, respectively. In some specific situations, it may be advantageous, in order to save time, to take multiple exposures without closing shutter or dumping science data. Up to 11 consecutive exposures of this type can be made. If no changes to FOC mechanisms are required, the time interval between exposures can be reduced to 23 seconds total. This is the fastest rate at which the FOC presently can be run provided the telescope can be slewed to a new position on the detector quickly enough to permit it.

All the overhead times reported here are to be considered approximated, and should not be used for an accurate calculation of the required time (See the Proposal Instructions for a detailed and accurate description of all the relevant overheads).

6.8 GUIDING MODES WITH THE FOC

If no special requirements are placed on the guiding tolerance of the HST, (see HST Phase II Proposal Instructions), the FOC will default to fine lock (estimated RMS jitter 0.005 arcseconds out of day/night transitions) for all configurations. These defaults can be overridden with the guiding tolerance special requirements for situations which do not strictly require the highest possible guiding accuracies. In this case the observer might require coarse track (estimated RMS jitter of 0.015 arcseconds). Since this could prove quite beneficial in terms of overhead time (20 minutes for fine lock and 0 minutes for gyro hold), the user is encouraged to think carefully about his real requirements in this area. Gyro hold with an absolute position error of $\pm 60''$ arcseconds and a drift rate of 0.01 arcseconds s^{-1} is not expected to be used very often with the FOC but could find interesting applications for purely photometric measurements.

6.9 UNIFORMITY OF RESPONSE (FLAT FIELDING)

The extended format ($512z\times$ 1024) geometrically corrected flat fields for both of the new relays are shown in Figures A1–A2. The new F/48 image shows the approximate location of the new default 512 × 512 format, which is no longer at the center, but close to the upper right quadrant. The flat fields were obtained from overlapped observations of the inner region of the Orion Nebula and are at 3727 and 1360Å respectively. The flat fields show a number of various types of features, some more subtle than others. The more evident features are the occulting fingers for the new F/96 relay, the slit finger for the new F/48 relay (used as a fiducial reference to the spectrograph slit) and the reseau marks. Because of the geometric correction, the edges of the original raw images can be seen as curved edges in these images, mainly on the left and right sides.

Because of the large amount of time necessary to obtain external flat fields for the FOC, these two UV flat fields (one for F/96 and one for F/48) are currently the only UV flat fields for the FOC. We plan to obtain another UV flat field at about 2200Å during 1994.

In all images, regardless of format, a number of pixels at the beginning of the scan line (i.e., starting at $S = 1$) are corrupted by defects in the beginning of the scanning sawtooth waveform. The number of pixels corrupted depends on the detector and format. Generally it is about 5% of the scan line for the new F/96 relay and relatively independent of format, whereas for the new F/48 relay it gets progressively worse with smaller formats (for the 128 × 128 format it is as much as 25% of the scan line). The faint horizontal stripes seen at small L values are due to a ripple instability of the coil drivers at the beginning of a frame.

The narrow line running from the bottom left corner to the upper right corner is due to the read beam not being completely blanked when it is forced to fly back to $S = 0, L = 0$ at the end of the frame. This feature is more noticeable with the smaller formats. The narrow horizontal features at the right edge, especially at $L = 256, 512, 768$, are due to noise glitches on the scan coil driver caused by changes in the most significant bits of the line counter. For both relays, the center 512 × 512 is seen outlined in larger formats. This effect is due to a burn-in of that heavily used format in the camera target so that a charge discontinuity at the edges of the format has appeared. The edges of a square baffle located just in front of the detectors limit the extended field of the new F/96 relay at the upper and lower left corners, the extended image field of the new F/48 relay on the upper left corner. The broad vertical bands (bright and dark) seen near the beginning of the scan line arise from ripples at the beginning of the scanning sawtooth waveform. The bands occur as a result of the varying pixel size which is a consequence of the varying scan rate at the beginning of the scan. A proper geometric correction would remove this effect; however, the distortion has a spatial scale smaller than the reseau spacing and thus does not get corrected. This effect should be corrected for in the near future. It must be noted that since the normal Routine Science Data Processing (RSDP) calibration of the images always uses the appropriate section of a full format flat field to flatten images obtained in all formats, these bands will not be flattened out in smaller formats (this is not necessarily undesirable, as will be discussed later).

The remaining features fall into two categories, large scale and small scale features. The large scale variations are due either to vignetting (significant only for the new F/48 relay) or detector response. The expected vignetting for the full the new F/48 full field format is shown in Figure 32*a* as a contour plot. Contours are shown as percentage transmission. The expected vignetting has not been included in the flat field for the new F/48 relay shown in Figure A1 so that features closer to the edge can be better seen. Figure 32*b* shows the vignetting function along the long slit.

Contour plots of smoothed flat fields, including the effects of vignetting for the new F/48 relay, are shown in Figure 33. A gaussian with a FWHM of 9 pixels was used to smooth the image and the result was normalized to 100 at the center. Figure 34*a* and 34*b* show a plot of row 300 of a UV flat field for the new F/48 relay and the new F/96 relay respectively to give a better idea of the size of the flat field variations.

All previous indications are that the relative variations in large scale response as a function of wavelength between 1300 and 6000Å are weak; generally speaking, the large scale response does not change more than 10% at all pixels except at the edges and corner of the full format. Figure 35*a* and 35*b* show contour plots of the ratio of the Orion Nebula derived

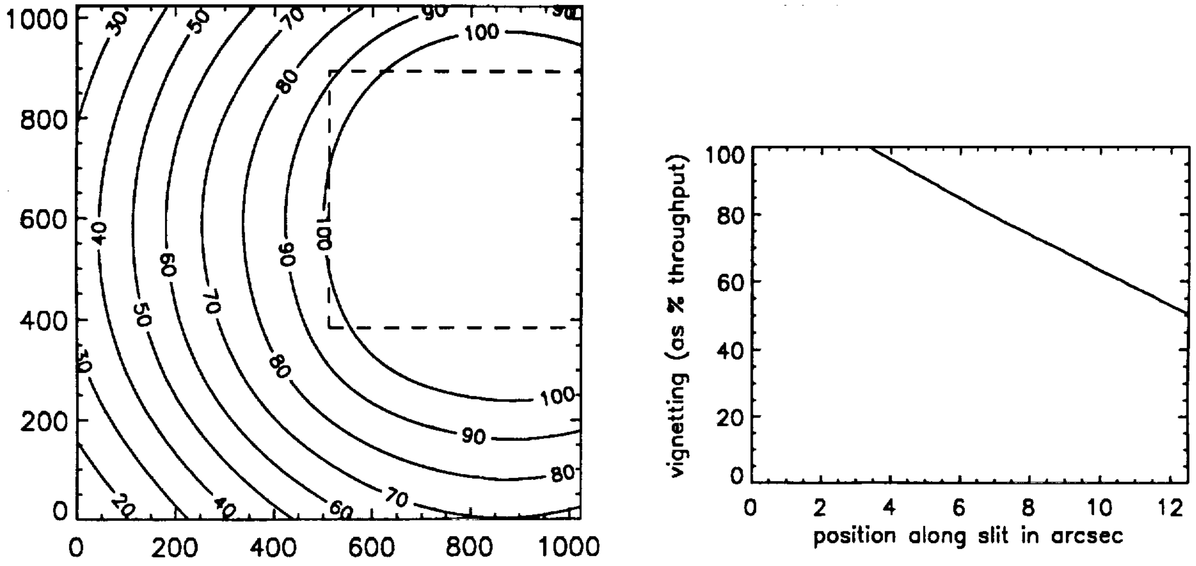

a. b.

Figure 32. **a.** Contour plot of the vignetting function for the new F/48 relay across the entire photocathode, with the location of the primary 512 × 512 imaging format shown (dotted line). **b.** Plot of the vignetting function along the spectrographic slit.

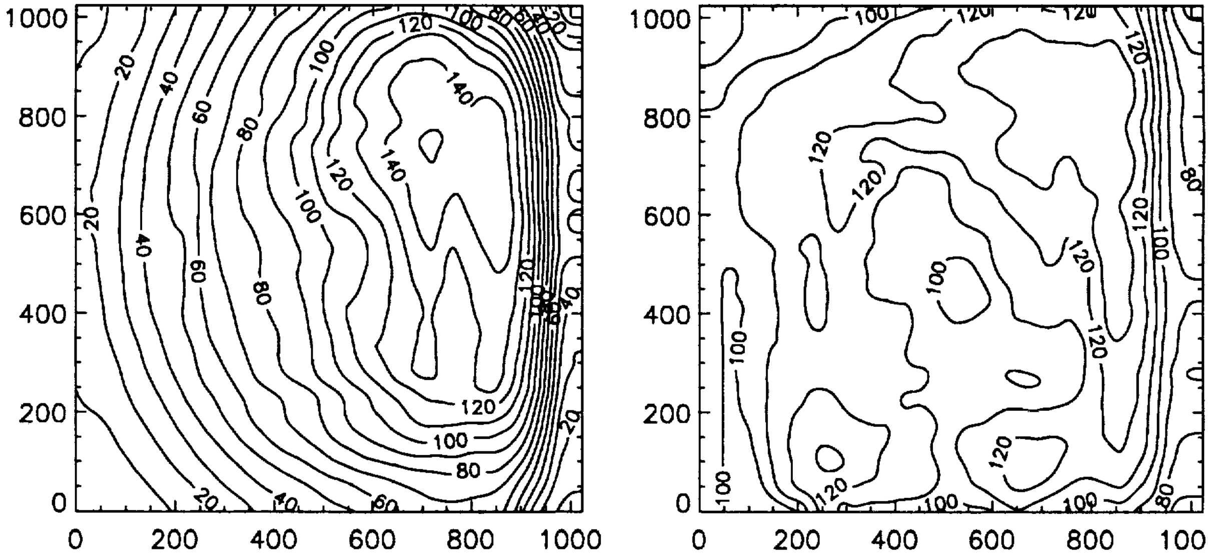

a. b.

Figure 33. **a.** Contour plot of the smoothed flat field for the new F/48 relay, including the effects of vignetting. **b.** Contour plot of the smoothed flat field for the new F/96 relay.

flat fields to those obtained from the onboard LEDs for the new F/48 and the new F/96 relays respectively.

Beyond 6000Å, the flat fields begin to change significantly, generally with poorer relative sensitivity towards the corners. Although the changes in the large scale response with wavelength are relatively minor, the changes in the fine scale features is more pronounced. Scratches and other small scale defects deepen in the far UV; for the new F/96, some scratches exhibit as much as a 30% decline in sensitivity in the far UV. Another source of fine scale nonuniformity is the presence of patterns—unfortunately not fixed. Although not always easily seen in low count extended areas or flat fields, there are two different patterns always present. The more noticeable one is an approximately sinusoidal pattern with the peaks and troughs oriented at an approximately 45 degree position angle and a period of 3.35 pixels for the new F/96 relay. It is believed to originate from a moiré effect between a TV tube grid and the diode array on the target. The RMS amplitude of this pattern is approximately 5% for the new F/96 relay and 2.5% for the new F/48 relay (the peak deviations from a flat response due to this pattern are at least twice these values). This pattern becomes intensified when count rates are in the nonlinear regime and thus is much more easily seen. In fact, it is a quick way of recognizing serious nonlinearity in an image. The pattern noise disappears at very low count rates.

A second pattern arises from some form of interference with an FOC digital timing waveform that has a 4 pixel period. It shows up as vertically striped patterns on the flat fields. Although very coherent in nature with regard to orientation and frequency, the details of the modulation do not appear to remain constant from image to image. The RMS amplitude of this pattern is approximately 2.5% for both relays.

There also appears to be an intrinsic granularity in the fine scale response, i.e., effectively random pixel-to-pixel variations in response which has not yet been well characterized.

Some comments on flat field calibration are in order, especially with regard to the routine pipeline calibration. Small drifts in distortion of the order of a pixel result in misregistration of fine scale features such as scratches between the flat field and the science image. Flat fielding the data in this case actually worsens the effects of the fine scale features by correcting the wrong pixels. For this reason and because FOC flat fields are of relatively low signal to noise (typically 300-500 counts per pixel), the flat fields used in RSDP are heavily smoothed to eliminate most of the fine scale features. As a consequence, they are not corrected for in the calibrated outputs of RSDP.

Unsmoothed flat fields are available from STEIS, and by using them, it is often possible to improve the flat fielding by the appropriate registration of the flat field to the science image. But this requires scientific judgment and must be applied on a case-by-case basis.

As previously mentioned, the startup oscillations in the scanning waveform result in uncorrected distortion at the beginning of the scan. The observer should keep in mind, however, that although it appears to be a flat fielding issue since it manifests itself in flat fields, it does not affect the total flux from an object—it just redistributes it. If one is doing aperture photometry on stars, for example, one is likely to introduce more errors in flattening out the effect than in leaving it alone. The ultimate solution would be the improvement in the geometric correction files to remove the effect by means of geometric correction. It is expected that this will be done by mid-1994.

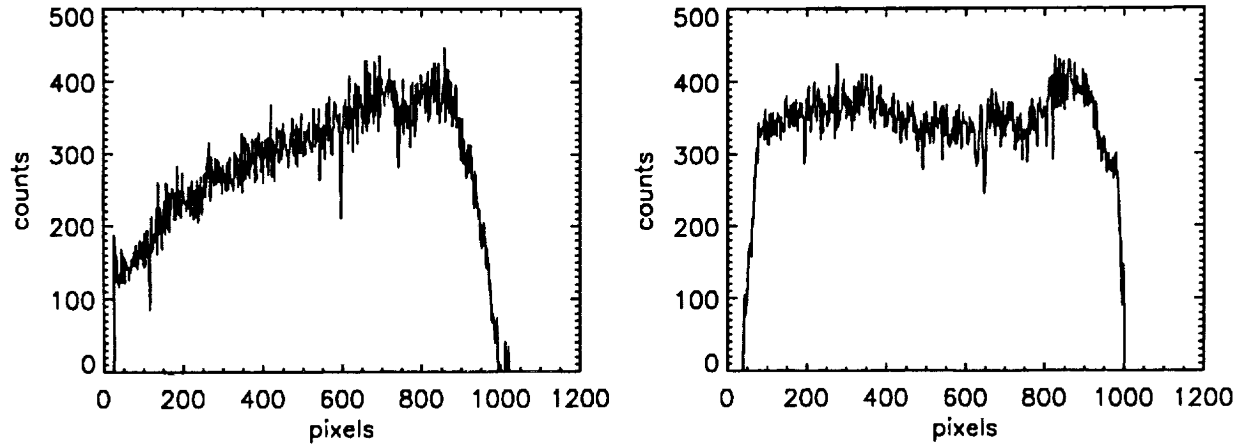

a. b.

Figure 34. Plots across row 300 of the UV flat field for the new F/48 relay (a) and the new F/96 relay (b). The effect of vignetting has not been included in plot (a).

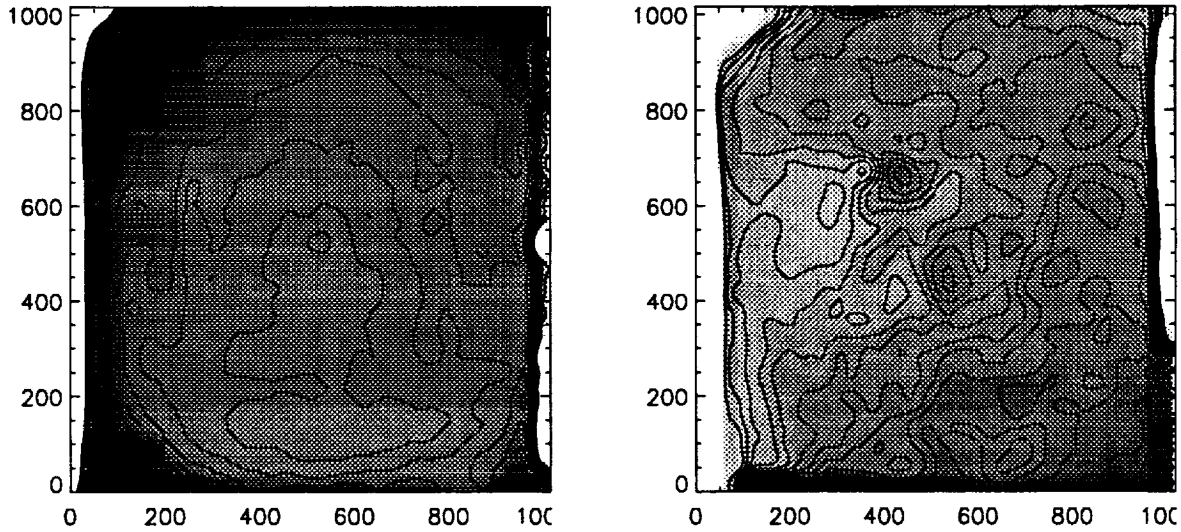

a. b.

Figure 35. Contour plot of the ratio between external UV flat field and internal LED flat field for the new F/48 relay (a) and the new F/96 relay (b) based on pre-COSTAR data. The expected effects of vignetting on the ratio for the new F/48 relay are not included. The center of each plot has been normalized to 1 with the contours at intervals of 2.5%.

One final effect should be mentioned. Although it is not a flat field issue, it appears to many at first glance to be one, and so it will be explained here. Many observers see a fringe or fingerprint type of pattern in the background of their calibrated images where the fringes are of relatively low spatial frequency—usually of periods of 20 or more pixels. It is a result of the geometric correction applied to the data. It does not appear in the raw data. What is being seen is not alternating areas of darker and brighter background, but rather, alternating areas of higher and lower variance in the poissonian noise of the background. This effect arises from the resampling algorithm used in the geometric correction—essentially what one is seeing is the effect of the pixels in the output, geometrically corrected image drifting in and out of phase with the corresponding pixels in the input, distorted image. Those pixels mapping directly to the center of a pixel in the input image result in little or no effective smoothing, while those which map to a point in between pixels in the input image will be an average of the input pixels and thus have smaller variance in the noise. A small amount of further smoothing to the geometrically corrected image will virtually eliminate the effect. The pattern is identical in all images as long as they use the same geometric correction file.

The achievable relative photometric accuracy depends on many factors, of course, and no simple rule of thumb will apply to all analysis. In many cases the accuracy depends on the amount of work an observer is willing to do to calibrate his data. For RSDP calibrated files, one should not expect the large scale accuracy to be better than 3-5% over the central region of the format, and should expect errors as large as 10% closer to the edges (much higher very close to the edges). Fine scale features can introduce large pixel-to-pixel errors (i.e., scratches and reseau marks). Scratches and blemishes can be dealt with by careful flat fielding. It is sometimes possible to remove the pattern noise with special techniques. Most important is to avoid placing targets on or near areas with serious photometric problems if possible. That is, keep targets of interest way from the edges of the format, burn-in regions, A/D glitches and known blemishes if more accurate photometry is desired.

6.10 VISIBLE LEAKS

Although the FOC narrow and medium band filters are the very best present technology can provide, they do exhibit a residual transmission of $\simeq 10^{-3} - 10^{-4}$ between 5000 and 6000Å where the detectors are still relatively sensitive. Consequently, indiscriminate use of these filters to isolate faint UV features from a bright visible background can lead to serious errors. The magnitude of the error is, of course, very sensitive to the precise shape of the spectrum of the source to be observed throughout the sensitive range of the FOC. Thus, it is not always sufficient to know only the expected flux of the source in the range $\lambda_0 \pm \Delta\lambda/2$ in order to estimate the expected count rate.

A striking example of a possible observing scenario that can be expected when imaging a bright visible source in the UV is shown in Figure 36. In the example shown in this figure, the source spectrum is assumed to increase sharply with increasing wavelength in the manner expected from an M supergiant star. If this source is fed into the new F/96 relay with the F231M filter on FW#3 in the beam, the resulting monochromatic count rate as a function of wavelength through the entire OTA+COSTAR+FOC system is shown by the curve marked F231M. The actual observed count rate in this configuration, of course, corresponds to the integral of this curve.

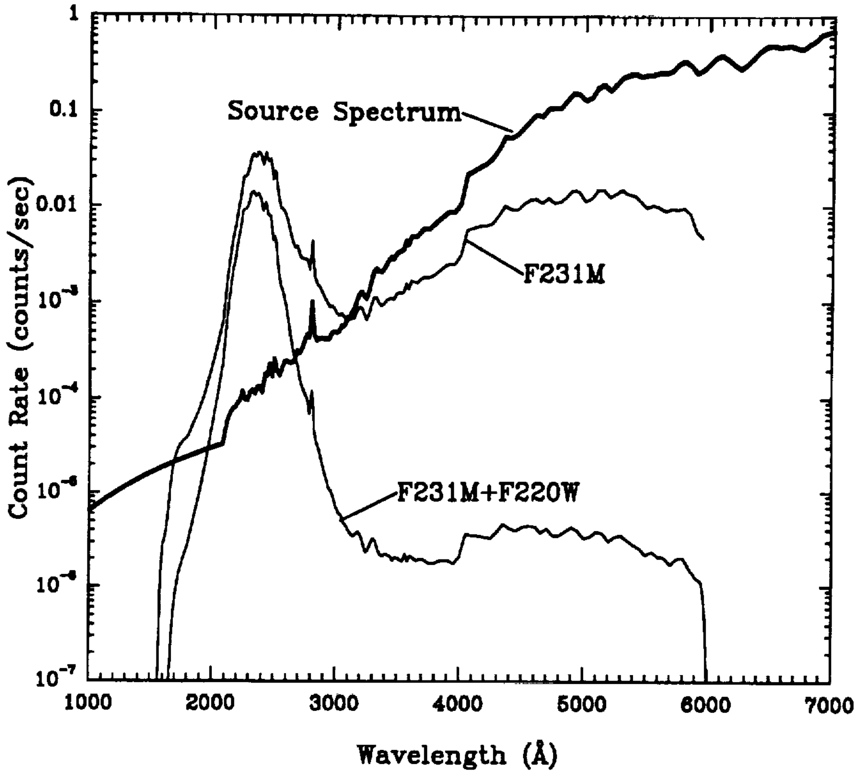

Figure 36. The expected monochromatic count rate as a function of wavelength for the new F/96 relay and the F231M filter or the F231M+F220W filters in the beam for an extended source whose spectrum varies as the curve marked SOURCE SPECTRUM. The source flux units are photons $\mathrm{cm}^{-2}\mathrm{sec}^{-1}\text{Å}^{-1}$.

If the F231M filter alone is used in this endeavour, the contribution of the flux within the band 2330 ± 115Å is only ≃ 18% of the total of 39 counts sec^{-1}. The counts originating from the region $\lambda > 2580$Å represent, in contrast, 71% of the total. In this admittedly extreme case, the thus derived UV brightness would be highly suspect, to say the least. Solutions to this problem are not easy to find but, at least for the new F/96 relay, one simple device would be to introduce a second cleverly selected filter into the beam in addition to the original one. This selection should be geared towards maximizing the suppression of the visible leak while minimizing absorption in the UV bandpass of interest.

In the case worked out in Figure 36, for example, the F220W filter on FW#2 is ideal as shown by the curve marked F231M+F220W. Now, the in-band fraction of counts amounts to 69% while the visible leak is only 5% or less of the total. The exposure time required to reach a S/N=10 in this case increases by a factor of six mainly because of the effective suppression of the visible counts.

Unfortunately, the new F/48 relay with its much smaller filter complement has far less flexibility in this regard than the new F/96 relay. In this case, another possible solution to the problem is to use the objective prisms to physically separate the UV from the visible. This technique works best for point or, at least, compact sources where spatial and spectral overlap is minimized. But even for extended sources, appropriate positioning of the target with respect to the dispersion axis of the prism can work quite well. At that point, the only remaining problem is to insure that the overload limit of the detector (described in Section 6.6) is not violated for the visible part of the image.

6.11 GEOMETRIC DISTORTION AND STABILITY

Because of the nature of the detectors, and the off-axis location of the instrument, the raw FOC data suffers from geometric distortion, *i.e.*, the spatial relations between objects on the sky are not preserved in the raw images produced by the FOC cameras. This geometric distortion can be viewed as originating from two distinct sources. The first of these, optical distortion, is external to the detectors and derives from the off-axis nature of the instrument apertures. The second, and much more significant source of distortion is the detector itself.

Geometric distortion is a fact of life when dealing with detectors containing image intensifiers, primarily because intensifiers rely on an electric field for accelerating, and a magnetic field for focusing the photoelectrons. Any variation in the uniformity of either results in image distortion within the intensifier. Photon positions are then further distorted in the process of "reading-out" the TV tube's target, firstly because the read-out beam is performing an angular sweep across a plane target, and secondly because of non-uniformities in the scanning rate of the beam. For this reason, each video format has individual distortion characteristics, and so unfortunately, the distortion measured for one format cannot be used to correct the distortion of an exposure taken in another format.

In order to measure and correct for the detector distortion, fiducial reference points (*reseau* marks) are etched onto the first of the bi-alkali photocathodes in the intensifier tube. (Since these reseau marks only transmit about 10for all practical purposes they cannot be flat fielded out.) These reseau marks form an orthogonal grid of 17 rows and 17 columns with a separation of 1.5 mm (60 pixels), each reseau being 75 microns square (3 × 3 pixels). The detector distortion can be determined by illuminating the photocathode with an internal light source, (*i.e.*, an internal flat field). The observed positions of the reseau marks, when compared to the expected positions, provide a map of the detector distortion across the field. The optical component of the distortion is determined independently from ray-tracing models of the HST and FOC optics, and is applied to the reference reseau grid to give the 'expected' positions.

Although the geometric distortion arises from several sources, the correction of images is carried out in a single step using a flux-conserving algorithm which maps values from the raw, distorted image into a geometrically corrected image. A two-dimensional polynomial transformation, which combines both the optical and detector distortion components, is used to provide the mapping of distorted pixel coordinates to corrected coordinates. Figures 37 and 38 show as an example the magnitude of the distortion field as determined for the pre-COSTAR F/48 and pre-COSTAR F/96 cameras using their $512z\times$ 1024 formats, from inflight calibrations.

The squares show where a regular grid of points on the sky (using a 60 pixel spacing) should have appeared if there were no distortion; the ends of the line segments show where the grid points actually appear in the distorted image. (The lines have been multiplied by a factor of 2 to make them more easily visible, *e.g.*, a line length of 50 pixels represents a distortion displacement of 25 pixels). The pixel coordinates shown refer to normal, square pixels, rather than the rectangular, zoomed pixel mode the images were obtained in.

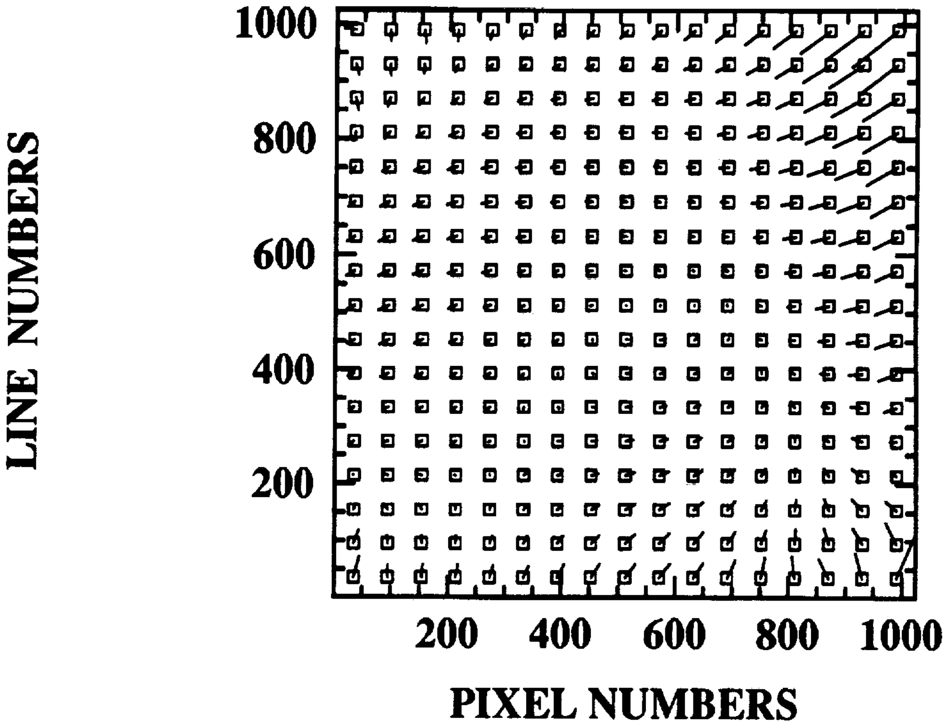

Figure 37. The 512z× 1024 format distortion field for the new F/48 relay.

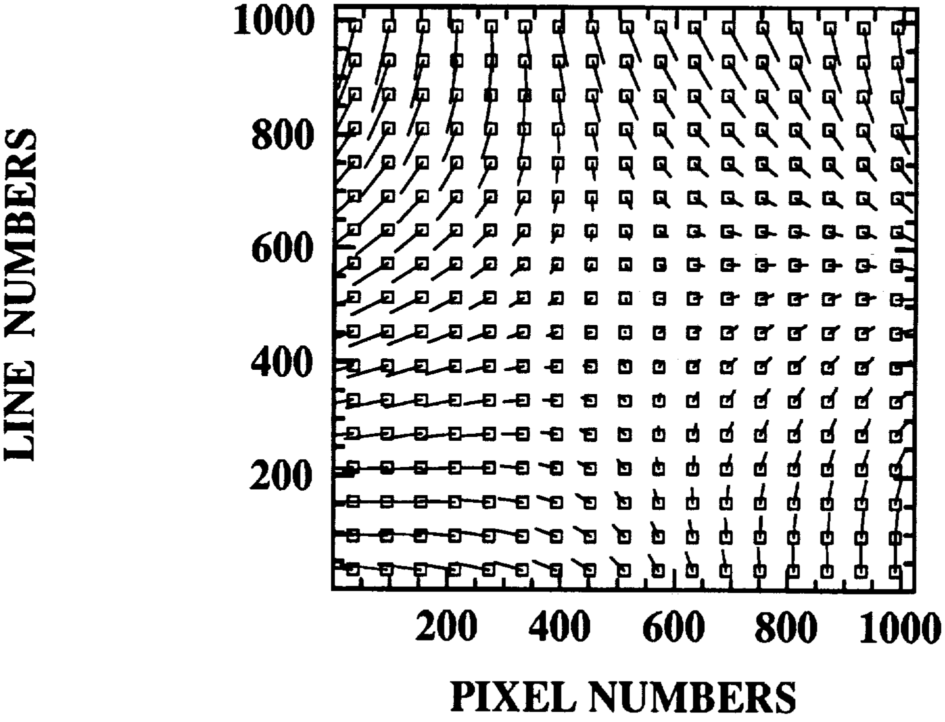

Figure 38. The 512z× 1024 format distortion field for the new F/96 relay.

In order to carry out geometric correction of FOC data, *i.e.*, to recover an image in which the spatial relationships between objects are restored, a necessary requirement is that the geometric distortion field, shown in Figures 37 and 38, must be stable. By this we mean that there must be no significant change in the observed reseau positions with time.

Short term variation of the geometric distortion pattern occurs during the period immediately following FOC high voltage switch-on. During this time the observed reseau positions show an RMS deviation from the stable positions of approximately 1-2 pixels. This period however, extends for only about 40 minutes, by which time the reseau position have stabilized to within 0.5 pixels, which is considered adequate for imaging purposes. In order to avoid this period of instability, the scheduling software automatically inserts a delay interval immediately following high voltage switch-on which prevents exposures being taken during this time. Long term variations in the geometric distortion were expected to occur as a result of desorption and out-gassing in the OTA and instruments, however given the time since launch, the desorption curve is now considerably flatter and out-gassing should be very near stable. Consequently, effects on distortion are much smaller and are taking longer to materialize. Based on our experience;

a. The new F/96 relay continues to be very stable, the geometric variation in the new F/96 relay has shown only about 1-2 pixels of movement over this period, (which theoretically should be the worst time).

b. The situation with the new F/48 relay is somewhat less certain since monitoring of the pre-COSTAR F/48 relay has shown it to be considerably less stable, with several large, unexplained changes in the geometric configuration. Any future new F/48 data must be considered to be poorly characterized with respect to geometric distortion.

Future determination of the new F/96 relay's geometric distortion will be based on observations of dense starfields and thus should be able to correct for the high spatial frequency variations in scan rate much better than the existing geometric corrections which are derived from the reseau grid.

6.12 PLATE SCALE

The plate scale (*i.e.*, the pixel size in arcseconds) has been determined for the two cameras in the FOC before the deployment of COSTAR. This was done by taking a series of images of a pair of astrometric stars, moving the telescope between exposures by a predetermined angular offset. The measured distances (in pixels) between the astrometric stars, combined with the known separation (in arc seconds) then give us the plate scale.

For the new F/96 relay the plate scale is 0.01435 arcsec pixel^{-1} (±0.0002) based on observations of an astrometric star field with the post-COSTAR F/96 relay. Extrapolating from the new F/96 results, the plate scale for the new F/48 should be 0.02825 arcsec pixel^{-1} (±0.0002).

These values are "radial" plate scales and are within a few percent of the nominal values, which will be *vis.* 0.014 arcsec pixel^{-1} for the new F/96 relay, and 0.028 arcsec pixel^{-1} for the new F/48 relay.

7.0 OBSERVER'S GUIDE(PRESCRIPTION FOR ESTIMATING EXPOSURE TIMES)

The first step consists in specifying the required signal to noise ratio S/N or the relative accuracy $\delta N/N = (S/N)^{-1}$ of the measurement. Then, the exposure time required to attain that accuracy is given, in general, for Poisson statistics, by:

$$t = (S/N)^2(R_S + 2R_B)R_S^{-2} \tag{1}$$

where R_S is the source rate and R_B the background rate in an appropriate resolution element in counts sec^{-1}. The problem then simply reduces to properly estimating R_S and R_B.

For a point source in the FOC field of view and for a count rate per pixel much less than N_{MAX} calculated from Table 9, the source rate is given by:

$$R_S = \frac{\pi}{4}D^2(1-p)\int_o^\infty \epsilon(\lambda)F(\lambda)Q(\lambda)T(\lambda)d\lambda \tag{2}$$

where:

$D =$ diameter of the ST primary = 2.4 meters
$p =$ ratio of obscured area to total area of primary mirror = 0.138
$\epsilon(\lambda) =$ fraction of energy intercepted by the appropriate resolution element
$F(\lambda) =$ source flux at ST in photons $\mathrm{cm}^{-2}\mathrm{sec}^{-1}$ Å^{-1}
$Q(\lambda) =$ FOC+OTA response function for $T(\lambda) = 1$ in counts photon $^{-1}$
$T(\lambda) =$ transmission of filters or efficiency of dispersing elements

The terms in eq. (2) can be assumed to be appropriate averages over the pixel to pixel variations in the instrument response function. $Q(\lambda)$ and $T(\lambda)$ are plotted in Figures 28 and 11 through 15.

The background rate, on the other hand, can be expressed, in general, as:

$$R_B = nz\left[B_p + \frac{\pi}{4}D^2(1-p)\Omega^p\int_o^\infty I^B(\lambda)Q(\lambda)T(\lambda)d\lambda\right] \tag{3}$$

where:

$n =$ number of normal (z=1) or zoomed (z=2) pixels in appropriate resolution element
$B_p =$ inherent detector background count rate per normal pixel
$I^B(\lambda) =$ specific intensity of diffuse background at ST in photons $\mathrm{cm}^{-2}\mathrm{sec}^{-1}\mathrm{sr}^{-1}$ Å^{-1}
$\Omega^p =$ solid angle subtended by a normal FOC pixel in steradians.

Equations (2) and (3) can be evaluated numerically or by approximating them by assuming that the spectral passband is sufficiently narrow. This permits the following simplifications:

$$R_S \simeq 3.9 \times 10^4 \epsilon(\lambda_0)F(\lambda_0)Q(\lambda_0)T(\lambda_0)\Delta\lambda \tag{4}$$

$$R_B \simeq nz\left[B_p + \frac{6.9 \times 10^{-10}}{K} I^B(\lambda_0)Q(\lambda_0)T(\lambda_0)\Delta\lambda\right] \tag{5}$$

where all the relevant functions are evaluated at wavelength λ_0 of peak response and $\Delta\lambda$ is the FWHM bandpass of the instrument in Angstroms. The latter two parameters are listed in Table 3. K takes on the numerical values 1 and 4 for the new F/48 and the new F/96 relays, respectively.

For an extended source, the size of the resolution element nz is determined by the user according to his application. For a point source, the encircled energy tabulated in Table 8 should be used to determine $\epsilon(\lambda)$ and nz for each specific case. The precise area to be used depends in general on the S/N ratio. If it is very high, one can afford to increase the size of the resolution element nz to collect more photons, if it is low, nz should be kept as small as possible. For any particular situation, there is an optimum nz at which the S/N is maximum for a given exposure time t or at which t is minimum for a given S/N ratio. A few quick calculations should be enough to locate this condition once the background has been properly defined as indicated in the next paragraphs.

At least two sources of diffuse background have to be considered in estimating $I^B(\lambda_0)$ in eq. (5). The first is residual airglow above the ST altitude of 500-600 km. For the FOC bandpass of 1200–6000Å only two features need to be considered: the HI, Lyman α line at 1216Å and the OI, 1304Å triplet. The latter feature need only be considered for daytime observations. Their contribution to R_B can be evaluated via the graphs shown in Figure 39. In this graph, the second term in the brackets in eq. (5) is evaluated for the three FOC relays for the condition $T(\lambda_0) = 1$ as a function of spacecraft position in the orbit and for a zenith oriented line of sight. Solar zenith angle 0° corresponds to local noon, 180° local midnight. Lyman α intensities can be expected to increase approximately a factor of 40% if the line of sight drops to the horizon. R_B can be determined by multiplying the data on Figure 39 by the appropriate T(1216Å) or T(1304Å) and nz and adding to B_p.

The second source of background is zodiacal light, which can be an important contributor to R_B in the 3000–6000Å range. This contribution as a function of wavelength is plotted in Figure 40 for the three relays. An intensity of 90 S10 units ($\simeq 3 \times 10^{-4}$ photons $\mathrm{cm^{-2}sec^{-1}sr^{-1}Å^{-1}}$) and a standard solar spectrum is assumed in these calculations. This corresponds to a line of sight direction of ecliptic latitude $\beta = 40°$ and helioecliptic longitude $\lambda - \lambda_{\odot} = 85°$. Thus, R_B for the zodiacal light can be computed by multiplying the results shown in Figure 40 by the appropriate nz $T(\lambda_0)\Delta\lambda$ and by the factor S/90 where S can be computed for any target position by means of the data tabulated by Levasseur-Regourd and Dumont (*Astr. Ap.*, 84, 277, 1980) and reprinted here for convenience as Table 12.

7.1 POINT SOURCES

How all this works in practice is best illustrated by some examples.

7.1.1 Imaging

How all this works in practice is best illustrated by some examples. Say that you are interested in observing an unreddened A0V star of $m_u = 24$ with an accuracy of 10% using the F342W filter, and the new F/96 relay with normal sized (unzoomed) pixels for which $z = 1$. From Table 3 for the F346M filter, you find that $\lambda_0 = 3480$Å, $\Delta\lambda = 434$Å, $QT(\lambda_0) = 0.045$. The stellar flux $F(\lambda_0) = 8.0 \times 10^2 \times 10^{-0.4\times24} = 2.0 \times 10^{-7}$ photons $\mathrm{cm^{-2}sec^{-1}Å^{-1}}$. Inserting these values into eq. (4), you get $R_S = 0.15 \times \epsilon(\lambda_0)$ counts $\mathrm{sec^{-1}}$. This is the total count rate from that star spread out over a certain number of pixels corresponding to the $\epsilon(\lambda_0)$ chosen from Table 8. If the star is reddened by a given total extinction A_V, you should use a standard or average reddening curve (see Savage and Mathis, *Ann. Rev. Astr. Ap.*, 17, 73, 1979 for an example) to deduce the appropriate $A_{\lambda 0}$. Then, R_S can be multiplied by $10^{-0.4A_{\lambda 0}}$ to take this effect into account in the simplest possible way. The possible

Table 12: Zodiacal Light Intensities in S10 Units

β $\lambda-\lambda_\odot$	0°	10°	20°	30°	40°	50°	60°	70°	80°	90°
180	180	152	127	105	89	76	66	59	58	63
170	161	147	123	104	89	76	66	59	58	63
160	147	134	113	98	86	75	65	59	59	63
150	140	129	107	91	80	71	63	58	59	63
140	139	129	105	87	75	67	62	58	60	63
130	141	132	105	86	74	65	61	59	60	63
120	147	138	108	88	75	66	61	59	61	63
110	158	148	113	91	78	68	63	61	62	63
100	175	160	120	96	82	72	65	62	62	63
90	202	176	130	103	87	76	68	64	63	63
80	239	197	144	113	94	82	72	67	64	63
70	296	228	162	124	103	88	77	69	65	63
60	394	275	190	143	116	96	82	72	66	63
50	572	355	238	173	135	108	89	76	67	63
40	920	510	316	220	160	123	95	80	68	63
30	1930	825	475	285	194	140	103	84	70	63
20				355	226	157	111	88	73	63
10					260	167	117	90	74	63
0					275	170	118	90	74	63

inaccuracies introduced by this method are probably not worse than the uncertainties on the validity of the reddening curve itself and/or the prediction of the continuous flux to be observed.

Next, calculate R_B from eq. (5) using the data in Figures 39 and 40. Far ultraviolet airglow is not going to be a factor in the B bandpass. The zodiacal light background per pixel can be estimated by means of the data graphed in Figure 40 and Table 12. Suppose the star is viewed at $\beta = 15°$ and $\lambda - \lambda_\odot = 120°$ for which S=120 S10 units. Then, this contribution is $2.3 \times 10^{-7} \times 120/90 \times 0.58 \times 434 = 8 \times 10^{-5}$ counts sec^{-1} per normal pixel so that, assuming $B_p = 7 \times 10^{-4}$ counts sec^{-1} per normal pixel, eq. (5) can be written as:

$$R_B/n \simeq 7 \times 10^{-4} + 8 \times 10^{-5} = 8.0 \times 10^{-4} \text{ counts s}^{-1} \text{ pix}^{-1}$$

Then, the required exposure time can be easily computed from eq. (1) and the data in Table 8 for $\epsilon(\lambda_o)$. Using the data in the column marked F346M, one obtains:

n	ε(3400Å)	R_S(cs^{-1})	R_B(cs^{-1})	t(sec)
1	0.087	0.013	0.0008	8639
9	0.409	0.061	0.007	2016
21	0.528	0.079	0.017	1811
37	0.601	0.090	0.030	1852
69	0.722	0.108	0.055	1869
97	0.773	0.116	0.078	2021

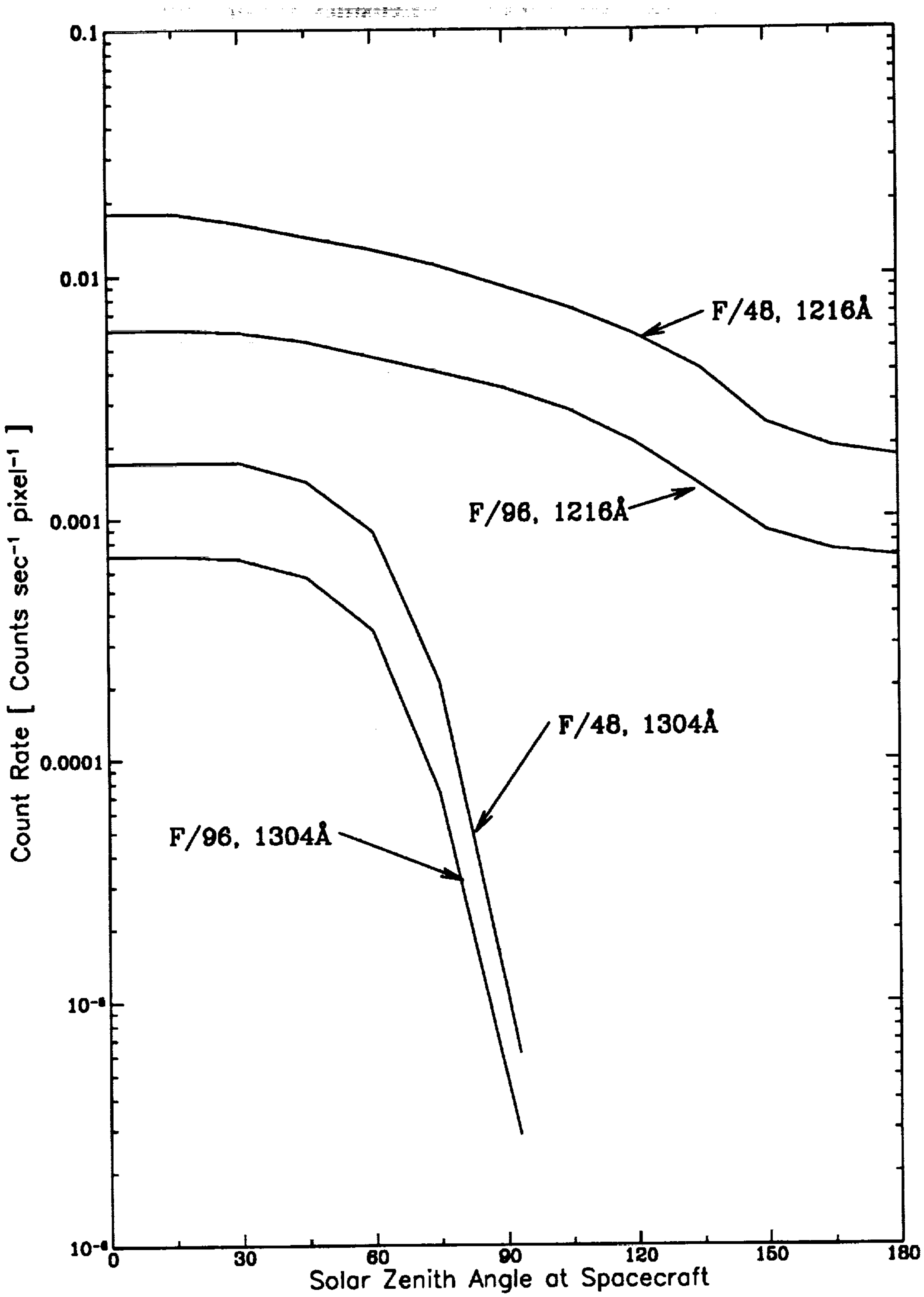

Figure 39. Residual 1216 and 1304Å airglow contribution to the FOC background counting rate with no filters in place in counts sec^{-1} per normal pixel as a function of the solar zenith angle at the spacecraft at 500km altitude. The line of sight is assumed to be oriented towards the zenith.

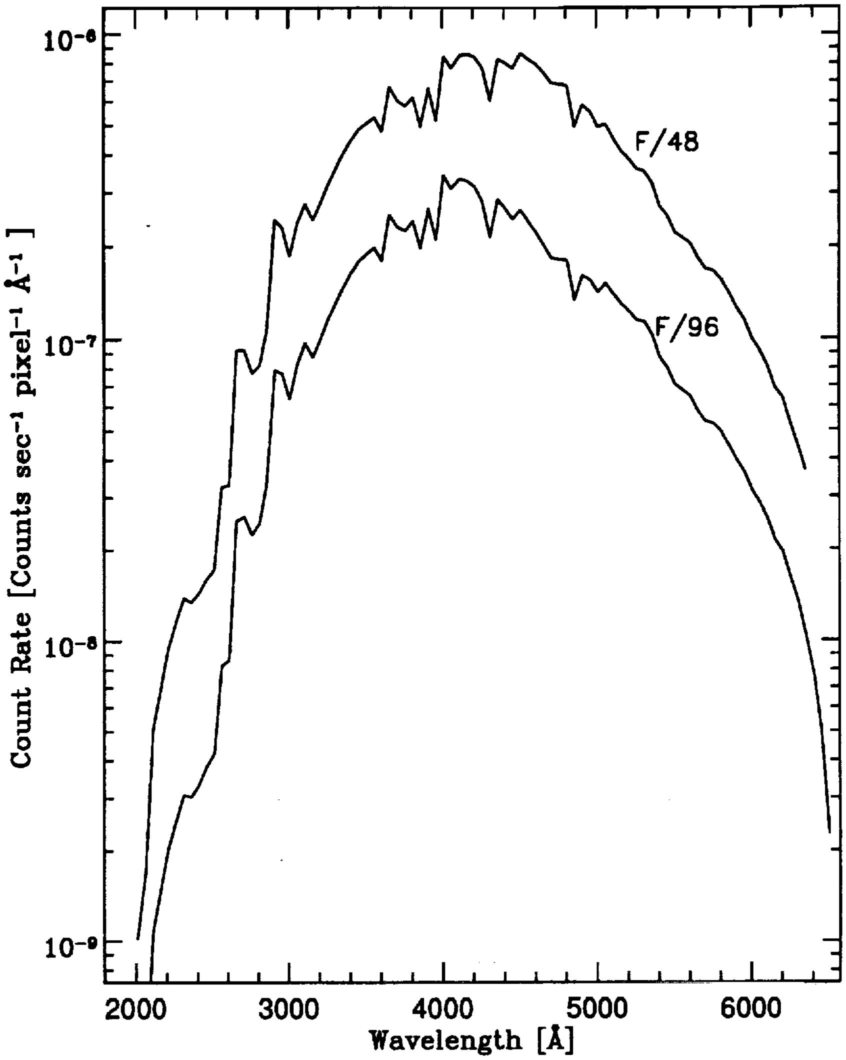

Figure 40. Zodiacal light contribution to the FOC background counting rate with no filters in place in counts $\sec^{-1}$ Å^{-1} per normal pixel as a function of wavelength. The zodiacal light intensity is assumed to be 90 S10 units.

Thus, integrating under the PSF out to a radius of 0.036 arcseconds at $n = 21$ provides enough flux for the required S/N to be achieved in a minimum exposure time of 1800 seconds. If the background rate for some reason had been 5 times higher, the minimum exposure time would have been 3500 seconds at $n = 9$.

The accuracy of this approximation is, of course, a sensitive function of the shape of the instrument bandpass and is, therefore, expected to be highest for the narrow, well-defined passband filters with negligible red and/or blue leaks. It will certainly only give rough order of magnitude estimates for the wide band pass filters for which a numerical integration of eq. (2) is required for higher confidence predictions. If there are other point sources within a few Airy radii of the primary source, their contribution to the background R_B must be evaluated by means of the appropriate system point spread function. It should also be kept in mind that some background sources may vary in intensity during an exposure. This will be the case for the airglow or scattered light emission sources for exposures lasting a good fraction of an ST orbit (see Section 6.5). In this situation, it is advisable to pick the worse case intensity to evaluate the required exposure time.

Particular attention has to be paid, in any case, to the expected count rate since it may violate the assumption that $R_S n^{-1} \ll N_{\mathrm{MAX}}$ (see Table 9 and Section 6.2.2). If it does for the particular format chosen as indicated in Table 6, either the format must be changed or a neutral density filter inserted in order to drop the expected rate below the threshold. This, of course, will also result in an increase in the exposure time required to reach the required S/N ratio.

7.1.2 Spectroscopy

Similar computations can be carried out for a point source in the slit of the spectrograph for the new F/48 relay except that, of course, the long slit spectrograph efficiencies plotted in Figure 28 have to be used in equations (4) and (5). The bandpass $\Delta\lambda$ is now naturally limited by the projected slit width of 0.06 arcseconds corresponding to 4, 2, 1.3 and 1Å for first, second, third and fourth order, respectively. The transmission of the order sorting filter also has to be taken into account with special attention devoted to possible higher order confusion if the filter has an appreciable near uv and visible leak and the source has appreciable emission in these regions. This confusion can be eliminated completely for point or pseudo point objects with the use of the objective prism FOPCD as the cross disperser. In this case, the transmission and the dispersion of the prism given in Table 5 have to be factored into the calculations.

For the case of the objective prisms, eq. (4) can be rewritten in the form:

$$R_S(\lambda) = 3.9 \times 10^4 \varepsilon(\lambda) F(\lambda) Q(\lambda) T^{op}(\lambda) T(\lambda) \delta\lambda$$

where T^{op} is the transmission of the prism tabulated in Table 5 and $\delta\lambda$ is the wavelength interval in Å corresponding to the FOC spatial resolution. This interval can be expressed simply as:

$$\delta\lambda = 2r(\lambda) D(\lambda) PS^{-1}$$

where $D(\lambda)$ is the prism dispersion in Å mm^{-1} tabulated in Table 5, $r(\lambda)$ is the radius of the circle enclosing the required energy $\epsilon(\lambda)$ in arcseconds given in Table 8 and PS is the plate scale of the appropriate relay in arcseconds mm^{-1} given in Section 3. Then, the source count rate around λ is:

$$R_S(\lambda) = 7.8 \times 10^4 \epsilon(\lambda) r(\lambda) D(\lambda) F(\lambda) Q(\lambda) T^{op}(\lambda) T(\lambda) PS^{-1} \tag{7}$$

Equations (3) and (5) for the noise calculations remain the same except that some simplification can be introduced due to the fact that the overwhelming sources of background in the case T(λ) = 1 are the system integrated zodiacal light and the geocoronal Lyman α line. Thus, in this case, eq. (5) can be written as:

$$R_B = nz \left[B_p + \frac{2.7 \times 10^{-5} S}{K} + \frac{c}{b}(7.7 \times 10^{-4}) I^{kR} \right] \tag{8}$$

where $c = 0$ for the NUVOPs and the FUVOP and FOPCD in the new F/48 relay, $c = 1$ for the FUVOPs on the new F/96 relay, $b = 1$ for the new F/48 relay, and $b = 2$ for the new F/96 relay. S is the intensity of the zodiacal light in S10 units and I^{kR} is the intensity of the Lyman α airglow in kilorayleighs.

To see how this works, suppose you want to observe a 20th visual magnitude QSO with a ν^{-2} spectrum and you want to compute the required exposure time to obtain a S/N=10 at 1700Å with the FUVOP of the new F/96 relay. In this case, F(1700Å)=10^{-5} photons $\text{cm}^{-2}\text{sec}^{-1}\text{Å}^{-1}$. From the data tabulated in Table 8, you find r(1700Å)=0.08 arcseconds for ϵ(1700Å) = 0.7 and, from the data in Table 5, D(1700Å) = $11.72/24 \times 10^{-3}$ = 488Å mm^{-1} and T^{op}(1700Å) = 0.88 while Q(1700Å)=0.014 from Table 10. This means that the source rate from eq. (7) at 1700Å is 0.46 counts sec^{-1}. The count rate is spread over $n = 97$ pixels for $z = 1$ from Table (8). Assuming that S = 120 S10 for the zodiacal light, $I^{kR} = 5$ kilorayleighs, $B_p = 7 \times 10^{-4}$ counts sec^{-1} pixel^{-1}, and K=4, c=1, b=2, eq. (8) gives:

$$R_B = 97\left[7 \times 10^{-4} + \frac{2.7 \times 10^{-5} \times 120}{4} + \frac{7.7 \times 10^{-4} \times 5}{2}\right] =$$

$$97\left(7 \times 10^{-4} + 8.1 \times 10^{-4} + 1.9 \times 10^{-3}\right) = 0.33 \text{ counts sec}^{-1}$$

Finally, the required exposure time is:

$$t = \frac{100(0.46 + 2 \times 0.33)}{0.46^2} = 529 \text{ seconds.}$$

7.2 EXTENDED SOURCES

The prescription for an extended source deviates only slightly from the formulation discussed so far provided R_S is redefined as:

$$R_S = nz\frac{\pi}{4}D^2(1-p)\Omega^p \int_o^\infty I_S(\lambda)Q(\lambda)T(\lambda)d\lambda \tag{9}$$

$$= nz\frac{6.9 \cdot 10^{-10}}{K} \int_o^\infty I_S(\lambda)Q(\lambda)T(\lambda)d\lambda$$

where n is now the chosen number of normal ($z = 1$) or zoomed ($z = 2$) pixels in the required resolution element and $I_S(\lambda)$ is the specific intensity of the extended source in photons $\text{cm}^{-2}\text{sec}^{-1}\text{sr}^{-1}$ Å^{-1}. Equations (3) and (5) for R_B need not be modified. Conversion of other specific intensity units into photons $\text{cm}^{-2}\text{sec}^{-1}\text{sr}^{-1}$ Å^{-1} can be executed via the following relations:

Units	Photons cm^{-2} sec^{-1} sr^{-1} Å^{-1}
U magnitudes per arcseconds squared	$=3.2\times10^{13} \times 10^{-0.4U}$ at 3600Å
B magnitudes per arcseconds squared	$= 6.4\times10^{13} \times 10^{-0.4B}$ at 4470Å
V magnitudes per arcseconds squared	$= 4.3\times10^{13} \times 10^{-0.4V}$ at 5560Å
1 Rayleigh Å^{-1}	$= 8.1\times10^4$
1 erg $\text{cm}^{-2}\text{sec}^{-1}\text{sr}^{-1}$ Å^{-1}	$= 5 \times10^7\lambda$ (Å)
1 $\text{Wm}^{-2}\text{Hz}^{-1}\text{sr}^{-1}$	$=1.5\times10^{29}[\lambda(\text{Å})]^{-1}$

1 S10 =333

Suppose, for example, you want to observe a Lyman α aurora above the limb of Jupiter of intensity 20 kiloRayleighs with a spatial resolution of 0.28 arcseconds with a S/N = 10 with the new F/96 relay. You will be using 400 new F/96 pixels for this purpose. You should use the F120M filter because it has the highest transmission at Lyman α and the lowest transmission at the longer wavelengths where the disk Rayleigh scattering spectrum may overwhelm any far uv auroral features.

From Figure 13, you find that at λ =1216Å, the F120M filter has T=0.1 and from Table 10 you deduce that Q(1216Å)=0.008. Then, since in this case the Jovian emission line of width ≤1Å is much narrower than the instrumental bandpass of 86Å, eq. (9) can be written simply as:

$$R_S \simeq \frac{400 \times 6.9 \times 10^{-10}}{4} \times 2 \times 10^4 \times 8.1 \times 10^4 \times 0.008 \times 0.1 = 0.09$$

counts sec^{-1}per resolution element

The background rate R_B will be dominated by the detector background and the geocoronal Lyman α airglow if the observation is carried out at night. From the curve marked the new F/96, 1216Å in Figure 39 for a typical observing configuration of 150° local solar zenith angle, you obtain 2.2×10^{-3} counts sec^{-1} pixel^{-1} looking towards the zenith. This implies that, for $B_p = 7 \times 10^{-4}$ counts sec^{-1} pixel^{-1}, you have:

$$R_B = 400\left[7 \times 10^{-4} + 2.2 \times 10^{-3} \times 0.1\right] = 0.37$$

counts sec^{-1}per resolution element

This means that S/N=10 for this Jovian aurora and resolution can be reached in:

$$t = \frac{75(0.09 + 2 \times 0.37)}{0.092^2} = 2562 \text{ seconds}$$

Observations at higher spatial resolution would require correspondingly longer exposure times.

If this same aurora is to be observed against a planetary disk background of Lyman α emission of 15 kilorayleighs with the same accuracy, the relevant background rate becomes:

$$R_B = 400\left[7 \times 10^{-4} + 2.2 \times 10^{-4} + \frac{6.9 \times 10^{-10}}{4} 1.5 \times 10^4 \times 8.1 \times 10^4 \times 0.008 \times 0.1\right]$$

$$= 400\left[7 \times 10^{-4} + 2.2 \times 10^{-4} + 1.7 \times 10^{-4}\right] = 0.44 \text{ counts sec}^{-1}\text{per res. el.}$$

so that:

$$t = \frac{25(0.09 + 2 \times 0.44)}{0.092^2} = 2994 \text{ seconds}$$

In this case, however, you might be looking onto the visible disk of the planet and the visible leak will dominate the count rate. To estimate the visible leak contribution notice that at ≃5000Å, the F120M filter has a residual transmission of 10^{-4} and assume the Jovian spectrum to be solar with an intensity of $\simeq 2 \times 10^{6}$ Rayleighs Å^{-1} at 5000Å. Thus, you can approximate the effect by spreading this intensity over ≃1500Å where Q(λ) ≃0.03. Then, with these assumptions:

$$\begin{aligned} R_B &\simeq 0.44 + 400\left[\frac{6.9 \times 10^{-10}}{4} 2 \times 10^{6} \times 8.1 \times 10^{4} \times 0.03 \times 10^{-4} \times 1500\right] \\ &\simeq 0.44 + 50 \text{ counts sec}^{-1}\text{per resolution element.} \end{aligned}$$

A solution to this problem would be to insert another filter into the beam to suppress the visible contamination. A good choice would be F140W for which T(1216Å) = 0.05 and T(5000Å) = 3×10^{-4} and:

$$R_S = 0.09 \times 0.05 = 4.5 \times 10^{-3}\text{count sec}^{-1}\text{per resolution element}$$

$$\begin{aligned} R_B &= 0.44 \times 0.05 + 400\left[\frac{6.9 \times 10^{-10}}{4} \times 2 \times 10^{6} \times 8.1 \times 10^{4} \times 0.03 \times 10^{-4} \times 3 \times 10^{-4} \times 1500\right] \\ &= 0.02 + 0.015 = 0.035 \text{ counts sec}^{-1}\text{per resolution element} \end{aligned}$$

$$t = \frac{235(4.5 \times 10^{-3} + 2 \times 0.035)}{(4.5 \times 10^{-3})^2} = 9.2 \times 10^{4}\text{seconds} = 26 \text{ hours}$$

Obviously, this hypothetical program cannot be accomplished with the FOC. To reduce the exposure time to physically realistic levels one needs to, say, reduce the required accuracy and/or spatial resolution. For example, halving both the accuracy and the resolution yields a more acceptable exposure time of 1.6 hours.

Finally, suppose you wish to image an extended object (a planetary nebula, for example) with the new F/96 relay at the highest possible resolution in the zoomed configuration for the biggest possible field of view. Suppose the object exhibits a line spectrum with a surface brightness at Hβ of 5×10^{-13} ergs $\text{cm}^{-2}\text{sec}^{-1}$ arcsec^{-2} and you wish to use the F486N interference filter to isolate the line to an accuracy of 10%. From the data shown in Figures 12 and 28 you find that at 4861Å, $T = 0.6$, and $Q = 0.03$. From the conversion relations on page 78, you note that $I_s(4861) = 5 \times 10^{-13} \times 4.25 \times 10^{10} \times 5 \times 10^{7} \times 4861 = 5.16 \times 10^{9}$ photons cm^{-2} sec^{-1} sr^{-1}. Thus, eq. (9) becomes for $n = 1$, $z = 2$:

$$R_S = \frac{2 \times 6.9 \times 10^{-10}}{4} \times 5.16 \times 10^{9} \times 0.6 \times 0.03 = 0.03 \text{ counts s}^{-1} \text{ per zoomed pixel}$$

From the data shown in Figure 40 and a zodiacal light brightness of 90 S10 and $B_p = 7 \times 10^{-4}$ counts s^{-1} per normal pixel, eq. (5) becomes:

$$R_B = 2[7 \times 10^{-4} + 3 \times 10^{-7} \times 0.63 \times 34] = 1.4 \times 10^{-3} \text{ counts s}^{-1} \text{ per zoomed pixel}$$

because $T(\lambda_o) = 0.63$ and $\Delta\lambda = 34$Å for the F486N filter from the data in Table 3. In consequence, finally:

$$t = \frac{100(0.03 + 2 \times 1.4 \times 10^{-3})}{0.03^2} = 3644 \text{ seconds.}$$

8.0 THE FOC EXPOSURE TIME SIMULATOR, FOCSIM

The general procedures to compute the required exposure times for any FOC observing configuration and possible emission source outlined in the preceding section are perfectly adequate for most purposes including proposal preparation and feasibility verification. There are cases, however, where it is useful to have the means to evaluate more precisely the integrals in eqs. (2), (3) and (9). This capability is especially important when the emission source spectrum is not well behaved outside the wavelength range of interest (see, for example, the situations described in sections 6.10 and 7 concerning visible leaks), when the precise spatial distribution of counts in the image is important as in crowded fields and for more precise planning envisaged in Phase II of proposal preparation. For these and other possibly more complex situations, an exposure time simulator for the FOC has been developed by F. Paresce, Y. Frankel and W. Hack of ST ScI. This program, called FOCSIM, presently evaluates exactly the exposure times and S/N ratio for any imaging exposure. It also allows computation of the actual expected spatial patterns of the FOC images and, therefore, evaluation of the correct S/N for wide bandpasses and/or closely-spaced pairs of stars to simulate crowded field conditions.

FOCSIM, as presently configured, is a menu driven interactive FORTRAN program which runs under IRAF. It accepts user input describing the FOC observing configuration and the physical characteristics of an astronomical source to be observed and computes count rates, background levels and exposure times consistent with those inputs. The user may select from a number of synthetic spectra the radiation sources for the program or use his own file of wavelengths and fluxes in appropriate units. The sources resident in the program include 77 simulated stellar spectra covering a wide range of MK classes generated by the Kurucz (1979) stellar atmosphere models, a number of UV standard stellar spectra from IUE (*Ap. J. Suppl.,* 40, 1, 1979), a flat continuum between two wavelengths, up to three emission lines, a blackbody source of arbitrary temperature and a power low spectrum of arbitrary index. The normalization factors of flux and wavelength can all be specified arbitrarily by the user. Any of these sources can be made artificially extended by an appropriate change in scale and normalization factors, if so desired. Furthermore, the diffuse background can also be calculated precisely by FOCSIM. Presently, user supplied intensities of zodiacal light, for UV airglow, and inherent detector background can be accommodated.

In support of COSTAR, FOCSIM has been upgraded to allow for automatic selection of the COSTAR imaging modes. The latest DQE tables are available for use with FOCSIM for both of the new relays. These can be selected in the FOCSIM setup and can be found in the FOCSIM auxiliary directory. In addition to the new DQE tables, theoretical PSFs have been produced to simulate COSTAR corrected FOC PSFs and observed PSFs taken with the COSTAR-corrected FOC will soon be added to the FOCSIM libraries. Using the updated DQE tables and PSFs will allow FOCSIM to simulate COSTAR corrected observations with accuracies dominated by the errors inherent in the PSFs, either from modelling errors in the TIM PSFs or from small changes in focus or position in the COSTAR-corrected field of view. Initial experience in Cycle 4 has indicated that errors of about 10% in the simulated count rates should be expected.

The output of FOCSIM includes all relevant information on the input parameters selected, the appropriate instrumental parameters and subsidiary data such as the individual components of background, the monochromatic count rate shown in Figure 36, restrictions such as N_{MAX}, data on the magnitude of the red and blue leaks, and, of course, the resultant exposure times for the required accuracy. The user can also request that FOCSIM output the transmission curves for the filters and the source spectra as IRAF SDAS tables, which can subsequently be plotted using IRAF graphing procedures.

FOCSIM will be made available at the ST ScI to interested users of the FOC who have local accounts. Unfortunately, FOCSIM is not available for general distribution along with STSDAS for a couple of reasons: first, it uses additional libraries which are prohibitively large, and secondly, it does not conform to IRAF's standards for software programming. A beginner's manual is available upon request from ST ScI, either as a POSTSCRIPT file or a printed version. It describes the basic steps necessary for running FOCSIM by walking through a sample session. The manual also provides a list of the catalogs of spectra that are available for use with FOCSIM and samples of the output which FOCSIM produces. Additional on-line help has recently been added which can be accessed through the standard IRAF help facilities.

The STSDAS package of routines provided by ST ScI includes the SYNPHOT simulation package. FOCSIM and SYNPHOT share the same DQE and filter transmission tables ensuring that both packages utilize the most up-to-date throughput information in calculating count rates. However, SYNPHOT does not have the capability of providing any spatial information for any source as it does not work with either the PSFs or the encircled energy tables. Furthermore, SYNPHOT only works with source information and does not incorporate background sources, such as zodiacal light, into the calculations, resulting in the necessity of calculating the signal-to-noise and background count rate of an exposure by using the methods in Section 7. Although more limited than FOCSIM in the output products, SYNPHOT produces the same results as FOCSIM for the same input conditions. Therefore, either SYNPHOT or FOCSIM can be used for calculating the expected source count rate, but FOCSIM will automatically provide more information about the expected image.

9.0 LIMITING MAGNITUDES

FOCSIM can be used to predict the limiting magnitude of any observing configuration. An example of this type of calculation is shown in Figures 41 and 43 for scenarios matching the observed average in-flight conditions. Studies of calibration images have been used to determine an average zodiacal light intensity of S10 = 191 units and a detector background for the new F/96 relay of $B_p = 6 \times 10^{-4}$ and for the new F/48 relay $B_p = 2 \times 10^{-3}$ counts s^{-1} pixel^{-1}. Figure 41 shows the predicted exposure time in seconds needed to reach a S/N = 10 for a specified visual magnitude of a B5V star through the F342W (U) filter for the two cameras. With average in-flight conditions, we should expect to detect a B5V star of $V = 28$ with the U filter in about 10 hours of exposure time with the new F/96 relay. The limiting magnitude is $V = 27.5$ if a S/N=5 in a 5 hour exposure is deemed sufficient. Figure 42 illustrates the results of calculations using extended sources. For this case, the specific intensity of the source is expressed in terms of visual magnitudes per arcseconds squared and the spectrum is assumed to have the shape of a B5V star. The spatial resolution in this case is chosen to be 0.112 arcseconds, which corresponds to binned regions of 4 and 8 pixels on a side for the new F/48 or new F/96 relays respectively. One should be able to detect a source of intensity = $23.5V$ magnitudes per arcseconds squared at S/N = 10 and 0.112 arcsecond resolution in 10 hours of exposure with the U filter under the average in-flight conditions described earlier.

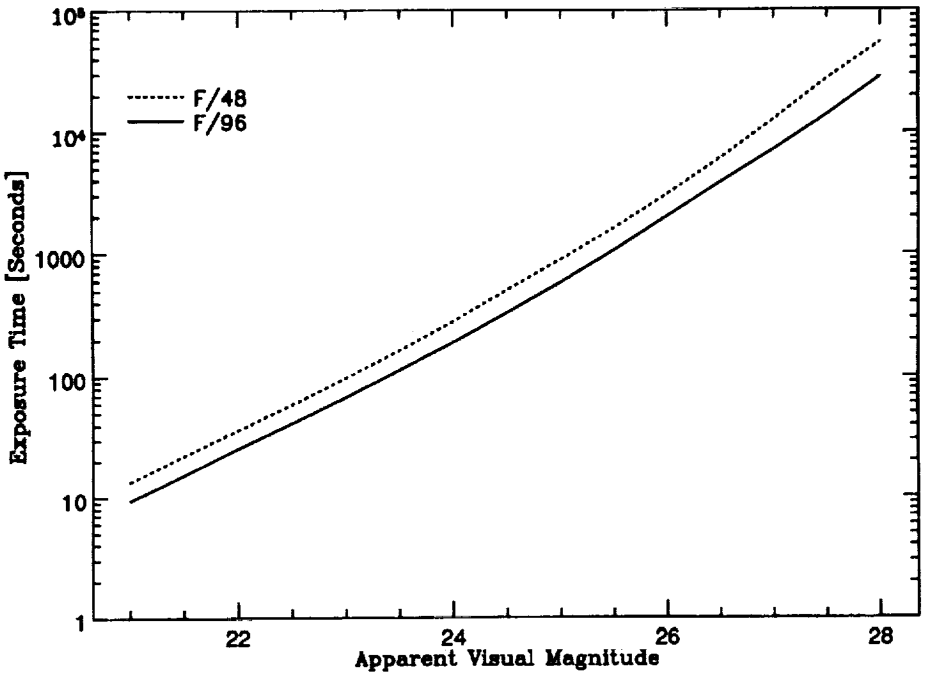

Figure 41. Exposure time required to reach a S/N = 10 on a B5V star with the U filter in an average observing condition with $B_p = 6 \times 10^{-4}$ counts $\sec^{-1}$ pixel^{-1} and a zodiacal light intensity of 191 S10.

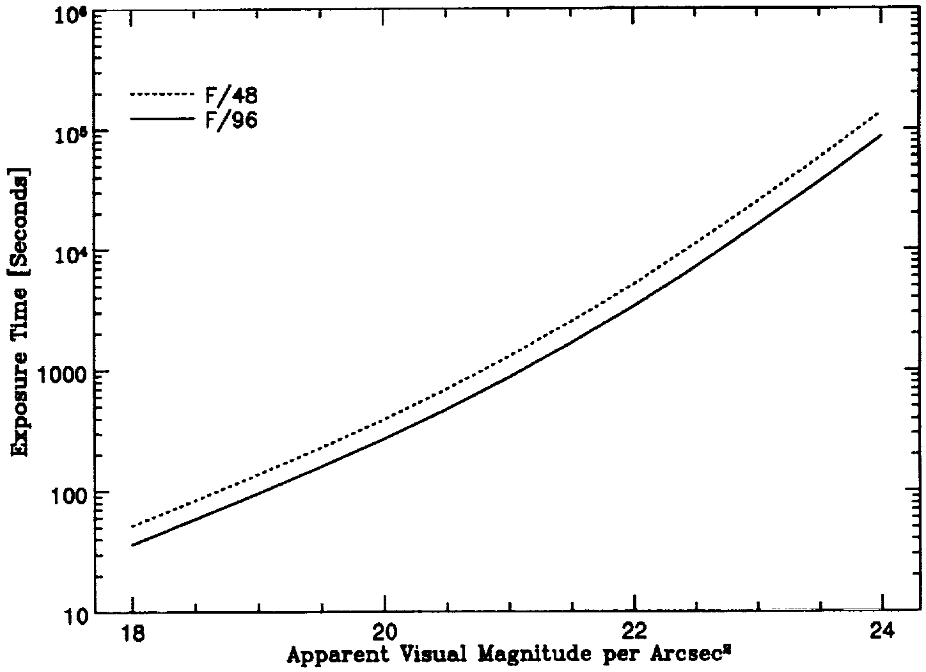

Figure 42. Exposure time required to reach a S/N = 10 on a B5V spectrum extended source with 0.1 arcsecond resolution with the U filter in the observing condition listed in Figure 41.

10.0 FOC DATA ANALYSIS AND PRODUCTS

10.1 PIPELINE PROCESSING

All data taken by the FOC are automatically processed and calibrated by the Routine Science Data Processing (RSDP), also called the "pipeline". It is possible to repeat, off line, the calibration part of the pipeline processing by using an IRAF/STSDAS task called CALFOC (CALibration of FOC data), used automatically by the pipeline. For every observation, the user will receive two sets of data coming out of the pipeline: the input and output files to CALFOC. The input files to CALFOC are:

1) the raw image,
2) a mask image characterizing the location of known bad pixels, reseaux, and likely data errors determined by online processing of transmitted data called the Data Quality File,
3) a file containing astronomical information related to the observation called the Standard Header Packet, and
4) a file containing engineering data related to the observation called the Unique Data Log.

The output files from CALFOC are:

1) the geometrically corrected image,
2) the geometrically and photometrically corrected image, and
3) a trailer file (*.trl) containing a log of the pipeline processing.

The data processing flow chart for normal imaging and spectrographic images is shown in Figure 43. CALFOC assumes that the processing parameters are in the image header, either directly from RSDP preprocessing, or inserted by task "cloadrsdpx" or "loadrsdpx". The processing parameters govern which correction steps are to be performed, and which calibration files are to be used. For normal imaging observations, the following steps are performed in order:

- dark count subtraction (not done at this time)
- format dependent photometric correction (using ITF reference file) (not done at this time)
- unzoom the zoomed image
- absolute calibration affecting header parameters only
- geometric distortion correction involving data interpolation and requiring a new mask image
- relative calibration or flat field correction (removing instrumental sensitivity variations) using UNI reference file, which is a reciprocal of a flat field.

For spectrographic (long-slit) observations, the final step is different i.e.:

- spectrographic relative and absolute calibrations with flux and wavelength calibrations affecting both data and headers.

In the spectrographic mode, several orders may overlap. The pipeline does not deliver separately calibrated data sets for each order, leaving line identification and order deconvolution to the user. The pipeline delivers the raw image and data sets corresponding to the results of the tasks as indicated in Figure 43. Detailed information on FOC calibration procedures and algorithms can be found in the "Requirements Section" of the "Design Manual, DRD-SOGS-SE-06-1," available from STScI. Some more general information is contained in the Calibration HST Data Set manual. See also the STSDAS Calibration Guide.

10.2 GENERAL PROCEDURES

All delivered images are REAL*4 datatype, to avoid integer rounding. The actual counts in each pixel are preserved as accurately as possible to permit immediate visualization of counting statistics and noise.

10.2.1 Dark-Count Subtraction

The dark-count reference file multiplied by the exposure time is subtracted from the input science file. The dark-count file is a full-frame image (512 × 1024), so if the science file is smaller than full frame then only the appropriate section of the dark-count file is used. Use "imarith" or "darkx" IRAF tasks. Standard processing does not apply the dark-count subtraction to images at this time.

10.2.2 Format-Dependent Photometric Correction (ITF)

These reference files are called ITF (Intensity Transfer Function) files for historical reasons. There is one such file for each format. The format-dependent correction is applied by multiplying the image from the previous step (i.e. the dark-count subtracted image) by the appropriate ITF file. Use "imarith" IRAF task. Standard processing does not apply the photometric correction to images at this time.

10.2.3 Correct For Zoom Mode

If the image was taken in zoom mode, the next step is to split the data values along the first image axis (the sample direction). The length of the first axis (NAXIS1) is doubled, and the length of the second axis (NAXIS2) is not changed. Use "dezoomx" IRAF task.

10.2.4 Compute Absolute Sensitivity

This does not affect the data values. The inverse sensitivity, pivot wavelength and RMS bandwidth of the optical mode selected are computed and stored in the header of the output image. The zero-point magnitude and the observation mode are also saved in the output header. Multiplying the data numbers in the image by the value of the header parameter PHOTFLAM and dividing by the exposure time converts to flux density F in units of ergs per square centimeter per second per angstrom. Use "evalband" IRAF task.

10.2.5 Geometric Correction

A raw FOC image is distorted by a few percent for two reasons, the optics and the detector. Both distortions are comparable in magnitude. The optical distortion was computed by ray tracing, and the detector distortion is measured by taking flat-field images and observing the positions of reseau marks that are uniformly spaced on the photocathode. A geometric correction reference file includes both optical and detector distortion. It gives the location in the input (distorted) image of each corner of every pixel of the output (corrected) image. The geometric correction is performed for each output pixel by adding up the counts in the corresponding region in the input image. This procedure rigorously preserves flux. Use "newgeom" IRAF task.

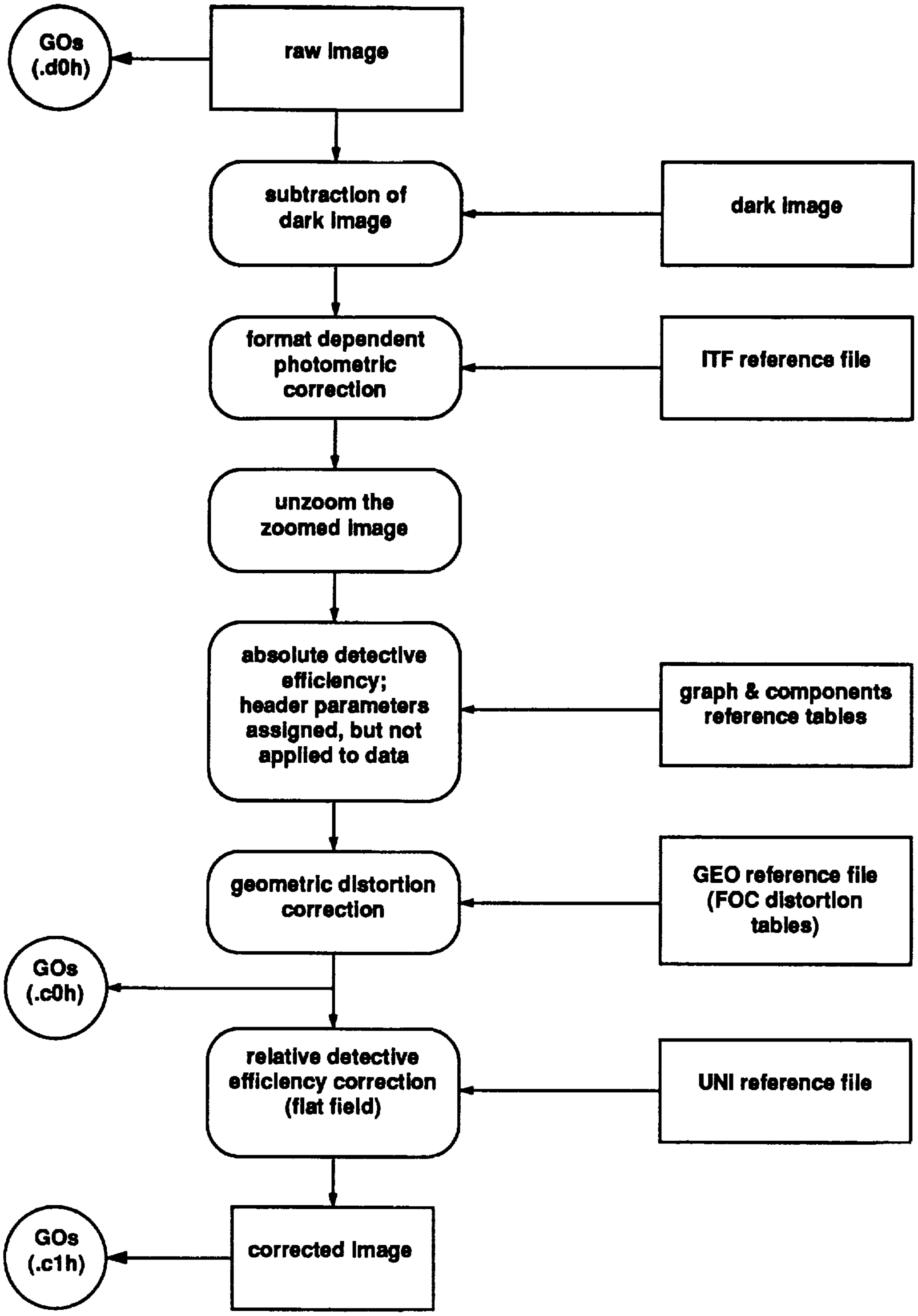

Figure 43. Flow diagram of FOC imaging data through the Routine Science Data Processing System.

10.2.6 Relative Calibration or Flat Field Correction (normal images only)

This correction is called the uniform detective efficiency (UNI) correction, and removes the nonuniform detective efficiency of the detector. It is applied by multiplying the image by the UNI reference file (format independent), which is the reciprocal of a flat field. The UNI files are full-frame in size, which is 1024 × 1024 because the image is dezoomed. As with the dark-count correction, if the science image is smaller than full-frame then only a subset of the UNI file is used. Since the sensitivity of the detector depends on wavelength, six different UNI files are provided for different wavelengths. For the new F/48 configuration, lambda = 3345 and 4800 Angstroms are provided; for the new F/96 configuration, lambda = 1360, 4800, 5600, and 6600 Angstroms are provided. The file to select is determined by comparing wavelengths of the UNI files with the pivot wavelength of the optical mode. Use "imarith" IRAF task.

10.2.7 Spectrographic Detective Efficiency Correction

The SDE correction is only applied to spectrographic images. It includes both the flat-field correction and a conversion from counts to flux density. It is applied after geometric correction because the absolute sensitivity depends on wavelength, and a major function of the geometric correction for spectrographic images is to align the spectrum with the axes and set the dispersion. The correction is applied by multiplying by a spectrographic detective efficiency reference file. The use of an order-selecting filter can change the location of a given wavelength on the photocathode, so there are several reference files; the appropriate one is selected based on the filters used. These files are full-frame (1024 × 1024), so only a subset will be used if the science image is smaller than this. Use "imarith" IRAF task. Standard processing does not apply the SDE correction to images at this time.

11.0 ACKNOWLEDGMENTS

This handbook could not have been written without the expert advice and assistance of our colleagues on the FOC team at the ST ScI. In particular, we are indebted to F.Paresce, D. Baxter, P.Greenfield, P. Hodge, M. Miebach and W. Baggett for supplying us with all of the information presented here.

The FOC has been brought to its present status by the devoted efforts of many groups including the ESA/ST Project Office Staff, the FOC Investigation Definition Team (IDT) and various industrial contractors (especially British Aerospace, Matra-Espace and Dornier System GmbH). The authors are particularly grateful to a number of people in these and other organizations that gave generous amounts of their time to assist us in producing this handbook. These are, in particular, the entire IDT, Richard Hook of ST/ECF, M. Saisse of the LAS/Marseille, and our colleagues P. Bely, C. Burrows, C.Cox, J. Crocker, R.Doxsey, G.Hartig, O. Lupie, P.Stanley at the ST ScI.

The FOC/IDT members are: R. Albrecht, C. Barbieri, J. C. Blades, A. Boksenberg, P. Crane, J. M. Deharveng, M. Disney, P. Jakobsen, T. Kamperman, I. R. King, F. Macchetto (Principal Investigator), C. D. Mackay, F. Paresce, and G. Weigelt.

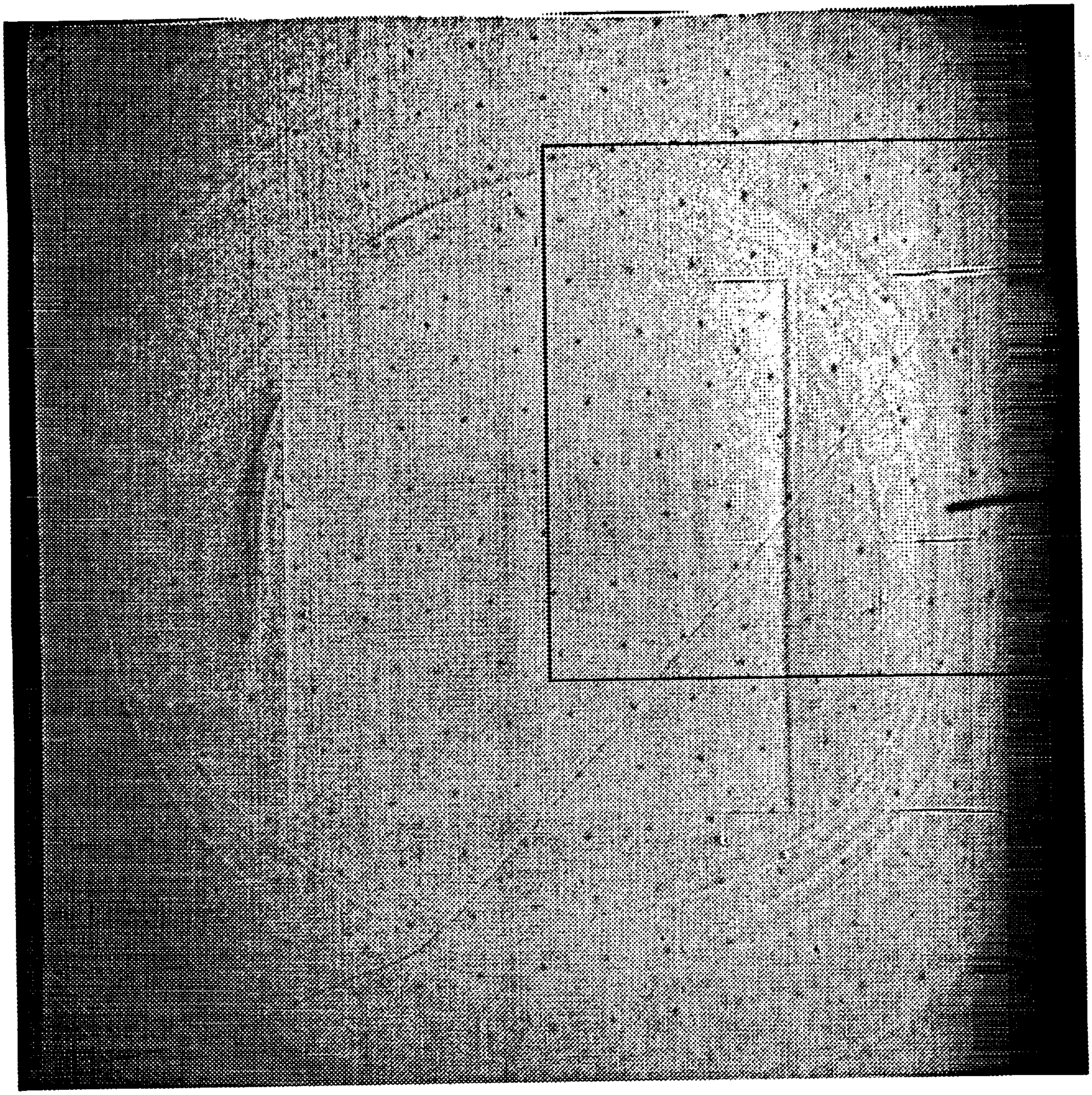

Figure A1. Extended format (512z× 1024) de-zoomed image taken with the pre-COSTAR F/48 relay under uniform external illumination. This image does not show the effects of vignetting that will be present after the installation of COSTAR. The slit finger is just visible at the right center edge inside the default 512 × 512 imaging format which is outlined with the solid line.

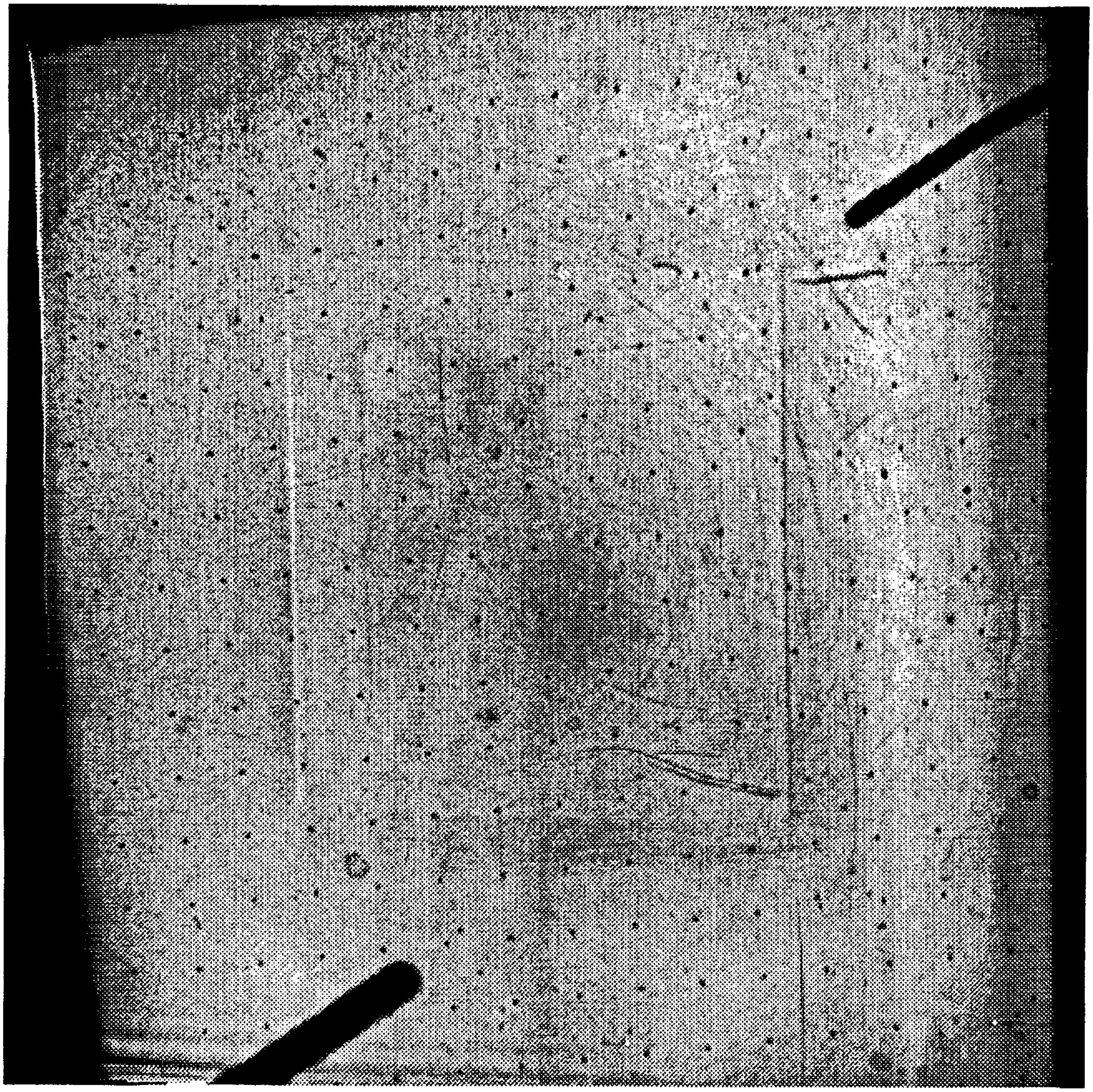

Figure A2. Extended format (512$z\times$ 1024) de-zoomed image taken with the pre-COSTAR F/96 relay under uniform external illumination. The occulting fingers and clipping of the frame due to the baffle are clearly visible.

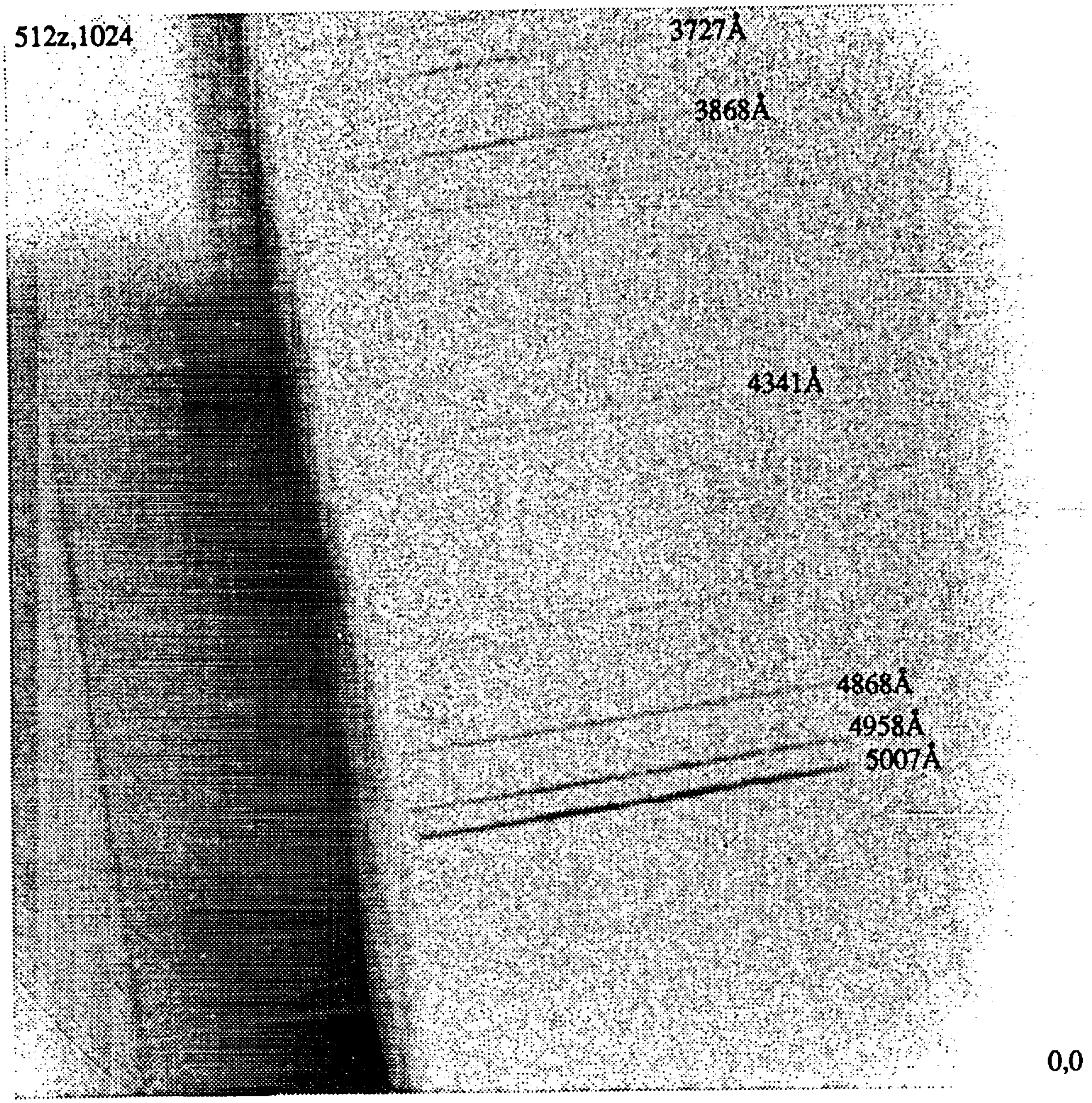

Figure A3. Extended format (512z× 1024) de-zoomed negative image taken with the pre-COSTAR F/48 relay in spectrograph mode of an extended external object. The area in the upper left corner suffers serious vignetting, limiting the wavelength coverage for slitless spectroscopy.

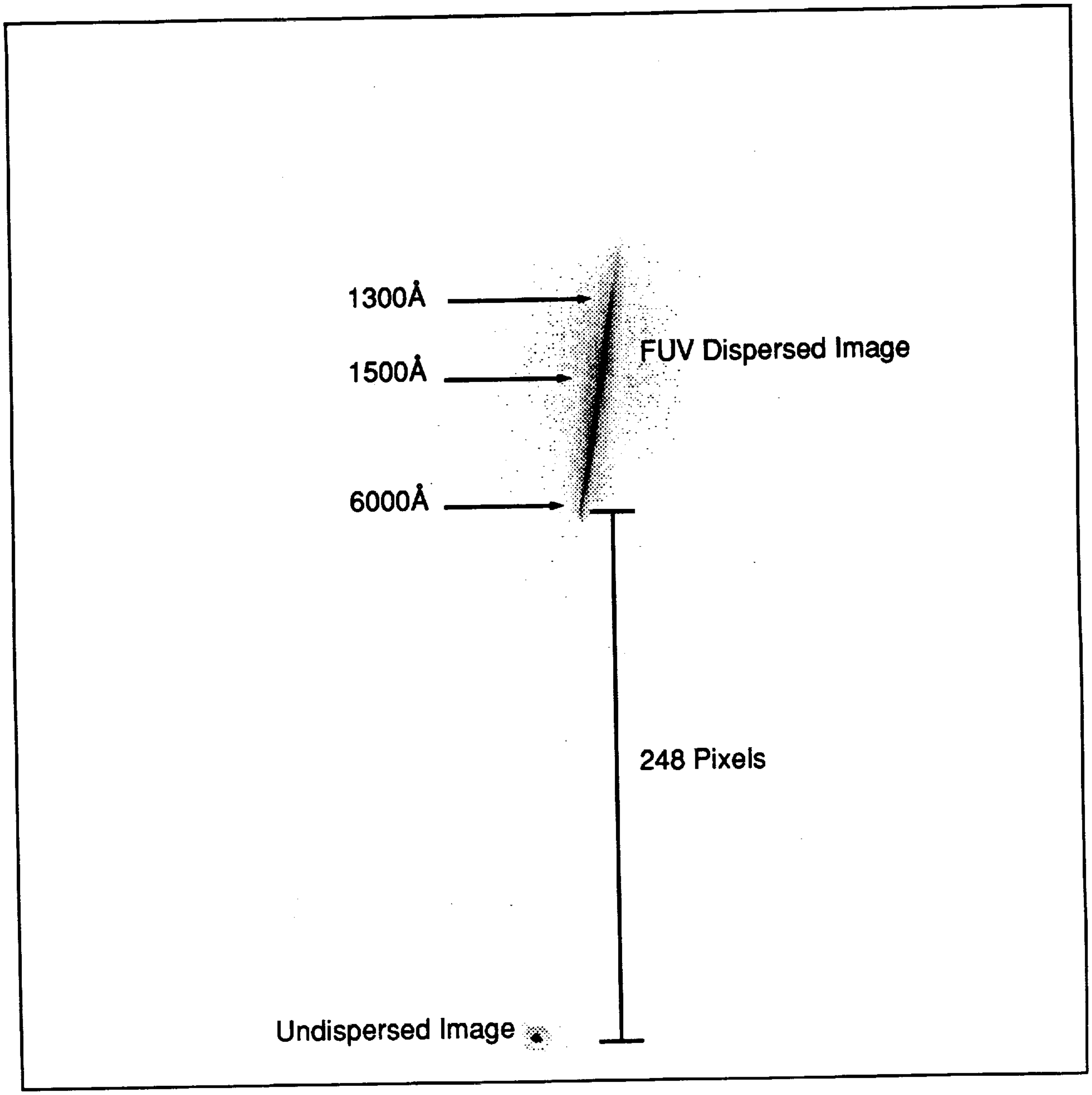

Figure A4. Central 256 × 512 pixels of the full 256 × 1024 pixel negative image taken with the COSTAR-corrected F/96 relay showing a star at the undispersed position overlayed with the image showing its Far-UV prism spectrum.

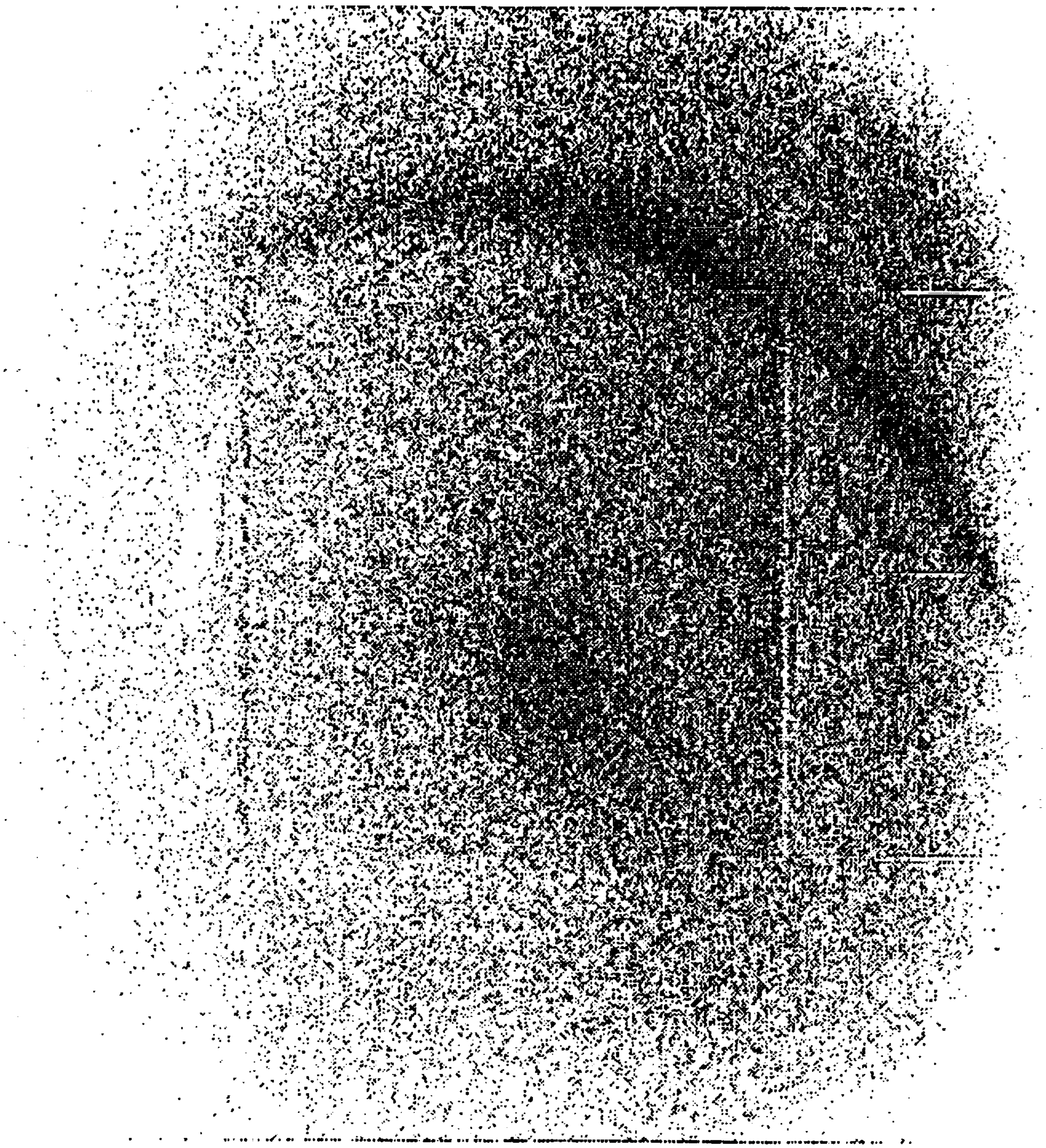

Figure A5. Dezoomed extended (512$z\times$ 1024) negative reproduction of an pre-COSTAR F/48 image showing the high background features. This image is displayed with a very high contrast grayscale to accentuate the shapes of the localized features.